Testing the electroweak sector and determining the absolute luminosity at LHCb using dimuon final states

Jonathan Steven Anderson

UCD School of Physics

A thesis submitted to University College Dublin
for the degree of Doctor of Philosophy

Head of School: Prof. L. Hanlon

Supervisor: Dr. R. McNulty

October 2008

Abstract

The LHCb [1] detector, which commenced data-taking at the Large Hadron Collider [2] in September 2008, is a foward single arm spectrometer optimised for measurements of $\mathcal{CP}$-violating and rare decays in the b quark sector. This thesis describes preparatory Monte-Carlo based studies of two proposed physics measurements that will be made at LHCb.

Firstly, the trigger, reconstruction and selection efficiencies for recording $Z \rightarrow \mu^+\mu^-$ events at the LHCb experiment are presented. From simulation we conclude that LHCb will be capable of reconstructing Z bosons via this channel with rapidities in the range 1.7<y<4.9 with an overall efficiency of 0.358 ± 0.002(stat.), yielding $\sim$172,500 events for an integrated luminosity of $1 fb^{-1}$. The background has been studied at the four-vector level and is estimated to be (3.0 ± 2.9)% of the signal level with the dominant contribution coming from events where two hadrons are misidentified as muons, a background source that can best be estimated from the data themselves. Systematic uncertainties in the efficiency and purity are discussed and expected to be <0.5% for a cross-section measurement in the forward region (1.7<y<4.9). Assuming the luminosity can be determined at a similar level, LHCb will rapidly be able to make a unique measurement of $\sigma_Z \cdot Br(Z \rightarrow \mu^+\mu^-)$ at high rapidities with a precision of about 1%. This measurement will provide an important cross-check for the corresponding measurements at CMS and ATLAS, and, in conjunction with a measurement of the W cross section, precisely test the electroweak sector at LHC energies. In addition measurements of the differential distributions, dσ/dy and dσ/dP_T, will constrain the proton parton distribution functions and provide a stringent test of QCD at high-Q^2.

Secondly, the feasibility of using the elastic two photon process $pp \rightarrow p + \mu^+\mu^- + p$ to make luminosity measurements at LHCb is investigated. The overall efficiency at LHCb for recording and selecting $pp \rightarrow p + \mu^+\mu^- + p$ events produced within the pseudorapidity range $1.6 < \eta < 5$ has been determined using Monte-Carlo to be 0.059 ± 0.001(stat.), yielding $\sim$5200 events for an integrated luminosity of $1 fb^{-1}$. The main background processes where dimuons are produced via inelastic two-photon fusion and double pomeron exchange have been studied using the full LHCb detector simulation while the other background sources, including backgrounds caused by K/π mis-identification, have been studied at the four-vector level. The background is estimated to be $(4.1 \pm 0.5(\text{stat.}) \pm 1.0(\text{syst.}))$% of the signal level with the dominant contribution due to K/π mis-identification. Systematic uncertainties on a luminosity measurement at LHCb using this channel are estimated to be $\sim$1.3% and are dominated by the uncertainty on the predicted cross-section for events containing dimuons produced via double pomeron exchange, an uncertainty that is expected to be reduced in the near future.

Declaration

This thesis is the result of my own work, except where explicit reference is made to the work of others, and has not been submitted for another qualification to this or any other university.

Jonathan Anderson

Acknowledgements

I am immensely grateful to Ronan McNulty for his excellent supervision during the last five years. Almost every aspect of the work outlined in this thesis has benefited from his wisdom and experience. I thank him for having faith in my abilities, dedicating so much of his time to me, teaching me a great deal and for dissuading me from quitting when my enthusiam for physics was at its lowest. Thanks Ronan!

My thanks go to the Head of the UCD School of Physics, Gerry O'Sullivan, for giving me the opportunity to undertake this research, and to University College Dublin for providing financial assistance in the form of a Research demonstratorship and a UCD presidents research award. I also acknowledge the funding provided by the European Union via the Marie-Curie grant MTKD-CT-2004-003134.

I would like to express my gratitude to the other members of the LHCb group at UCD, especially Aidan Smoker, Karol Hennessy, Tahar Kechadi and Zoltan Mathe, for their friendship and for making the last five years so enjoyable. In particular I would like to thank Karol for being such a great flat mate during our stay at CERN and for his patience when answering all of my computing related questions.

I thank the members of the LHCb group at the University of Liverpool, in particular Tara Shears and Themis Bowcock, for their friendship and advice, especially during the last months of my PhD when I was based at CERN.

I thank Alan Martin, James Stirling, Robert Thorne and Greame Watt for invaluable discussions and suggestions regarding the Z cross-section measurement work outlined in chapter 4. I also thank Tara Shears for initially bringing the $Z \rightarrow \mu^+\mu^-$ channel to my attention and subsequently for her many useful suggestions and comments.

I thank Mike Albrow, Valery Khoze, Alan Martin and Andrey Shamov for many useful comments and suggestions regarding the work outlined in chapter 5. I am particularly grateful to Andrey Shamov for providing me with a copy of his modified version of the LPAIR Monte-Carlo generator.

Above all, I would like to thank my parents Susan and Steven. Without their love and support I would never have made it this far. Mum, Dad: I love you both very much, thank you for everything! I would also like to express by love and gratitude to my sisters, Heidi and Lynn, and to my Grandmother Ella.

Finally, I would like to dedicate this work to the memory of my Grandfather Bob who passed away as this thesis was nearing completion. It was his influence more than anything else that has lead me towards a life in science. His friendship, wisdom, intelligence and advice are sorely missed.

Contents

In loving memory of my Grandfather.

1 Introduction

The goal of particle physics is to describe the elementary constituents of matter and the interactions that can occur between them. Since these fundamental elements are point-like and often don't occur under normal circumstances in nature, particle physics experiments must probe nature at very small length scales while at the same time providing sufficient energy for new particles to be created. This is achieved by colliding highly energetic particles together using a particle accelerator: since the length scale probed by a particle is inversely proportional to its energy, particles with higher energies probe smaller length scales; furthermore due to the equivalence of mass and energy, the energy involved in the collision can be used to create other, possibly more massive, particles. In the past this technique has proven to be very successful in improving our understanding of the Universe and, generally speaking, with each increase in accelerator energy new elements of nature have been revealed.

Currently all of the experimentally observed matter particles and three of the four fundamental interactions - the Electromagnetic, Weak and Strong forces - can be described by a set of gauge quantum field theories that are collectively known as the Standard Model (SM)[3, 4, 5]. Although the SM, which was developed in the 1960s and 1970s, has withstood rigorous experimental tests over the last thirty years it has several deficiencies, primarily:

1. Within the SM the matter particles and the Weak vector bosons gain inertia via their interaction with a complex scalar field known as the Higgs field. Although the existence of this field can be confirmed experimentally by observing the quanta of one of the components of the Higgs field, known as the Higgs boson, such an observation has yet to be made.
2. The fourth fundamental force, Gravitation, is not accounted for within the SM framework - the SM is therefore incomplete.
3. Although the SM can partially account for the observed matter-antimatter asymmetry in the Universe via the phenomenon of $\mathcal{CP}$ violation, which arises via the inclusion of a complex phase in the quark mixing matrix, the predicted level of $\mathcal{CP}$ violation in the SM is insufficient to fully account for this asymmetry.

In an attempt to shed new light on these problems a new proton-proton collider, known as the Large Hadron Collider (LHC)[2], is being commissioned at CERN, the European centre for nuclear research, near Geneva, Switzerland. At four locations on the LHC ring, high energy protons will be brought into collision with each other with, by far, the highest accelerator energies ever recorded ($\sqrt{s}$ =14TeV) and replicate the conditions present in the early Universe fractions of a second after the Big Bang. Each of these interaction points will be surrounded by one of four giant particle detectors, named ATLAS[6], CMS[7], Alice[8] and LHCb[1].

This thesis presents the results of preparatory Monte-Carlo based studies of two proposed physics measurements at the LHCb experiment. The first measurement, a determination of the total and differential Z cross-section times leptonic branching fraction, will improve our understanding of the internal structure of the proton, test the theoretical structure describing the Strong force in a new energy regime and, in conjunction with a measurement of the W cross-section, precisely test the theory that describes Electroweak interactions. The preparations for this measurement are outlined in Chapter 4. The second measurement, a determination of the event rate of the rare QED process $pp \rightarrow p + \mu^+\mu^- + p$, is described in Chapter 5 and can be used to make a precise evaluation of the absolute luminosity at LHCb - a quantity that is needed for all absolute cross-section measurements. To place this work in context we begin, in Chapter 2, by summarising the Standard Model and physics at hadron colliders before giving a brief overview of the LHC and the LHCb detector in Chapter 3.

2 Theoretical context

This chapter introduces some of the theoretical concepts that will be required to understand the subsequent parts of this thesis. We begin by briefly summarising the current theory, known as the Standard Model, that describes the elementary building blocks of the Universe. This is followed by an overview of how the properties of physics processes at the LHC can be calculated.

2.1 The Standard Model

Our current understanding of the fundamental constituents of matter and the interactions between them is encapsulated by a set of gauge quantum field theories that are collectively known as the Standard Model (SM). This section gives a brief overview of the SM. For a more complete description see, for example, references[9],[10] or[11].

2.1.1 The Fundamental Particles

Within the SM all matter and three of the four fundamental forces of nature - the Electromagnetic, Weak and Strong interactions - are described in terms of three types of fundamental particles: leptons, quarks and mediators. The leptons and quarks are fermions[1] and form all the matter in the universe while the mediators are bosons and act as messenger particles that communicate the forces between the fermions. Every particle has an anti-particle partner possessing the same mass and spin, but opposite charge and internal quantum numbers. A given force can be communicated between two matter particles if both particles carry a non-zero charge for that force, e.g. if two particles are electrically charged they can interact via the electromagnetic interaction. The properties of the leptons, quarks and mediators are:

Leptons: There are six leptons and their corresponding six anti-particles. They are naturally divided into three generations with the members of higher generations having larger masses than those in lower generations. Beginning with the first generation the members of the lepton generations are: the electron (e) and the electron neutrino (ν_e), the muon (μ) and the muon neutrino (ν_μ), and the tau (τ) and the tau neutrino (ν_τ). In units of e, the charge on the electron, the leptons have an electromagnetic charge of +1 or -1 except for the neutrinos that have a charge of 0. Their properties are summarised in table 2.1.

[1] A particle that possesses half-integer spin is referred to as a fermion while particles with integer spin are known as bosons.

Generation	Lepton	Mass (MeV/c^2)	Spin	Q/e
1	e^-	0.510998910(13)	1/2	-1
	ν_e	< 0.002 (CL=95%)	1/2	0
2	μ^-	105.6583668(38)	1/2	-1
	ν_μ	< 0.19 (CL=90%)	1/2	0
3	τ^-	1776.84(17)	1/2	-1
	ν_τ	< 18.2 (CL=95%)	1/2	0

Table 2.1: Summary of the lepton properties, including electromagnetic charge Q, mass and spin [12]. For the quoted electron, muon and tauon masses, the uncertainties on the last digits are given in parentheses.

Generation	Quark	Mass (MeV/c^2)	Spin	Q/e
1	u	$2.55^{+0.75}_{-1.05}$	1/2	+2/3
	d	$5.04^{+0.94}_{-1.54}$	1/2	-1/3
2	c	1270^{+70}_{-110}	1/2	+2/3
	s	104^{+26}_{-34}	1/2	-1/3
3	t	171200 ± 2100	1/2	+2/3
	b	4200^{+170}_{-70}	1/2	-1/3

Table 2.2: Summary of the quark properties, including electromagnetic charge Q, mass and spin[12].

Quarks: There are six quark types that come in three varieties that are distinguished by a colour quantum number (that can have the value of blue, red or green) and their corresponding anti-particles. This makes for a total of eighteen quarks and eighteen anti-quarks. Again the quarks are divided into generations as shown in table 2.2. The members of the quark generations are: up (u) and down (d), charm (c) and strange (s), and top (t) and bottom (b). The quarks have an electromagnetic charge of $+\frac{2}{3}$ or $-\frac{1}{3}$ in units of e. As we shall see in section 2.1.4, quarks never appear in nature as free particles, they are always confined in colourless combinations as mesons (the quark anti-quark bound state) or as baryons (consisting of three quarks or three anti-quarks).

Mediators: Within the SM the Electromagnetic, Weak and Strong forces are mediated by spin-1 gauge bosons. The leptons only participate in the Electromagnetic and Weak interactions which are mediated by the photon (γ) and the massive gauge bosons $W^\pm$ and Z. The quarks in addition to participating in Electromagnetic and Weak processes also interact via the Strong force that is mediated by the gluons (g). There are 8 different gluons each one having a

Force	Particle	Mass (GeV/c^2)	Spin	Q/e
Electromagnetism	γ	$< 6 \times 10^{-16}$ (CL=99.7%)	1	0
Weak nuclear	$W^{\pm}$	80.398 ± 0.025	1	± 1
	Z	91.1876 ± 0.0021	1	0
Strong nuclear	g	0	1	0
Mass	H^0	> 114.4 (CL=95%)[13]	0	0

Table 2.3: Gauge boson properties including spin, charge and mass [12]. It should be noted that the gluon mass quoted is the theoretical value. A gluon mass as large as a few MeV/c^2 may not be precluded[14].

different colour configuration - see section 2.1.4 for more details on this. The SM also predicts the existence of a massive scalar (i.e. spin 0) mediator called the Higgs boson (H^0). Its role within the theory is to enable the particles to acquire mass and, in particular, to explain why the photon is massless while the $W^{\pm}$ and Z are massive. Without the Higgs boson the SM would predict that all of the particles are massless. The Higgs boson is the only element of the SM currently lacking experimental confirmation. The gauge boson properties are summarised in table 2.3.

In total then there are sixty one elementary particles within the SM framework. Twelve leptons, thirty six quarks and thirteen mediators. As already mentioned, the SM only describes three of the four known fundamental interactions - Gravitation is not included at all. In spite of this fact the SM still constitutes an effective theoretical structure for describing interactions between the fundamental bosons and fermions since the gravitational force is roughly 40 orders of magnitude weaker than the other fundamental interactions.

2.1.2 Mathematical Framework

Mathematically the SM treats particles as excitations of relativistic quantum fields. The interactions between these particle fields are described by quantum field theories that obey local gauge invariance, i.e. their associated Lagrangians are invariant under specific local transformations. This gauge invariance leads to the conservation of one or more charges carried by the particle fields. If the field has only one associated charge the gauge invariance of the field is based on the unitary transformation group $U(1)$ while if the field has $n > 1$ associated charges the invariance is based on the group $SU(n)$. The structure of the SM is given by the symmetry group $SU(3)_C \otimes SU(2)_I \otimes U(1)_Y$. The non-Abelian[2] groups $SU(3)_C$ and $SU(2)_I \otimes U(1)_Y$ represent respectively: Quantum Chromodynamics (QCD), the theory that

[2] A non-Abelian group is one where the group operation * is non-commutative. In other words, for two elements of the group, x and y, the operation $x * y$ is not necessarily equal to $y * x$.

describes the Strong force, and Electroweak theory, which unifies the Electromagnetic and Weak forces. Here the subscripts C, I and Y refer to the conserved charges of each group: the colour charge, weak isospin and weak hypercharge [3].

Since the SM is a quantum field theory it utilises a Lagrangian operator to completely describe the particles and the interactions between them. In the following sections the gauge field theories describing the Elecromagnetic, Strong and Weak forces and the resulting Lagrangians will be described in more detail. For a more complete discussion see, for example, reference [11].

2.1.3 Quantum Electrodynamics

Quantum Electrodynamics (QED), the quantum field theory that describes electromagnetic interactions, is based on the requirement that the Lagrangian for an electromagnetically charged particle should be left unchanged under the application of a local phase transformation.

The Lagrangian corresponding to the Dirac equation for a free fermion field ψ having spin $s = \frac{1}{2}$ and mass m is

$$L_{free} = \bar{\psi}(x)(i\gamma^{\mu}\partial_{\mu} - m)\psi(x) \tag{2.1}$$

. Although this Lagrangian is invariant under *global* phase transformations of the fermion field, i.e. $\psi \rightarrow e^{i\theta}\psi$, it is not invariant under *local* phase transformations, where θ depends on the space-time coordinate, since the partial derivative in equation 2.1 will transform as

$$\partial_{\mu}\psi(x) \rightarrow \partial_{\mu}[e^{i\theta(x)}\psi(x)] = e^{i\theta}(\partial_{\mu} + i\partial_{\mu}\theta(x))\psi(x) \tag{2.2}$$

. In order for the Lagrangian to be *locally* invariant under all such phase transformations - which are collectively described by the mathematical group $U(1)$ - an additional piece must be added to the Lagrangian that transforms in such a way as to cancel the $\partial_{\mu}\theta(x)$ term in 2.2. This can be achieved if a vector field $A_{\mu}(x)$ is introduced that transforms under the local gauge transformation as

$$A_{\mu}(x) \rightarrow A_{\mu}(x) - \frac{1}{e}\partial_{\mu}\theta(x) \tag{2.3}$$

and which defines the covariant derivative

$$D_{\mu}\psi(x) = [\partial_{\mu} - ieA_{\mu}(x)]\psi(x) \tag{2.4}$$

. This covariant derivative then replaces the partial derivative ∂_{μ} in 2.1 and transforms locally under $U(1)$ as

$$D_{\mu}\psi(x) \rightarrow (D_{\mu}\psi)'(x) = e^{i\theta}D_{\mu}\psi(x) \tag{2.5}$$

[3] The weak hypercharge of a particle is defined as $Y = 2(Q - I_3)$ where Q is the particle's electromagnetic charge and I_3 the third component of its isospin.

If A_μ is to be a true propagating field then a gauge invariant kinetic term must also be included in the Lagrangian. The QED Lagrangian therefore has the form

$$L_{QED} = \bar{\psi}(x)(i\gamma^\mu D_\mu - m)\psi(x) - \frac{1}{4}F_{\mu\nu}(x)F^{\mu\nu}(x) \tag{2.6}$$

where $F_{\mu\nu} = \partial_\mu A_\nu - \partial_\nu A_\mu$ is the field strength tensor and the indices μ and ν run over the four space-time coordinates.

This vector field A_μ can be identified as the propagator for the electromagnetic force and is usually called the photon. The strength of the coupling between charged fermions and the photon is given by e and is usually expressed as $\alpha_{em} = e^2/4\pi$. This propagator must be massless since the addition of a mass term, $\frac{1}{2}m^2 A_\mu A^\mu$, to L_{QED} would violate local gauge invariance. This prediction of a massless electromagnetic propagator is in agreement with experimental observation of the massless photon.

2.1.4 Quantum Chromodynamics

The gauge theory that describes the field associated with the Strong force is called Quantum Chromodynamics (QCD). The theory is based on the application of the gauge invariance associated with the $SU(3)_c$ symmetry group and results in eight massless vector fields which are identified as the propagators of the Strong interaction and are known as gluons. Unlike the $U(1)$ group, the $SU(3)_c$ group is non-Abelian which means that the gluons carry colour charge and can couple to one another. Requiring local gauge invariance the QCD Lagrangian can be written as

$$L_{QCD} = \sum_f \bar{q_f}(x)(i\gamma_\mu D^\mu - m_f)q_f(x) - \frac{1}{4}F^a_{\mu\nu}(x)F^{\mu\nu}_a(x) \tag{2.7}$$

where we have summed over all of the quark flavours f and

$$F^a_{\mu\nu} = \partial_\mu A^a_\nu - \partial_\nu A^a_\mu - \sqrt{4\pi\alpha_s} f^{abc} A^b_\mu A^c_\nu \tag{2.8}$$

is the field strength tensor of the gluon field, A^a, with the indices a,b,c running from 1 to 8. f^{abc} are known as structure functions and define the Lie algebra of the group[15] while m_f is the mass of the quark of flavour f and α_s is the strong gauge coupling constant.

Asymptotic freedom and quark confinement

The non-Abelian nature of QCD causes it to differ from QED in one important way: the gauge coupling constant α_s varies more considerably than α_{em} as a function of four-momentum scale Q. The variation in α_s is caused by the vacuum polarisation due to the production and annihilation of virtual quarks and gluons. In an effort to illuminate its effects within QCD we first consider how the corresponding effect arises in QED. Within QED so called charge screening can

occur whereby virtual charged pair production occurring near a charged particle will cause the vacuum to become polarised in the region surrounding the particle. This polarisation causes the effective charge of the particle to vary with distance and results in an electromagnetic coupling constant, α_{em} , that increases with increasing momentum transfer, Q^2. In a similar way virtual quark-antiquark pairs also cause a screening of the colour charges of QCD. However, here the effect is more complicated since the gluons also carry colour charge and can alter the strong coupling constant in the same way. The net effect of the polarization caused by virtual gluons in the vacuum is not to screen the field, but to increase it. Since the virtual quarks and the virtual gluons have opposite contributions to this QCD charge screening, determining which effect wins out depends on the number of quark flavours. To highest order in α_s the dependence of α_s on the four-momentum scale Q is given by

$$\frac{\partial \alpha_s(Q^2)}{\partial \ln(Q^2)} = \beta(\alpha_s(Q^2)) \simeq -\frac{11N_c - 2n_f}{12\pi}\alpha_s^2 \tag{2.9}$$

where N_c and n_f are the number of colour charges and number of quark flavours respectively. Since there are 6 quark flavours and 3 colour charges within QCD it can be seen that α_s will decrease with increasing Q^2, an effect known as *asymptotic freedom*. This so called charge anti-screening in QCD has two important consequences. Firstly, although the strong coupling constant is large at low energies, asymptotic freedom allows cross-sections for processes involving the strong interaction to be calculated using perturbation theory so long as those processes occur at high energies. Secondly, since the effective strength of the strong force increases with distance, if two quarks are separated, α_s will continue increasing until the field gains a sufficient amount of energy to create a new $q\bar{q}$ pair. This effect whereby no finite amount of energy can liberate a quark is called *quark confinement* and explains why no free quarks are seen in nature.

2.1.5 Electroweak Theory

It has been observed that charged weak interactions are only possible between fermions with left-handed helicity[4] and that the mediator of the neutral weak interaction couples to left and right-handed particles with different strengths. Electroweak theory [16], the quantum field theory that describes the electromagnetic and weak forces, therefore deals with the right and left hand parts of Dirac fields separately by grouping each generation of quarks and leptons into left-handed doublets and right-handed singlets of the form:

$$\begin{pmatrix} l^- \\ \nu_l \end{pmatrix}_L, \begin{pmatrix} u \\ d' \end{pmatrix}_L, l_R^-, u_R, d'_R \tag{2.10}$$

where d' represents the down type quark weak eigenstates.

Within Electroweak theory the electromagnetic and weak nuclear interactions are unified and their combined Lagrangian obeys the local gauge invariance given by the $SU(2)_I \otimes U(1)_Y$

[4] helicity being the component of a particles spin in the direction of its motion

symmetry group. The local phase transformation given by this group, under which the Electroweak Lagrangian is invariant, is of the form:

$$T = exp(-i(\frac{g_1}{2}Y\theta'(x) + \frac{g_2}{2}\sigma_i\theta_i(x))) \qquad i = 1,2,3 \tag{2.11}$$

Where Y is the diagonal matrix of the weak hypercharges of the particles, σ_i are the Pauli matrices, and g_1 and g_2 are the gauge couplings for the $U(1)_Y$ and $SU(2)_I$ groups respectively. Requiring this local gauge invariance of the Electroweak Lagrangian results in three massless spin-1 fields (W^1, W^2, W^3) associated with $SU(2)_I$, and a massless spin-1 field B associated with $U(1)_Y$. In a similar way to QED and QCD, if the addition of these fields is to satisfy the requirement of local gauge invariance, the fields must be massless. This is a situation that is at odds with experimental data[17, 18] since three of the electroweak mediators, $W^{\pm}$ and Z, are massive while only one, the photon, is massless. As we shall see in the following section this dilemma can be resolved by the inclusion of an additional scalar field which breaks the electroweak symmetry and allows the weak vector bosons to become massive.

The Higgs Mechanism

The physical mass of the Weak vector bosons, $W^{\pm}$ and Z, is explained by the existence of a scalar field ϕ, called the Higgs field[19], that breaks the electroweak symmetry and in the process of doing this causes the fermions and Weak vector bosons to acquire mass. This mechanism, often referred to as *Spontaneous Symmetry Breaking* (SSB), is based on the *Goldstone Theorem*[20] which states that if a Lagrangian has a continuous global symmetry other than the trivial symmetry associated with the vacuum then there must exist one massless boson, called a Goldstone Boson, associated with each generator. The Higgs mechanism exploits this fact by introducing a doublet of complex scalar fields $\phi^0(x)$ and $\phi^+(x)$ with hypercharge $Y = +1$ in $SU(2)_L \otimes U(1)_Y$ space:

$$\phi(x) \equiv \begin{pmatrix} \phi^{(0)}(x) \\ \phi^{(+)}(x) \end{pmatrix} = \frac{1}{\sqrt{2}} \begin{pmatrix} \phi_1(x) + i\phi_2(x) \\ \phi_3(x) + i\phi_4(x) \end{pmatrix} \tag{2.12}$$

These fields have an associated scalar potential $V(\phi)$ of the form:

$$V(\phi) = \mu^2\phi^\dagger\phi + \lambda(\phi^\dagger\phi)^2, \qquad \lambda > 0. \tag{2.13}$$

If $\mu^2 > 0$ this potential has a trivial minimum at $\phi = 0$ corresponding to the ground state of the system (vacuum) while if $\mu^2 < 0$ the potential has a non-trivial ground state given by:

$$| < 0|\phi^{(0)}|0 > | = \sqrt{\frac{-\mu^2}{2\lambda}} = \frac{v}{\sqrt{2}} \tag{2.14}$$

Here v is the vacuum expectation value. This ground state is degenerate having an infinite number of solutions corresponding to any point on the circle given by

$$|\phi_0|^2 = \frac{(\phi_1+\phi_2+\phi_3+\phi_4)}{2} = \frac{v^2}{2} \tag{2.15}$$

and according to Goldstone's Theorem will result in four Goldstone Bosons. Three of these bosons will be massless while one of them, called the Higgs Boson, will have a mass $M_H = \sqrt{2\lambda v^2}$. By performing a unitary gauge transformation on the field $\phi(x)$, the three massless bosons can be removed and their degrees of freedom used to give the weak vector bosons mass and a third, longitudinal, polarisation state.

This results in the physically observed states (the weak vector bosons $W_\mu^\pm$, Z_μ and the photon A_μ) being related to the massless fields in the following manner

$$W_\mu^\pm = \frac{1}{\sqrt{2}}(W_\mu^1 \mp W_\mu^2) \tag{2.16}$$

$$\begin{pmatrix} Z_\mu \\ A_\mu \end{pmatrix} = \begin{pmatrix} \cos\theta_W & -\sin\theta_W \\ \sin\theta_W & \cos\theta_W \end{pmatrix} \begin{pmatrix} W_\mu^3 \\ B_\mu \end{pmatrix} \tag{2.17}$$

where θ_W is the Weinberg or weak mixing angle. The charged W bosons only couple to left-handed helicity states while Z bosons will couple to the right-handed and left-handed components of a fermion field with the following coupling strengths

$$\begin{aligned} c_L^f &= I_3^f - Q_f \sin^2\theta_W \\ c_R^f &= -Q_f \sin^2\theta_W \end{aligned} \tag{2.18}$$

where Q_f and I_3^f are the fermion's electromagnetic charge and third weak isospin component respectively. Interactions between fermions and Z bosons are commonly described by vector and axial-vector coupling constants, g_V and g_A, that are related to the coupling constants of left and right handed currents through the relations:

$$g_V = c_L^f + c_R^f, \quad g_A = c_L^f - c_R^f \tag{2.19}$$

so that we have:

$$\begin{aligned} g_V &= I_3^f - 2Q_f \sin^2\theta_W \\ g_A &= I_3^f \end{aligned} \tag{2.20}$$

The electromagnetic and weak interaction couplings are related via the Weinberg angle in the following manner,

$$e = g_2 \sin\theta_W = g_1 \cos\theta_W \tag{2.21}$$

and the electroweak bosons $W^{\pm}$, Z and the photon γ will then have the following masses

$$M_W = \frac{g_2 v}{2}; \quad M_Z = \frac{g_2 v}{2\cos\theta_W}; \quad M_\gamma = 0 \tag{2.22}$$

The Higgs field will also couple to the fermion fields and in this way will generate their mass. This coupling of the Higgs field to a fermion pair is given by a Yukawa coupling constant of the form

$$C_f = M_f \frac{\sqrt{2}}{v} \tag{2.23}$$

and will vary for each fermion according to its mass M_f.

The Electroweak Lagrangian

The addition of the field $\phi(x)$ means that the electroweak Lagrangian not only has terms due to the interaction of the mediators and fermions but also terms due to the interaction of these particles and the Higgs field:

$$L_{EW} = L_{Bosons} + L_{Fermions} + L_{Higgs} \tag{2.24}$$

The first term describes the interactions between the massless gauge bosons and has the form:

$$L_{Bosons} = -\frac{1}{4} W^i_{\mu\nu} W^{i\mu\nu} - \frac{1}{4} B_{\mu\nu} B^{\mu\nu} \tag{2.25}$$

where the field strength tensors are given by:

$$\begin{aligned} W^i_{\mu\nu} &= \partial_\upsilon W^i_\mu - \partial_\mu W^i_\upsilon - g_2 \varepsilon^{ijk} W^j_\mu W^k_\upsilon \\ B_{\mu\nu} &= \partial_\upsilon B_\mu - \partial_\mu B_\upsilon \end{aligned}$$

Here g_2 is the weak-isospin coupling constant and the indices i, j, k run from 1 to 3. The second term of 2.24 describes the free fermion propagation and their coupling to the massless gauge boson mediators (W^1, W^2, $W^3$and B). It has the form:

$$L_{Fermions} = \bar{\psi}_L \gamma_\mu D^L_\mu \psi_L + \bar{\psi}_R \gamma_\mu D^R_\mu \psi_R \tag{2.26}$$

where the two covariant derivatives are defined as:

$$D^L_\mu = (\partial_\mu - i g_2 \frac{\sigma^i}{2} W^i_\mu - i g_1 \frac{Y}{2} B_\mu) \tag{2.27}$$

$$D^R_\mu = (\partial_\mu - i g_1 \frac{Y}{2} B_\mu) \tag{2.28}$$

Here g_1 is the weak hypercharge coupling. The field $\phi(x)$ adds an extra term to the Lagrangian of the form:

$$L_{Higgs} = (D_\mu^L \phi)^\dagger (D_\mu^L \phi) - V(\phi) - g_f \bar{\psi}\phi\psi \tag{2.29}$$

where the last term in 2.29 is due to the Yukawa coupling between the couplet and a particular fermion ψ. The first term in 2.29 is the Higgs interaction with the mediators (W^1, W^2, W^3 and B).

2.1.6 Quark mixing and CP violation

The experimentally observed phenomenon of quark mixing - charged weak interactions where a quark from one generation changes into a quark from another generation - is accounted for within the SM by allowing the quark weak and mass eigenstates to be different. The quark weak eigenstates, labeled with primes in equation 2.30, are related to the quark mass eigenstates via a unitary 3×3 matrix known as the Cabibbo-Kobayashi-Maskawa (CKM) matrix:

$$\begin{pmatrix} d' \\ s' \\ b' \end{pmatrix} = \begin{pmatrix} V_{ud} & V_{us} & V_{ub} \\ V_{cd} & V_{cs} & V_{cd} \\ V_{td} & V_{ts} & V_{tb} \end{pmatrix} \begin{pmatrix} d \\ s \\ b \end{pmatrix} \tag{2.30}$$

The coupling strength of the 9 possible quark transitions are given by the elements of this matrix. For example, V_{td} gives the strength of the charged weak coupling between t and d quarks. Experimentally it has been seen that the most common charged weak transitions occur between quarks in the same generation while transitions between different generations are much rarer - in other words the diagonal elements of the CKM matrix have been found empirically to be close to one while the off diagonal elements have been found to be small.

The observed phenomenon of $\mathcal{CP}$ violation - a variance of physics under the interchange of particles and anti-particles and a reversal of spatial coordinates - can be accommodated within the SM if the CKM matrix is complex. In general a complex 3×3 matrix is described by 18 parameters. However, the requirement that the CKM matrix is unitary implies 6 orthogonality and 3 normalisation constraints that reduce the number of parameters to 9. Since it is also possible to remove 5 arbitrary phases associated with the 6 quark fields, the CKM matrix can be fully described by 4 independent parameters: 3 rotation angles and 1 complex phase. This complex phase results in the violation of the $\mathcal{CP}$ symmetry within the SM. To see why, consider the Lagrangian describing charged weak transitions between up-type and down-type quarks:

$$L \propto \bar{u}_i \gamma^\mu V_{ij} d_j W_\mu^- + \bar{d}_i \gamma^\mu V_{ij}^* u_j W_\mu^+ \tag{2.31}$$

Transforming this Lagrangian under the combined transformation $\mathcal{CP}$ yields:

$$L_{\mathcal{CP}} \propto \bar{d}_i \gamma^\mu V_{ij} u_j W_\mu^+ + \bar{u}_i \gamma^\mu V_{ij}^* d_j W_\mu^- \tag{2.32}$$

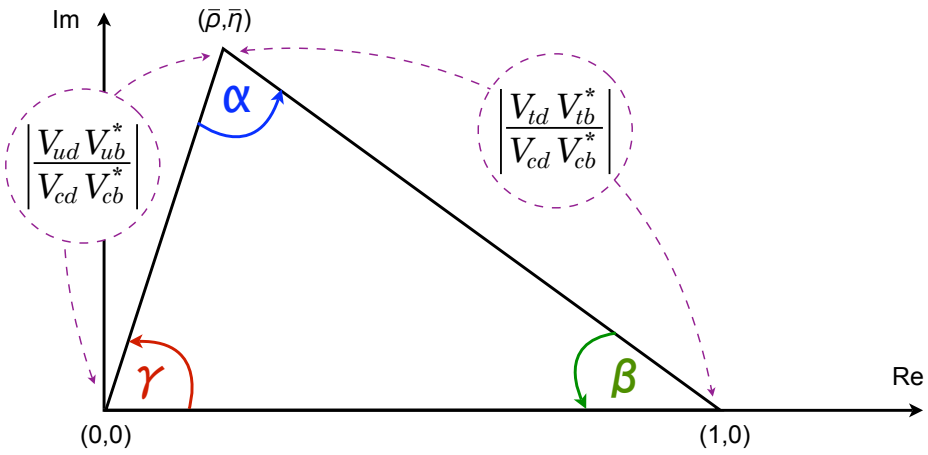

Figure 2.1: The unitarity triangle corresponding to equation 2.33. The base of the triangle has unit length by convention.

Since the CKM matrix contains a complex phase, the matrix elements will not necessarily be equal to their complex conjugates - i.e. $V_{ij} \neq V_{ij}^*$. The Lagrangian may therefore be changed under the $\mathcal{CP}$ transformation resulting in a violation of the $\mathcal{CP}$ symmetry.

The unitarity of the CKM matrix leads to a set of 6 orthogonality relations which can be represented as 6 triangles in the complex plane. However, in only two of them, all three sides are of comparible size, while the remaining triangles all contain one side that is suppressed in length relative to the others. The orthogonality relations describing the two non-squashed triangles are given by:

$$V_{ud}V_{ub}^* + V_{cd}V_{cb}^* + V_{td}V_{tb}^* = 0 \tag{2.33}$$

$$V_{tb}V_{ub}^* + V_{ts}V_{us}^* + V_{td}V_{ud}^* = 0 \tag{2.34}$$

The triangle corresponding to equation 2.33 is shown in figure 2.1 and is defined by three angles: α, β and γ. One of the primary goals of the LHCb experiment is to test the CKM formalism and search for New Physics by measuring the angles of the two non-squashed triangles. Such measurements can provide unambiguous evidence of physics beyond the Standard Model in two different ways. Firstly, if the measured values of α, β and γ do not sum to 180° then the way in which $\mathcal{CP}$ violation is currently incorporated within the Standard Model is wrong. A new mechanism would therefore be needed to explain this phenomenon. Secondly, by measuring the angles given by equations 2.33 and 2.34 via tree-level decay channels, which have little sensitivity to new physics processes, a comparison can be made to the corresponding measurements made using decay channels that are susceptable to perturbative effects caused by loop contributions due to non-SM particles. Any significant discrepancy between these two sets of measurements would therefore be a conclusive sign of New Physics.

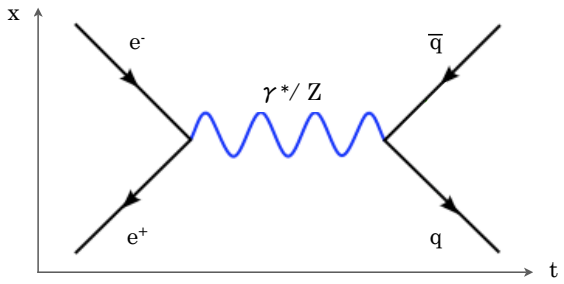

Figure 2.2: The Feynman diagram describing the leading order contribution to the process where an electron annihilates with a positron and a quark anti-quark pair is produced. Here time is represented on the horizontal axis while the vertical axis represents one of the spatial co-ordinates.

2.1.7 Feynman diagrams and perturbative calculations

Within the SM the scattering amplitude for a given process can be written as a perturbation series expansion in powers of the gauge coupling constant - i.e. for QCD interactions the expansion is in powers of α_s. Terms in this perturbative series can be visualised by graphs, known as Feynman diagrams, that have external lines, representing the initial and final states, vertices representing the interactions, and internal lines and loops representing intermediate particles. Figure 2.2 shows an example of a Feynman diagram - here the diagram represents the first term in the perturbative series, known as the leading order contribution, for the process where an electron and a positron annihilate and a quark anti-quark pair is produced. Since each vertex represents an interaction, the probability of a certain process is directly related to the strength of the interaction involved. Higher order calculations are achieved by including diagrams that correspond to higher order terms in the gauge coupling constant - in other words diagrams that contain more vertices. A calculation that includes all terms to order α, compared to the lowest-order diagram, is referred to as next-to-leading order (NLO), while one containing all terms to order α^2 is known as a next-to-next-to leading order (NNLO) calculation. Since the Hamiltonian for a given interaction is expanded in powers of the gauge coupling constant this perturbative prescription for calculating cross-sections only results in convergent solutions if the gauge coupling constant is less than one. The procedure works well for QED interactions where the coupling constant, α_{em}, at low energies is equal to $1/137$ and only increases slowly as a function of Q^2. However, as already alluded to in section 2.1.4, the coupling constant for QCD interactions, α_s, varies as a function of Q^2 and becomes large when $Q^2 < 300 MeV^2/c^4$. In this region the perturbative technique fails and other approximate methods must be used instead.

2.2 Hard scattering processes at the LHC

This section briefly reviews the theoretical techniques that are used to make predictions about the physics processes that will occur in high energy proton-proton collisions at the LHC; further details can be found in reference[21].

The physics processes occurring in high energy proton-proton collisions can be classified as either hard or soft depending on the Q^2 at which the process occurs. The event properties and rates of the primary hard scattering processes (e.g. Z boson production) that occur between the constituent quarks and gluons (known as partons) of the colliding protons can be accurately predicted using perturbative QCD (pQCD). However, since the properties of the partons inside the colliding protons can't be described using perturbation theory, such calculations are performed by employing the *factorisation theorem*[22] and parameterising the internal structure of the proton by so-called parton distribution functions (PDFs). This perturbative technique employing the Factorisation theorem and its application to the Drell-Yan process[24] at the LHC is described in more detail in section 2.2.1.

Calculations of hard scattering processes to all orders in perturbation theory are not possible - indeed, due to their time consuming nature, calculations for many processes have only been performed at leading order. Corrections to perturbative calculations are therefore required and are introduced using *parton showering*[23] techniques. These techniques are outlined in section 2.2.2.

The hard scattering processes that we are primarily interested in at the LHC, do not occur in isolation but are produced in conjunction with other, low Q^2, soft processes. Such soft processes occur most commonly during the process where coloured quarks and gluons, originating both from the hard scatter and the remnants of the dissociated protons, form colourless final state hadrons - a process known as *hadronisation*. As noted in the previous section, perturbative treatments of QCD processes at low Q^2 give unstable solutions - therefore predictions for these soft processes must be obtained using different, less accurate, theoretical methods. The methods most commonly used to describe the process of hadronisation in Monte-Carlo event generators are briefly reviewed in section 2.2.3.

An overview of the various ingredients that must be included to fully describe the physics processes that occur in proton-proton collisions is shown schematically in figure 2.3. Here the areas where soft interactions are dominant, both within the colliding protons and during the hadronisation process, are highlighted in grey.

2.2.1 Hard scattering and the factorisation theorem

Since the proton is a composite particle, theoretical predictions of the physics processes that occur during collisions between high energy protons must take this substructure into account. The factorisation theorem[22], which was first used to describe dilepton production resulting from the annihilation of a quark anti-quark pair (the Drell-Yan process[24]), states that the cross-section for a given physics process resulting from a hadron-hadron interaction can be

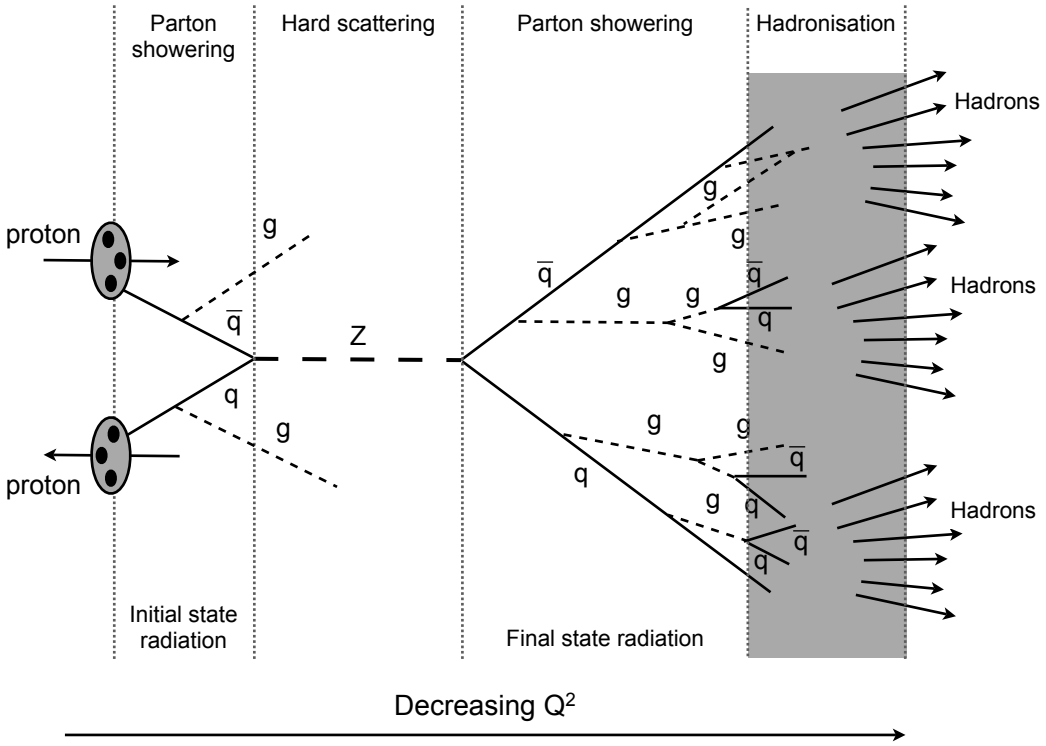

Figure 2.3: Schematic showing an example of a hard scattering process in a proton-proton collision - here the leading order production of a Z boson that subsequently decays to a quark anti-quark pair. All parts, both perturbative and non-perturbative, of the production and decay process are represented including the decay of the resulting quark anti-quark pair into colour neutral final state hadrons (Hadronisation). The areas where soft interactions are dominant, both within the colliding protons and during the hadronisation process, are highlighted in grey.

decomposed as the product of a partonic level cross-section (e.g. $\hat{\sigma}_{q\bar{q}\to l^+l^-}$ for the Drell-Yan process) and a parameterised description of the internal constituents of the colliding hadrons. In other words, the cross-section for the production of a final state X during the collision of two hadrons A and B is given by:

$$\sigma_{AB\to X} = \int dx_a dx_b f_{a/A}(x_a, Q^2) f_{b/B}(x_b, Q^2) \hat{\sigma}_{ab\to X} \tag{2.35}$$

where a and b are the two partons participating in the hard scattering process. Here $f_{a/A}$ and $f_{b/B}$ are the so called parton distribution functions (PDFs) that parameterise the properties of the partons within the colliding hadrons and are functions of x, the fraction of the hadron's longitudinal momentum carried by the various partons, and Q^2 the energy transfered during the hard scatter. The way these PDFs change as a function of Q^2 is described by the DGLAP equations[25]. This fact allows PDFs found at one momentum scale to be evolved to other Q^2 values, a process commonly known as *DGLAP evolution*. Currently PDFs for the proton are produced by a number of different groups, most notably MSTW[26] and CTEQ[27], by

making a global fit to a variety of experimental data that are sensitive to different regions of x and Q^2. The experimental data used in these fits come from a number of different sources: deep inelastic scattering data from HERA, fixed target experiments at Fermilab, CERN and SLAC, and more recently Drell-Yan and jet data from the Tevatron. Multiple data-sets with the same x values but different Q^2 values provide a valuable test of DGLAP evolution.

The Drell-Yan process

The Drell-Yan process[24] is the production of a lepton pair of large invariant mass in hadron-hadron collisions via the mechanism of quark anti-quark annihilation. At the LHC this proceeds predominantly through the production of an intermediate virtual photon but can also, in sufficiently energetic interactions, proceed via an on-shell Z or W.

The leading order parton level cross-section for dilepton production from quark anti-quark annihilation via a massive intermediate photon is a QED process given by

$$\hat{\sigma}_{q\bar{q}\to l^+l^-} = \frac{4\pi\alpha^2}{3\hat{s}}\frac{1}{3}Q_q^2 \tag{2.36}$$

here Q_q^2 is the quark electromagnetic charge and $\hat{s} = x_1x_2s$ where s is the total centre of mass energy squared while $x_1(x_2)$ is the fraction of the first(second) colliding hadron's momentum carried by the quark or anti-quark. The factor of $1/3$ accounts for the fact that only when the colour of the quark matches the colour of the anti-quark can annihilation occur, thus producing a colourless final state (recall there are 3 colour charges in QCD). The parton level differential cross-section as a function of dilepton mass, M, can also be calculated and is given by

$$\frac{d\hat{\sigma}_{q\bar{q}\to l^+l^-}}{dM^2} = \frac{4\pi\alpha^2}{9M^2}Q_q^2\delta(\hat{s}-M^2) \tag{2.37}$$

In an analogous way the leading order parton level cross-section for the production of on-shell Z bosons, an electroweak process, can be calculated:

$$\hat{\sigma}_{q\bar{q}\to Z} = \frac{\pi}{3}\sqrt{2}G_FM_Z^2(g_V^2+g_A^2)\delta(\hat{s}-M_Z^2) \tag{2.38}$$

where $G_F = g_2^2/(4\sqrt{2}M_Z^2cos^2\theta_W)$ is the Fermi constant and M_Z is the mass of the Z boson, while g_V and g_A are the vector and axial couplings respectively.

As outlined in the previous section, the total cross-section can now be determined by convolving these parton level cross-sections with the appropriate hadron PDFs. For example, the cross-section for Z boson production in proton-proton collisions is given by

$$\sigma_{pp\to Z} = \int dx_1dx_2\hat{\sigma}_{q\bar{q}\to Z}\sum_q[f_{q/p_1}(x_1,Q^2)f_{\bar{q}/p_2}(x_2,Q^2)+f_{\bar{q}/p_1}(x_1,Q^2)f_{q/p_2}(x_2,Q^2)] \tag{2.39}$$

From here the cross-section of a particular final state can be obtained by multiplying by the branching fraction for that final state.

2.2.2 Parton showering

The previous section outlined the procedure for calculating the leading order cross-section for the Drell-Yan process at the LHC. This calculation can be extended to include higher order contributions - in fact in recent years exact calculations for this process have been made that include all terms up to next-to-next-to leading order (NNLO)[28]. Unfortunately, even these state of the art calculations are still missing higher order terms that will contribute to the overall cross-section. The standard procedure for dealing with the higher orders that are not included in a given perturbative calculation is to add initial and final state parton showers to the process in question. This works in the following way. Since the partons carry electromagnetic and/or colour charge, the higher order contributions that are missing will take the form of emissions of gluons and photons. These missing terms can be approximated by adding additional radiative processes whereby a parton is allowed to branch into a parton with lower energy plus, for example, an emitted gluon, i.e. $q \rightarrow qg$. This branching is usually modeled using the Altarelli-Parisi splitting function[23]. The showering continues until the branching quarks and gluons reach some predefined energy which is above the confinement regime. The Monte-Carlo generators PYTHIA[29] and Herwig[30] both apply a value of 1GeV.

2.2.3 Hadronisation

At this point we have reached the stage where the hard scattering process can be calculated using a combination of the Factorisation theorem and perturbation theory and the missing higher order terms in the calculation can be approximated using the parton shower method - leaving us with an unphysical state that consists of coloured quarks and gluons. In addition to the quarks and gluons that originate from the hard scatter there will also be a large number of coloured partons that come from the dissociation of the colliding hadrons. The final step, therefore, is to convert all of these coloured objects into a final state of colourless hadrons. This process is called hadronisation and involves soft processes which cannot be described analytically using perturbation theory. Hadronisation is usually modeled using one of the following phenomenological approaches.

String fragmentation model: The String (or Lund) model is based on the starting assumption that the energy stored in the colour dipole field between a charge and an anti-charge, a $q\bar{q}$ pair for example, increases linearly with the separation between the charges. Naively this can be viewed as follows: when the q and $\bar{q}$ are moved apart a coloured flux tube or string, that is uniform along its length, is stretched between them - resulting in a potential that rises linearly. If the energy stored in the string is large enough a second $q'\bar{q}'$ pair or, indeed, two such pairs - i.e. $q'\bar{q}'$ and $q''\bar{q}''$ - can be produced. These new quarks and anti-quarks can then be combined with the original $q\bar{q}$ pair to form two colourless states, either two mesons or two baryons. The splitting of these strings stops whenever there are only on-mass-shell hadrons remaining. The

string fragmentation model is the method that is used to simulate the hadronisation process in the PYTHIA event generator[29].

Cluster model: The cluster model[31] is used to describe the hadronisation process inside the Herwig Monte-Carlo generator[30]. This model begins by splitting all of the coloured gluons resulting from the final state showers into quark anti-quark pairs or diquark anti-diquark pairs. Then all of the resulting quarks are combined with their nearest neighbours to form colourless *clusters*. Finally, the hadrons that these clusters then become are determined by the mass of the cluster.

Since the hadronisation process produces all of the hadrons within the predicted final state - which at the LHC constitutes the vast majority of the final state particles - predictions of the underlying event, i.e. the low transverse momentum (P_T) portion of the event, are highly sensitive to the way hadronisation is treated. The underlying event can have a large influence on the background predictions for some physics measurements. It is therefore desirable to tune the way Monte-Carlo generators deal with the process of hadronisation. Such tuning, which will be done by all of the LHC experiments including LHCb, is usually achieved by adjusting parameters within the hadronisation model until the generator makes predictions about the underlying event that match the experimental data - for example the overall charged track multiplicity as a function of pseudorapidity.

3 Experimental environment

The proposed measurements outlined in this thesis will be made using the Large Hadron Collider Beauty (LHCb) detector. LHCb will utilise the proton-proton collisions generated by the Large Hadron Collider (LHC) to look for signs of New Physics (NP), primarily through measurements of rare and $\mathcal{CP}$ violating decays of B hadrons. This chapter provides an overview of the LHC and the LHCb experiment.

3.1 The Large Hadron Collider

The Large Electron-Positron collider (LEP), the main accelerator facility at the European Centre for Nuclear Research (CERN) near Geneva, was closed in November 2000 to be replaced by a new higher energy accelerator - the Large Hadron Collider (LHC). The LHC, which commenced operation in September 2008, has been built to discover New Physics via direct observations of new particles and through precision tests of SM predictions. This section describes the design, layout and ultimate running performance of the LHC.

3.1.1 Design considerations

Most high energy particle physics experiments use particle colliders to produce the high energy densities required to investigate the fundamental pieces of matter and the interactions between them. These colliders come in two varieties: linear accelerators and circular storage rings. As the name suggests, linear accelerators accelerate particle beams along a straight track. The maximum beam energy attainable with these machines is primarily determined by the length of the accelerator used - a limitation that can be avoided if the particles are instead accelerated along a closed path. At circular storage rings, an accelerator design that was first proposed in the 1950's[32], the particle beams are accelerated, focused and guided using radio-frequency cavities, quadrupole magnets and dipole magnets respectively. The closed particle trajectories at such machines enable the beams to be circulated many times over, gaining energy with each revolution. Since higher beam energies can be attained using circular storage rings, every energy frontier collider for the last 30 years has been of this type. However, there is a draw-back associated with circulating charged particles in a storage ring - they lose energy via synchrotron radiation. The rate that a particle of charge q, mass m and energy E loses energy via synchrotron radiation as it circulates in a storage ring of radius r is given

by

$$\frac{dE}{dt} \propto \frac{E^4 q^2}{m^4 r^2} \tag{3.1}$$

Operating the LEP accelerator at a centre of mass energy of 1TeV, the energy scale at which New Physics is expected to manifest itself, would result in a power loss of 100GW[1]. The only way to avoid this huge power loss is to either increase the size of the ring or accelerate heavier particles.

A parameter of great significance at collider-based particle physics experiments is the total energy available in the centre of mass frame of the two colliding particles. This parameter, commonly referred to as the centre of mass energy ($\sqrt{s}$), is important since it determines the maximum mass of any particles produced in the interactions and consequently it has a large impact on direct searches for New Physics. The centre of mass energy at a colliding beam experiment where two particles of equal energy, E, collide with each other head-on is equal to the sum of their energies - i.e. $\sqrt{s} = 2E$. This contrasts favourably with the situation at fixed target experiments where a beam of high energy particles is incident upon a stationary target. In such collisions the initial momentum in the centre of mass frame of the two particles will be non-zero and therefore, due to the fact that this momentum must be conserved, the particles produced in the interaction will be boosted in the direction of motion of the incoming beam - thus reducing the amount of energy that can be converted into mass. When a particle of energy E collides with a stationary target of rest mass of m, the centre of mass energy is given by $\sqrt{s} \simeq \sqrt{2Em}$. Since $\sqrt{s}$ is directly proportional to the beam energies in symmetric beam-beam collisions while it scales as the square root of the beam energy in beam-target collisions, all energy frontier accelerators are configured to produce head-on collisions between two beams of equal energy.

At hadron colliders the primary hard interactions occur between two partons, one parton from each of the two interacting hadrons. The energy available for the creation of new particles at hadron colliders is therefore not $\sqrt{s}$ but the centre of mass energy of the primary partonic interaction, $\sqrt{\hat{s}} = x_1 x_2 \sqrt{s}$, where x_1 and x_2 are the fractional momenta carried by the two interacting partons. For proton-proton collisons at $\sqrt{s}$ =14TeV, the average values of x_1 and x_2 as a function of the rapidity of the hard interaction sub-system and the resulting probability distribution for $\sqrt{\hat{s}}$ are shown in figures 3.1(a) and 3.1(b) respectively. The most probable value of $\sqrt{\hat{s}}$ occurs for energies just above the confinement regime ($\sim$1GeV) and the distribution falls rapidly for higher $\sqrt{\hat{s}}$ values. Since direct searches for New Physics at particle physics experiments require the production and detection of new particles of unknown mass, the large spread in $\sqrt{\hat{s}}$ at hadron colliders makes them ideal laboratories for discovering New Physics. This contrasts with the situation at electron-positron colliders where very clean events are produced at very well defined centre of mass energies. A systematic search for new heavy particles at an electron-positron collider therefore requires a continuous variation and monitoring of the energy of the two colliding beams[2] - a difficult task that requires more beam time.

[1] When LEP was running at a centre of mass energy of 90GeV the power loss was 10MW.

[2] It should be noted that, due to initial state radiation, resonances with masses lower than the centre of mass energy can be produced at electron-positron colliders.

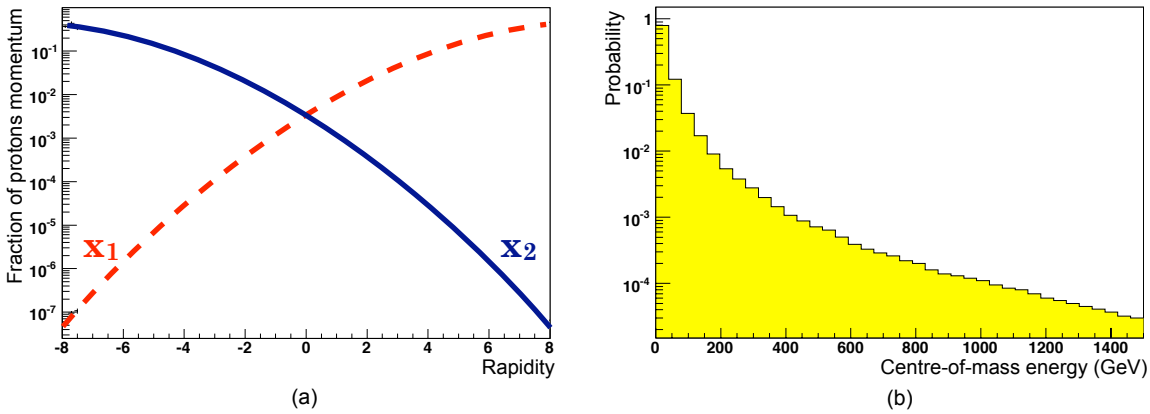

Figure 3.1: (a) Average fractional momenta carried by the two interacting partons, x_1 and x_2, in proton-proton collisions at the LHC as a function of the rapidity of the hard interaction sub-system.(b) Probability distribution for the centre of mass energy of the primary partonic interaction in proton-proton collisions at the LHC.

Electron-positron colliders are therefore more suited for precision measurements of particles that have been previously discovered using a hadron collider. Since the primary task of the next generation of high energy physics experiments will be to discover the Higgs boson and search for physics beyond the Standard Model, such studies will be made at a hadron storage ring collider - the Large Hadron Collider (LHC).

3.1.2 The LHC accelerator system

The LHC[2] consists of a ring of superconducting magnets that will primarily accelerate and store two 7TeV counter-rotating beams of protons[3]. A dipole field of 8.3T is required to constrain a beam containing 7GeV protons inside a 27km circular path of radius 4.3km where 2/3 of the length contains dipole magnets. At the LHC this field is supplied by 1,232 superconducting Niobium-Titanium alloy magnets placed inside a cryostat containing a bath of superfluid helium with a temperature of 1.9K. A cross-section view of one of these dipole magnets is shown in figure 3.2(b). Ultimately it is the bending capability of these magnets which determines the maximum beam energies that will be possible at the LHC. Under design LHC running conditions each of the beams will consist of 3564 "buckets" that will be equally spaced around the ring's circumference, resulting in a bucket frequency of 40MHz and a bucket spacing of 7.5m. However, due to a complicated filling procedure where the beams must be passed from the smaller SPS storage ring into the LHC, only 2808 of the buckets will be filled resulting in an average bunch crossing frequency of 30MHz. Beam lifetimes of $\sim$10 hours will be achieved by maintaining high vacuum conditions of better than 10^{-8}mbar inside the beam pipes. The beams are kept apart except at four locations where the beams cross each other resulting in proton-proton collisions with an ultimate centre-of-mass energy

[3]In order to study heavy ion collisions and search for quark-gluon plasmas, the primary tasks of the Alice collaboration, the LHC will collide heavy nuclei instead of protons for one month every year.

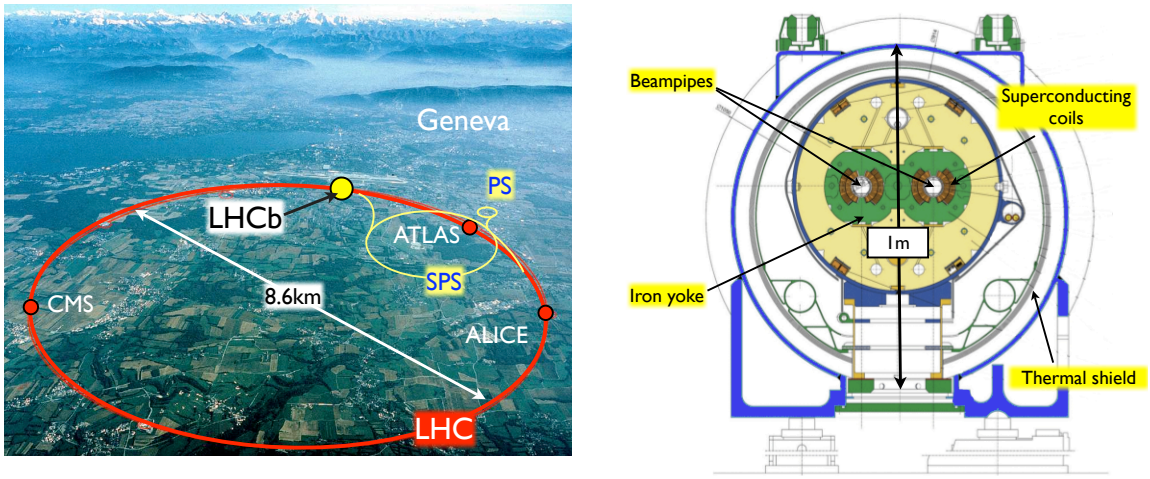

(a) (b)

Figure 3.2: (a) The LHC accelerator system with the location of LHCb shown (from[2]). (b) Cross-section view of one of the LHC dipole magnets (from[2]).

of $\sqrt{s}$ =14TeV. Each interaction point is surrounded by one of four detectors. Two of these detectors are the large multipurpose experiments, ATLAS[6] and CMS[7], while the other two are more specialised: ALICE[8] will study heavy ion collisions and search for quark-gluon plasmas, while LHCb[1] will investigate heavy flavour physics. The primary goal of LHCb is to find indirect evidence of New Physics in $\mathcal{CP}$ violating and rare decays of hadrons that contain b quarks.

The protons in the LHC will be accelerated up to energies of 7TeV in the following way. They are first accelerated along a linear accelerator (LINAC) up to an energy of 50MeV, they are then passed on to the Proton Synchrotron Booster (PBS) rings that will bring them up to 1GeV. From there they are injected into the Proton Synchrotron (PS) that accelerates them up to 26GeV before they are fed into the Super Proton Synchrotron (SPS) where they are accelerated to 450GeV. It is at this point that they are finally passed into the LHC where they are accelerated to their final energy of 7TeV. The layout of the PS, SPS, LHC and the four main experiments, ATLAS, CMS, Alice and LHCb, is shown in figure 3.2(a).

3.1.3 Luminosity at colliding beam experiments

The event rate, $R(t)$, for a given process at a colliding beam experiment like LHCb and the cross-section for that process, σ, are directly proportional to one another. The factor of proportionality that relates these two quantities is known as the *instantaneous luminosity*, $L(t)$, and is a measure of the intensity of the colliding beams.

$$R(t) = L(t) \times \sigma \tag{3.2}$$

For New Physics searches and precision measurements at a collider experiment the quantity of greatest significance is usually the number of events, N, observed during a given running period. Here the proportionality factor is the *time-integrated luminosity* which for a running period of length T is given by

$$L_{int} = \int_0^T L(t)dt \tag{3.3}$$

In terms of the beam parameters the integrated luminosity can be expressed as

$$L = 2cfN_1N_2cos^2(\frac{\phi}{2}) \int \rho_1(\mathbf{x},t)\rho_2(\mathbf{x},t)d^3xdt \tag{3.4}$$

where: c is the speed of light; f is the beam crossing frequency; N_1 and N_2 are the number of particles in the bunches in the two beams; ϕ is the crossing angle of the beams; and ρ_1 and ρ_2 are the bunch densities. The luminosity can therefore be increased by having more particles in the bunches, focusing the beams, increasing the revolution frequency or minimising the crossing angle of the beams.

The measurement of the luminosity at the LHCb experiment is one of the main topics addressed in this thesis. The luminosity must be determined at a colliding beam experiment for two reasons. Firstly, as can be seen from equation 3.2, a measurement of the luminosity is required to make any cross-section measurement. Cross-section measurements are important because they enable comparisons to be made with theoretical predictions. Secondly, it is desirable to be able to optimise the running luminosity of a collider. Generally speaking the goal of such optimisation is to maximise the integrated luminosity so as to record as many events as possible. However, as we shall see, at LHCb the luminosity will be optimised using a different criterion. By investigating the correlation between the luminosity and a variety of beam parameters, these parameters can be tuned to optimise the delivered luminosity.

Luminosity measurements can be made by either directly measuring the beam parameters given in equation 3.4 or, as we shall see in more detail in chapter 5, by measuring the event rate of some accurately predicted physics process. Luminosity measurements can be divided into two classes: high accuracy *absolute luminosity* measurements and less accurate *relative luminosity* measurements that are used to monitor how the beam conditions and luminosity vary during a physics running period. Relative luminosity measurements can be made by relating a stable high rate monitor that is not accurately predicted, J/ψ production for example, to an absolute luminosity measurement that has been made over some extended period or during special beam running conditions.

3.1.4 The design luminosity of the LHC

The luminosity at a storage ring collider like the LHC can be expressed as follows:

$$L = \frac{N_1N_2k_bf\gamma F}{4\pi\beta^\star\varepsilon} \tag{3.5}$$

Parameter	Symbol	LHC design value
Number of protons per bunch	N_i	1.1×10^{11}
Revolution frequency	f	$11.25kHz$
Number of bunches per beam	k_b	2808 (2106 at LHCb)
Emittance	ε	$3.75\mu m$rad
Betatron function	$\beta^\star$	$0.5m$ ($16.7m$ at LHCb)
Crossing angle factor	F	~ 0.9

Table 3.1: The LHC design specifications. The displaced interaction point at LHCb results in one in four bunch crossings being missed - there will only be 2106 bunch crossings per revolution at LHCb compared to 2808 at ATLAS and CMS. Lower running luminosities will be achieved at LHCb by changing the beam optics to defocus the beams. LHCb will nominally operate with a $\beta^\star$ value of 16.7m.

where γ is the relativistic factor for the colliding particles (i.e. E_p/m_p for the colliding protons at the LHC), N_i is the number of protons in each bunch, f is the beam revolution frequency, k_b is the number of bunches in each beam, ε is the emittance - a measure of the compactness of the beam, $\beta^\star$ is a measure of the ability of the magnets to focus the beam at the interaction point and F is a factor that takes into account the angle at which the beams cross each other. The design values of these factors at the LHC are given in table 3.1. Of particular interest is the product $k_b \times f$ that defines the bunch crossing frequency which will have a value of 30MHz at the LHC. This product defines the fundamental time step at all of the LHC experiments and must be taken into account by any trigger strategies that are developed.

The main focus of effort at the LHC's two largest experiments ATLAS and CMS will be the search for the Higgs boson and signs of New Physics. Since many of these New Physics processes are expected to have cross sections of only a few tens of femtobarns at LHC energies, these experiments will require high running luminosities. Accordingly the LHC has a design luminosity of $10^{34}cm^{-2}s^{-1}$, which corresponds to a factor of 100 increase on the luminosity obtained at the previous energy frontier accelerator - the Tevatron at Fermilab. Running at these high luminosities results in an unfortunate side effect - the average number of proton-proton collisions per bunch crossing is much greater than one, making the reconstruction of events much more difficult. The average number of proton-proton collisions per bunch crossing, μ, is related to the luminosity in the following way,

$$\mu = \frac{\sigma_{inelastic} L(t)}{f_{LHC} \varepsilon_{filled}} \tag{3.6}$$

where: $\sigma_{inelastic}$ is the inelastic cross-section at the LHC ($\sim$80mb); $L(t)$ is the instantaneous luminosity; f_{LHC} is the LHC bucket crossing frequency of 40MHz; and ε_{filled} is the fraction of non-empty bucket crossings. As can be seen from equation 3.6, a higher running luminosity will result in a higher average number of proton-proton collisions per bunch crossing. At

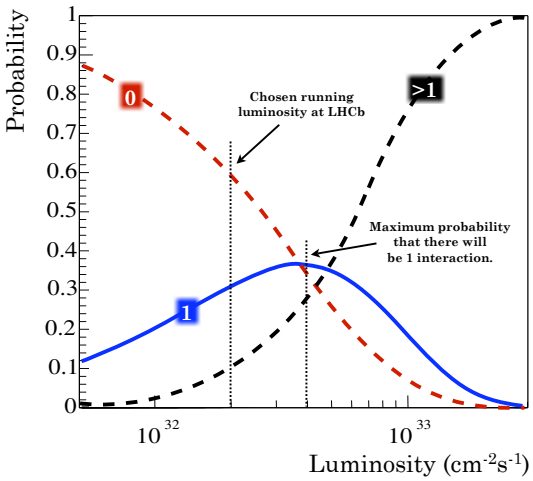

Figure 3.3: Probability distributions for 0, 1 and > 1 proton-proton interaction per bunch crossing as a function of luminosity at LHCb. (Here an inelastic cross-section at the LHC of $80mb$ has been assumed.)

a running luminosity of $10^{34}cm^{-2}s^{-1}$ the average number of proton-proton interactions per bunch crossing is ~ 27.

3.1.5 Optimal running luminosity at LHCb

In contrast to the needs of the LHC's general purpose detectors, the ideal running luminosity at LHCb is substantially lower than $10^{34}cm^{-2}s^{-1}$. Critical to the LHCb physics program is the accurate measurement of the various B hadron lifetimes. This will require a precise determination of the primary and secondary vertex coordinates - a task that is virtually impossible in the pile-up conditions present with a luminosity of $10^{34}cm^{-2}s^{-1}$. The probability that n interactions occur in a given bunch crossing is given by the Poisson distribution

$$P(\mu, n) = \frac{\mu^n}{n} e^{-\mu} \tag{3.7}$$

where μ is the average number of interactions per bunch crossing. Figure 3.3 shows the probability of there being 0, 1 or more than 1 proton-proton interaction in a given bunch crossing at the LHC as a function of instantaneous luminosity. The ideal conditions for reconstructing primary and secondary vertex coordinates are found when there is only one interaction in a given bunch crossing. From figure 3.3 we see that $P(\mu, 1)$ is greatest (~ 0.35) when $L = 4 \cdot 10^{32}cm^{-2}s^{-1}$. However, at this luminosity the probability of having more than one collision in a given bunch crossing is quite high (~ 0.25). Since these multiple interaction bunch crossings can consume bandwidth in the trigger system and will result in increased radiation damage to the detector, the running luminosity at LHCb has been chosen to be $L = 2 \cdot 10^{32}cm^{-2}s^{-1}$. At this luminosity $\sim 30\%$ of bunch crossings at LHCb will result in one and only one proton-proton interaction while $\sim 8\%$ will result in more than one interac-

Process	Expected cross-section (pb)		Uncertainty on
	$\sqrt{s}$ =10TeV	$\sqrt{s}$ =14TeV	cross-section prediction
Total	9.6×10^{10}	10.1×10^{10}	$O(50\%)$
Inelastic	7.4×10^{9}	8×10^{9}	$O(50\%)$
$b\bar{b}$ production	3.3×10^{8}	4.8×10^{8}	$O(50\%)$
$Z \rightarrow \mu^{+}\mu^{-}$	1.28×10^{3}	1.90×10^{3}	$O(5\%)$
$pp \rightarrow p + \mu^{+}\mu - + p$	1.30×10^{5}	1.48×10^{5}	$O(1\%)$

Table 3.2: Expected production cross sections, in units of pico-barns, for various processes at the LHC.

tion giving an average number of interactions per bunch crossing of 0.53. In order for LHCb to operate at a lower luminosity than the other experiments the beams are locally defocussed - corresponding to higher $\beta^{\star}$ values - around LHCb's interaction point.

3.1.6 Expected LHC running conditions during start-up

The process of turning the LHC on for the first time, as one would imagine, will not be trivial - the design performance of the LHC will not be attained for some time.

At the time of writing the envisioned LHC running conditions during start-up are as follows. Firstly, and perhaps least significantly for the physics program at LHCb, the beam energies will be lower than the design values. A proton within one of the colliding beams at start-up will have an energy of 5TeV. Therefore, the maximum centre of mass energy possible in collisions at the LHC during start-up will be 10TeV, lower than the 14TeV that the machine will eventually reach. As shown in table 3.2, at this lower running energy the Z, $pp \rightarrow p + \mu^{+}\mu^{-} + p$ and $b\bar{b}$ production cross-sections are, respectively, 33%, 12% and 31% lower than the at $\sqrt{s}$ =14TeV. Secondly, and more significantly, the delivered instantaneous luminosities expected during the early running period are lower than the preferred LHCb running luminosity of $2 \times 10^{32} cm^{-2} s^{-1}$. As shown in table 3.3, it is currently planned that the LHC will commence operation with two proton bunches in each beam, before increasing to 43 bunches and subsequently 156 bunches per beam. At LHCb this will result in 1, 19 and 68 bunch crossings per beam revolution respectively. With 9×10^{10} protons in each bunch and a $\beta^{\star}$ value of 6m at LHCb this will result in average instantaneous luminosities of $1.7 \times 10^{29} cm^{-2} s^{-1}$, $3.3 \times 10^{30} cm^{-2} s^{-1}$ and $1.2 \times 10^{31} cm^{-2} s^{-1}$ respectively.

	Bunches	Crossings	$\beta^\star$	protons/bunch	μ	Luminosity
	2	1	$6m$	0.9×10^{11}	0.9	1.7×10^{29}
Start-up	43	19	$6m$	0.9×10^{11}	0.9	3.3×10^{30}
	156	68	$6m$	0.9×10^{11}	0.9	1.2×10^{31}
Design	2808	2106	$16.7m$	1.1×10^{11}	0.53	2×10^{32}

Table 3.3: Possible start-up scenarios at LHCb compared to the design specifications. Shown are: the number of bunches in each beam; the number of bunch crossings at LHCb in each revolution; the $\beta^\star$ value; the number of protons in each bunch; the average number of interactions per bunch crossing (μ); and the resulting average instantaneous luminosity (in units of $cm^{-2}s^{-1}$)

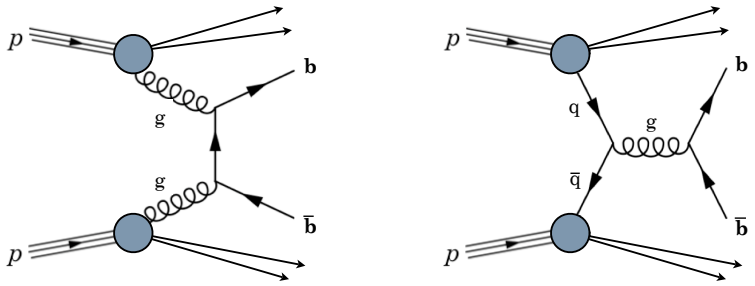

Figure 3.4: Feyman diagrams showing the dominant leading order $b\bar{b}$ production mechanisms - gluon fusion (left) and quark-antiquark annihilation (right).

3.2 The LHCb experiment

LHCb has been primarily designed and built to make $\mathcal{CP}$ violation and rare decay measurements in the b quark system. The production of B hadrons at the LHC has therefore influenced the layout of the detector. This section begins with a brief overview of B hadron production at the LHC and subsequently describes the various sub-detectors that make up LHCb.

3.2.1 Production of B hadrons at the LHC

The dominant $b\bar{b}$ production mechanisms at the LHC will be via gluon fusion and quark-antiquark annihilation (shown in figure 3.4). Table 3.2 shows the expected total and $b\bar{b}$ production cross-sections at the LHC for proton-proton centre of mass energies of 10TeV and 14TeV - the centre of mass energies that will be obtained at start-up and under nominal LHC running conditions respectively. The total and $b\bar{b}$ cross-sections must be extrapolated using data from previous hadron collider experiments, UA1, CDF and D0 for example, and have large associated uncertainties of the order $\sim$50%. Approximately one event in two hundred at the LHC will contain a $b\bar{b}$ pair. This corresponds to 10^{12} $b\bar{b}$ events per year at a single interaction point with a running luminosity of $2 \times 10^{32} cm^{-2}s^{-1}$.

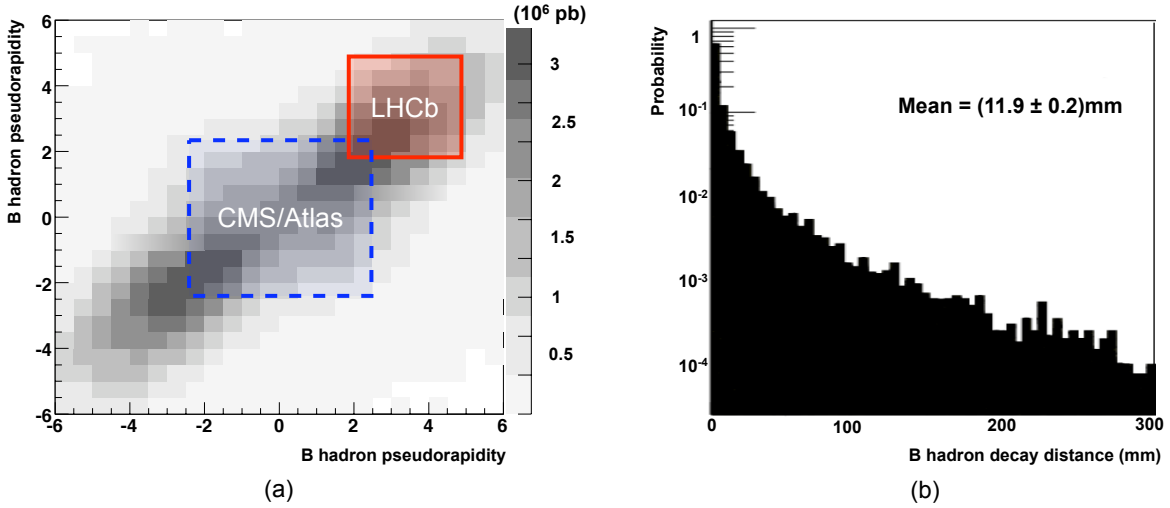

Figure 3.5: (a) The pseudorapidity correlation of B and $\bar{B}$ hadrons from $b\bar{b}$ production at the LHC. The regions accessible at LHCb and the general purpose detectors, ATLAS and CMS, are highlighted. (b) Probability distribution of the decay length of B hadrons at LHCb.

At LHC energies the incoming partons that produce $b\bar{b}$ pairs will have asymmetric momenta that are substantially larger than the mass of the b quark. This results in a production topology that has two important features. Firstly, the pseudorapidity[4], η, distributions for both the b and $\bar{b}$ are relatively flat in the range -5$<\eta<$5 with slightly lower values in the central region near η =0. This flat and broad pseudorapidity distribution means that b quarks will be preferentially produced at small polar angles at the LHC, i.e. either in the forward or backward direction with respect to the beam-pipe. Secondly, there is a strong correlation between the pseudorapidity values of the b and $\bar{b}$ meaning that if one of them is produced in the forward (or backward) direction then the other will also be produced in the same direction. These two points are illustrated in figure 3.5(a) which shows the pseudorapidity correlations, as predicted by the leading order PYTHIA event generator, for B and $\bar{B}$ hadrons resulting from the production of a $b\bar{b}$ pair at the LHC. The fact that both B hadrons are produced in the same direction is noteworthy since many $\mathcal{CP}$ violation measurements require the reconstruction of the decay of one B hadron while also tagging the flavour of the other B hadron. This can only be achieved if the decay products of both B hadrons lie within the region instrumented by the detector. The design of the LHCb detector exploits this production topology by only instrumenting a small portion of the forward hemisphere corresponding to the pseudorapidity range of 1.9$<\eta<$4.9 - thus reducing the complexity and cost of the detector while maintaining a high acceptance for both B hadrons. Although LHCb only covers $\sim$2.5% of the solid angle enclosing the interaction point there is a $\sim$15% chance that both B hadrons will lie within the LHCb acceptance. In comparison, ATLAS and CMS, which both cover $\sim$98.5% of the

[4]A particle's pseudorapidity, η, is related to the angle between the particle direction of flight and the direction of the incident protons, θ, at which the particle is produced in the following way $\eta = -\log[tan(\frac{\theta}{2})]$.

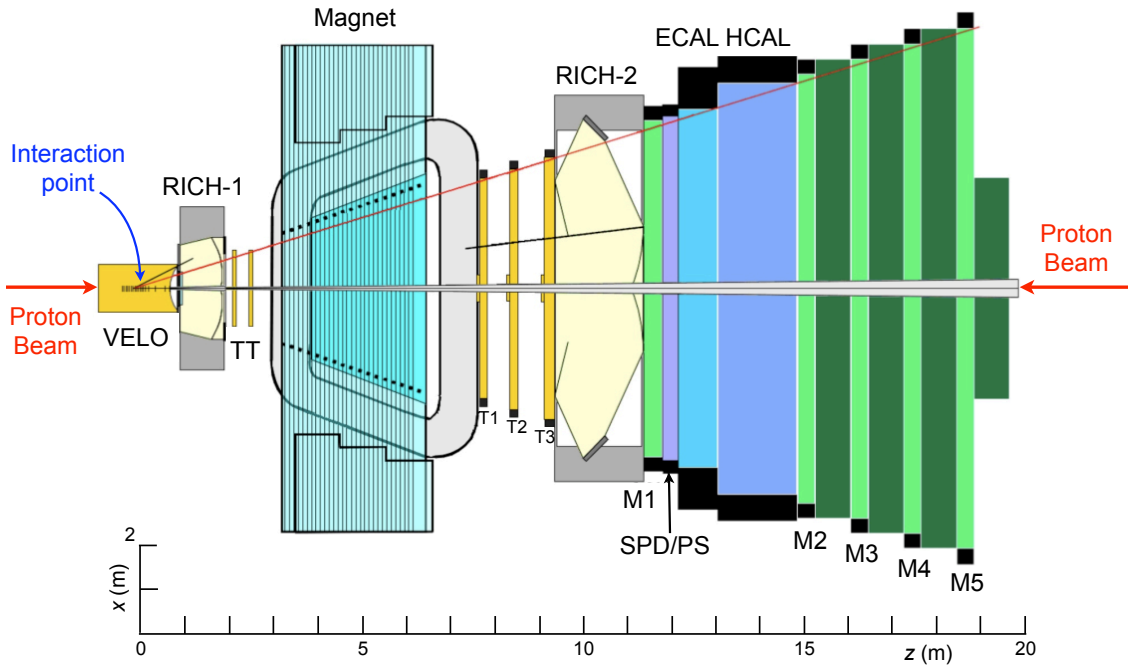

Figure 3.6: Overhead view of the LHCb detector in the bending x-z plane. The sub-detectors are labeled, they are the vertex locator (VELO) that will surround the interaction point, the two ring-imaging Cherenkov detectors (RICH-1, located between the VELO and TT detectors, and RICH-2), the tracking stations (TT, T1, T2 and T3), the magnet, the electromagnetic calorimeter (ECAL), the hadronic calorimeter (HCAL), the scintillating pad detector (SPD), the pre-shower detector (PS) and the five muon detectors (M1-M5) (from[36]).

solid angle[5], only contain both B hadrons $\sim$37% of the time. However, since LHCb can reconstuct B hadrons with lower transverse momenta - $P_T > 2GeV/c$ at LHCb compared with $P_T > 6GeV/c$ at ATLAS/CMS - the total visible $b\bar{b}$ cross-section at LHCb (230μb) is much larger than at ATLAS/CMS (100μb).

3.2.2 The layout of the LHCb detector

Since the two B hadrons resulting from proton-proton interactions at the LHC will be produced in the same forward or backward cone, LHCb has been designed as a forward spectrometer with an angular acceptance between 10 and 300 (250) mrad in the bending (non-bending) plane. This corresponds to an approximate coverage in pseudorapidity of $1.9 < \eta < 4.9$. The layout of the detector in the bending plane is shown in figure 3.6. Beginning with the detector closest to the interaction point and moving progressively further away along the beam-line, the components of LHCb are: the vertex detector (VELO); the first RICH detector (RICH-1); the Tracker Turicensis (TT); a warm dipole magnet; 3 tracking stations (T1, T2 and T3) - each of which consists of a silicon Inner Tracker (IT) and a gas straw tube Outer Tracker

[5] ATLAS and CMS cover the pseudorapidity range $|\eta| < 2.5$.

(OT); the second RICH detector (RICH-2); a calorimeter system consisting of a scintillating pad detector (SPD), pre-shower detector (PS), an electromagnetic calorimeter (ECAL) and an hadronic calorimeter (HCAL); and 5 muon stations (M1-M5) that are interleaved with 4 iron absorbers. These detector components are described in the following sections. The coordinate system of LHCb is defined as follows: the origin is at the interaction point; the z-axis lies along the direction of the beam pointing towards the muon system; the x and y axes lie in the horizontal and vertical (upward) directions respectively.

3.2.3 The tracking system

The tracking system at LHCb has a threefold purpose: it allows for precise vertexing, it enables the momentum of charged particles to be determined and, by extrapolating reconstructed tracks to hits in the RICH detectors, the calorimeters and the muon stations, it enables the identification of charged particles. The tracks of charged particles are reconstructed at LHCb using the VELO and four planar tracking stations: TT, T1, T2 and T3. The TT is located between the VELO and the magnet while T1-T3 are located downstream of the magnet in front of the RICH-2 detector. VELO and the TT are composed of silicon micro-strip detectors while the other tracking stations, T1, T2 and T3, are divided into two regions: the region closest to the beam-pipe, where the particle flux will be highest, consists of silicon micro-strips that are collectively known as the Inner Tracker (IT) while the outer regions are instrumented with gas-filled straw tube detectors that are collectively known as the Outer Tracker (OT).

The tracks of any charged particles that pass through the magnet aperture will be deflected by a magnetic field which has its main component along the y-axis and an integrated field of 4.2Tm. The momentum of a particle deflected in this way can then be determined since the difference in the slope of the particle's track in the VELO and the tracking stations downstream of the magnet (T1-T3) will be inversely proportional to the particles momentum. The crucial task of reconstructing primary and secondary vertices at LHCb is performed using the VELO.

The Vertex Locator

In chapter 2 we saw that, within the SM, b quarks can only decay into the lighter quarks u and c via the charged weak interaction - such flavor changing interactions do not occur via the electromagnetic or strong forces. This has an important consequence for the study of B quark systems: hadrons containing b quarks have long enough lifetimes to travel a measurable distance before they decay. The decay distance of B hadrons in the laboratory frame at LHCb - which has a mean value of $\sim$12mm - is shown in figure 3.5(b). By measuring the distance between the primary vertex, where the B hadron is produced, and the secondary vertex where it decays, B hadrons can be distinguished from a variety of different background processes which have kinematic properties that are similar to B hadron decays but lack this characteristic displaced secondary vertex. Precision measurements of primary and secondary vertices can be achieved by accurately reconstructing tracks in the region immediately surrounding the interaction point. At LHCb this task will be performed using a set of silicon detectors,

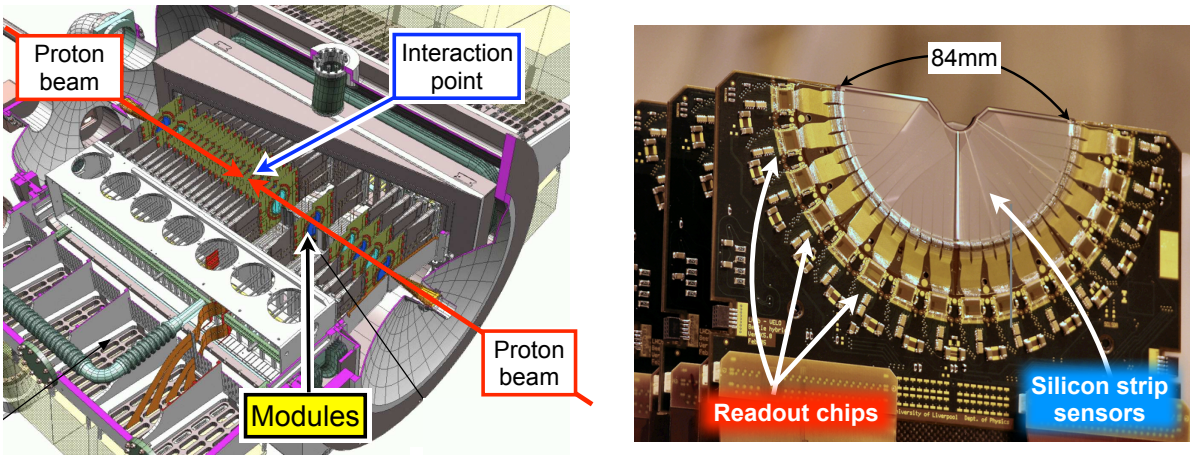

(a) (b)

Figure 3.7: (a) A 3D projection of the VELO detector with key components marked (from[34]). (b) A photograph of one of the VELO r sensors (from[33]).

collectively known as the Vertex Locator (VELO)[34], that will be placed close ($\sim$8mm) to the beam-line surrounding the interaction point.

The VELO detector consists of a set of 42 half-disc shaped modules that are interspersed over a length of $\sim$1m along the z-axis. As can be seen in figure 3.7(a) they are placed perpendicular to the beam pipe, 21 on one side of the beam and 21 on the other side. Each VELO module consists of two separate silicon detectors which are fixed to each other back to back. These two detectors are configured differently: one type is divided into radial strips and are known as r sensors while the other type, known as ϕ sensors, are divided into annular strips. This configuration was chosen to allow for the rejection of low impact parameter[6] tracks at an early stage in the trigger system. This is possible since the r sensors enable two dimensional tracks to be reconstructed in the r-z projection, providing a fast impact parameter measurement in the trigger system before the much slower to perform full three dimensional track reconstruction is available. In order to reconstruct primary and secondary vertices as accurately as possible, the sensitive area of the VELO modules will be located $\sim$8mm from the beam during data-taking. Since the radiation damage suffered by silicon sensors placed this close to the LHC beam would be very high during beam injection, the VELO has been designed so that the two VELO halves are retractable and will only be moved into position when the LHC beams are stable. To enable the sensors to be placed this close to the beams, the VELO tank is bonded directly to the beam pipe. However, in order to protect the LHC vacuum, the VELO modules are located inside a secondary vacuum that is separated from the primary LHC vacuum by a thin aluminium foil that can be seen in figure 3.8(a). This foil also acts as a radio-frequency

[6]The impact parameter of a track is defined to be the distance of closest approach between the particle's track and the primary vertex.

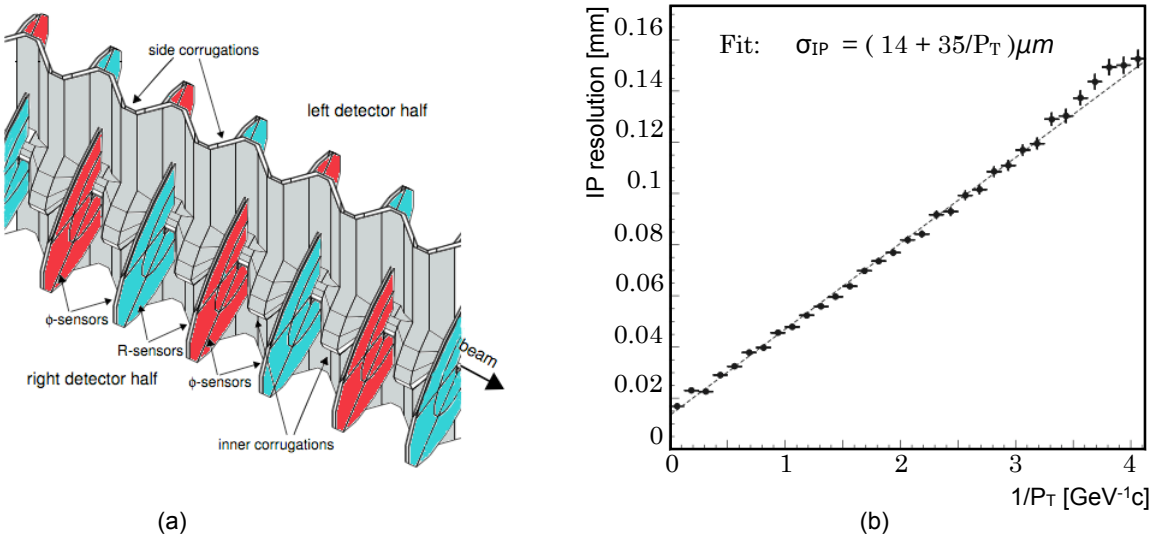

Figure 3.8: (a) Close up view of the RF foil with the detector halves in their closed positions. The ϕ and r sensors are highlighted using different colours (from[34]). (b) Impact parameter resolution as a function of $1/P_T$ for reconstructed tracks at LHCb (from[36]).

(RF) shield that protects the VELO electronics from electromagnetic effects caused by the high frequency LHC beam structure.

The resolution on impact parameter, vertex reconstruction and proper time measurements that will be made by the VELO have been estimated using Monte-Carlo simulations. Figure 3.8(b) shows the dependence of the impact parameter resolution of a track, σ_{IP}, on the inverse of the transverse momentum of that track - a relationship that can be parameterised as

$$\sigma_{IP} = (14 + 35/P_T)\mu m \tag{3.8}$$

where P_T is the transverse momentum of the particle and has the units GeV/c. The first term in equation 3.8 is due to the intrinsic resolution of the detector while the second term is due to multiple scattering. It is estimated that the VELO will reconstruct primary vertices with a resolution of $\sim 40\mu m$ in the z direction and $\sim 10\mu m$ in the x and y directions. The reconstruction resolution for secondary vertices will depend on the number of tracks coming from the vertex and will vary between $\sim 100\mu m$ and $\sim 300\mu m$ in z corresponding to an average lifetime resolution of $\sim 40 fs$.

In addition to the 42 VELO modules, 4 modules, consisting of r sensors only, are located at the upstream end of the VELO tank - i.e. the end facing away from the rest of LHCb. These modules are collectively referred to as the *Pile-up detector* and will be used in the electronic L0 trigger stage to reject events that contain multiple proton-proton interactions in a single bunch crossing. This will be done by quickly reconstructing any primary vertices in the event and rejecting any events with more than one (due to timing constraints the full VELO

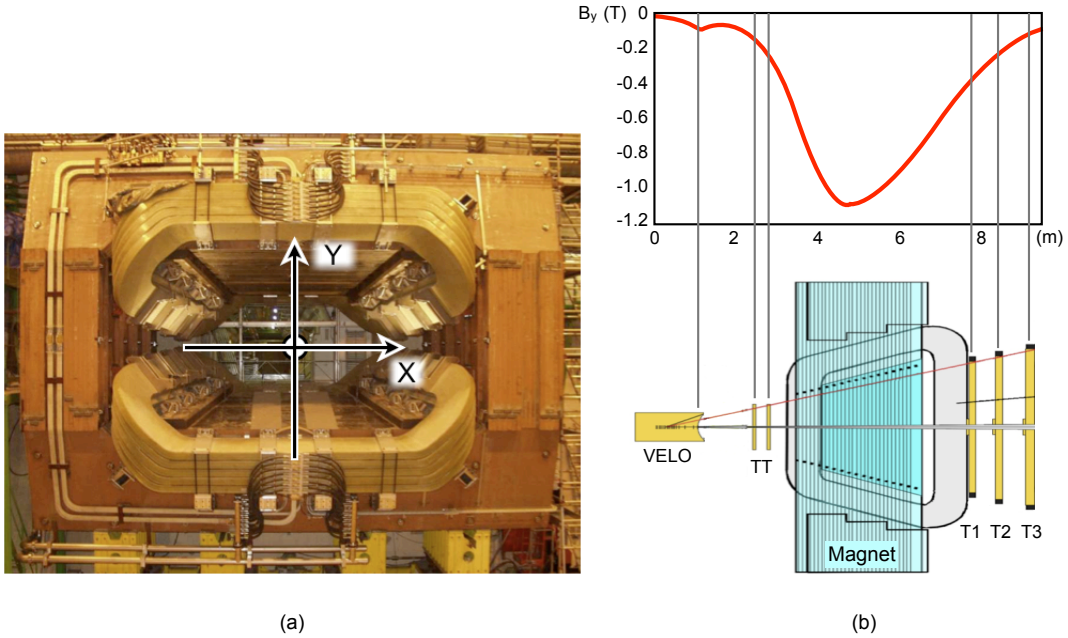

Figure 3.9: (a) The LHCb dipole magnet shortly after installation. The x and y axes are shown while the z-axis points out of the picture perpendicular to the page (from[33]). (b) The main B field component (B_y) shown as a function of displacement from the interaction point at $z = 0$. For the purpose of comparison the relative locations of the VELO and the tracking stations (TT, T1, T2 and T3) are shown.

reconstruction will not be available at L0). The Pile-up detector will reject $\sim$80% of events with multiple interactions while retaining $\sim$95% of single interaction events.

The magnet

The LHCb magnet[35], shown in figure 3.9(a), is a warm dipole consisting of two aluminum coils arranged inside an iron yoke. In order to minimise the field in the VELO, where fast straight track finding is essential for the trigger system, the magnet is located downstream from VELO between the TT and the tracking stations T1, T2 and T3. The magnet will provide an integrated field of $\int \vec{B} \cdot \vec{dl} \simeq$4.2Tm. The magnitude of the main B field component, B_y, as a function of displacement from the interaction point along the z axis is shown in figure 3.9(b). For particles with momenta $<$100GeV/c, that have track hits in at least 3 VELO modules and one hit in at least two layers of each of the three tracking stations (T1-T3), this field will enable the particles momentum to be determined with a resolution of $\delta P/P \sim 0.4\%$ - an uncertainty that increases to $\delta P/P \sim 1.5\%$ for tracks with momenta of 1TeV/c.

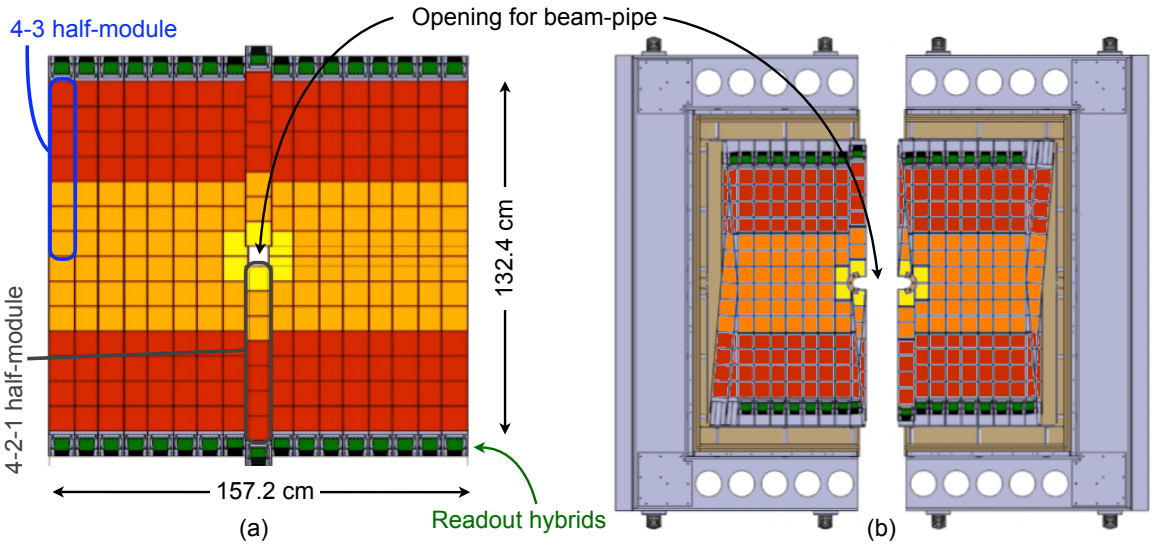

Figure 3.10: (a) The sensor arrangement in the (fourth) TT layer adjacent to the magnet. The colours signify the readout configuration (from[37]). (b) Graphic illustrating the module arrangement inside the TT enclosure (from[37]).

The Tracker Turicensis

The Tracker Turicensis (TT)[36] will be located between the magnet and RICH-1. The detector consists of four planar layers of p-on-n type silicon microstrip detectors that cover the polar angle between 15 mrad to 300 (250) mrad in the x-z (y-z) plane. The layers are arranged into two pairs, labeled TTa and TTb, that are separated in the z direction by 27cm. To enable the reconstruction of three dimensional space-points, the first and fourth layers have vertical readout strips while the second and third layers have readout strips that are rotated by $+5^\circ$ and -5° with respect to the vertical y-axis. Each plane is built out of half-modules that individually cover half of the height of the LHCb acceptance and have a width in the x direction of 9.6cm. Each half-module contains seven silicon strip sensors and has either a 4-3 or 4-2-1 readout configuration[7]. The half-modules with the 4-2-1 readout arrangement will be placed adjacent to the beam-pipe where the particle flux will be highest while the 4-3 half-modules will be located further away from the beam-pipe where occupancies are expected to be lower. In each silicon sensor there are 512 readout strips each with a width of 183μm. Due to clustering between neighbouring strips this results in a spatial resolution of $\sim$50μm. The detector planes in TTa have 15 half-modules above and below the beam-pipe, corresponding to an active area of 1.39m $\times$ 1.32m in the x-y plane, while the layers in TTb have 17 half-modules above and below the beam-pipe giving an active area of 1.57m $\times$ 1.32m. The module arrangement in the fourth TT layer is shown in figure 3.10(a). As shown in figure 3.10(b), the TT layers are located inside a light tight, electrically and thermally insulated box that is vertically split into two half-stations that can be retracted from the beam-pipe. Under running conditions the TT

[7] i.e. in modules with a 4-3 readout configuration four of the sensors are chained together giving an effective strip length of 37.7cm while the other three sensors are chained together giving a strip length of 28.3cm.

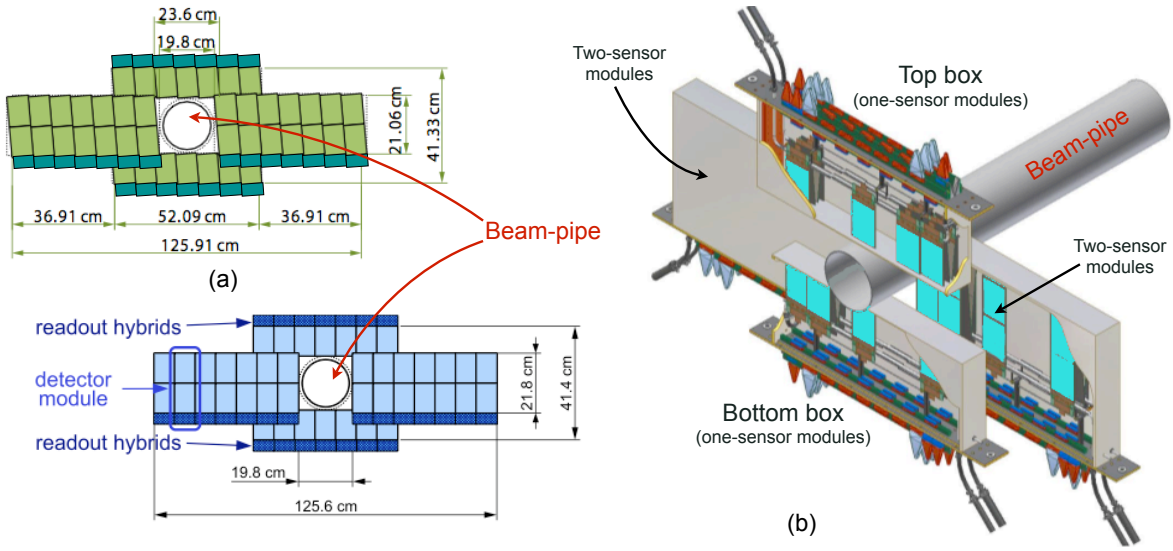

Figure 3.11: (a) Layout of two IT layers: one with a vertical readout configuration (bottom), and one with readout strips rotated by 5° with respect to the y-axis (top). The relative placement of the sensors and readout hybrids is shown (from[37]). (b) The placement of the four IT boxes in one of the T stations around the beam-pipe (from[37]).

box will be kept at a temperature of $5°C$ and will be continually flushed with nitrogen to avoid condensation on the electronics.

The TT has two functions. Firstly, since the magnetic field in the vicinity of the TT will be non-zero, hits in the TT can be combined with information from the VELO to provide approximate momentum measurements with associated uncertainties of $\sim$20%. Although less accurate than measurements using the other tracking stations, these measurements are invaluable in the trigger since track reconstruction using using the full tracking system (VELO-TT-T1-T2-T3) requires considerably more processing time. The second job of the TT is to improve the offline track reconstruction capabilities of LHCb. In particular the TT will enable the reconstruction of low momentum tracks that are bent outside the acceptance of the other tracking stations (T1-T3) and neutral particles, K_s^0 for example, that decay outside of the VELO.

The Tracking stations (T1-T3)

There are three tracking stations (T stations), labeled T1, T2 and T3, located between the magnet and RICH-2. Since the particle track densities will be lower further away from the beam line and due to cost issues, these tracking stations are each divided into two regions, an inner tracker (IT) and an outer tracker (OT).

The Inner Tracker: The IT[38] is a silicon strip detector that is located at the innermost region of the T stations where the particle flux is highest. As shown in figure 3.11(b), the IT component of each T station consists of 4 separate boxes of silicon sensors that are arranged

in a cross-shaped configuration. Like the TT box, these boxes are light tight, electrically and thermally insulated, cooled to $\sim 5^{\circ}C$ and continually flushed with nitrogen. The dimensions of the silicon sensors in the IT are similar to the sensors in the TT. The sensors have 512 readout strips each with a width of 198μm resulting in a spatial resolution of $\sim 55\mu$m. As shown in figure 3.11(a), the modules in the boxes above and below the beam-pipe consist of a single silicon sensor while the modules to either side of the beam-pipe have two sensors each. Each box contains four silicon layers with readout strips that are rotated by 0°, $+5^{\circ}$, -5° and 0° with respect to the vertical y-axis.

The Outer Tracker: As shown in figure 3.12(a), the remaining parts of the T stations not covered by the IT are instrumented by a straw tube detector called the Outer Tracker[39]. A single OT layer is made up of 14 long modules, with dimensions in x and y of $0.32\text{m} \times 4.8\text{m}$, and 8 short modules, placed above and below the IT, of dimension $0.32\text{m} \times 2.3\text{m}$. As shown in figure 3.12(b), these modules comprise two staggered layers of 64 straw tubes each. The straw tubes consist of a 25μm anode wire surrounded by a gas-filled 5mm diameter Kapton tube that acts as a cathode. Any charged particle that passes through one of the tubes will ionise the gas molecules and, due to a 1.5kV potential between the wire and the tube wall, the liberated electrons will drift towards the anode wire. The field strength is sufficiently large $\sim 100\mu$m from the wire for an electron avalanche to be initiated. In this way the transit of a charged particle through the tube can produce a detectable signal. The delay between a charged particle passing through one of the tubes and a signal reaching the corresponding anode is dominated by the drift time of the ionised electrons (in the OT this is a delay of $\sim$50ns). This delay can be used to determine the distance of closest approach between the track and the anode. Utilising this technique, the straw tubes in the OT are expected to provide a spatial resolution of 200μm. In a similar manner as the TT and IT, each T station will have two OT layers with wires in the vertical direction and two layers with wires rotated by $+5^{\circ}$ and -5° with respect to the y-axis.

3.2.4 Track reconstruction

Three different classes of charged particle tracks can be reconstructed at LHCb: *Long tracks*, *Upstream tracks* and *Downstream tracks*. Downstream tracks contain no information from the VELO and are reconstructed by combining hits in the TT and the three T stations. Downstream tracks are most commonly used to reconstruct long lived particles, K_S^0 and Λ particles primarily, that decay outside of the VELO tank. Tracks that have associated hits in the VELO and TT detectors but no hits in the T stations are known as upstream tracks. Upstream tracks are most often due to low momentum particles that are deflected outside the acceptance of the T stations. Occasionally, due to reconstruction inefficiencies in the T stations, high momentum particles are also reconstructed as upstream tracks. Long tracks are formed from the association of hits in the VELO and in the T stations. Although not a strict requirement, these tracks usually also have associated hits in the TT station. Since they have the highest reconstruction quality and momentum resolution, long tracks have been used exclusively in the physics studies presented in this thesis.

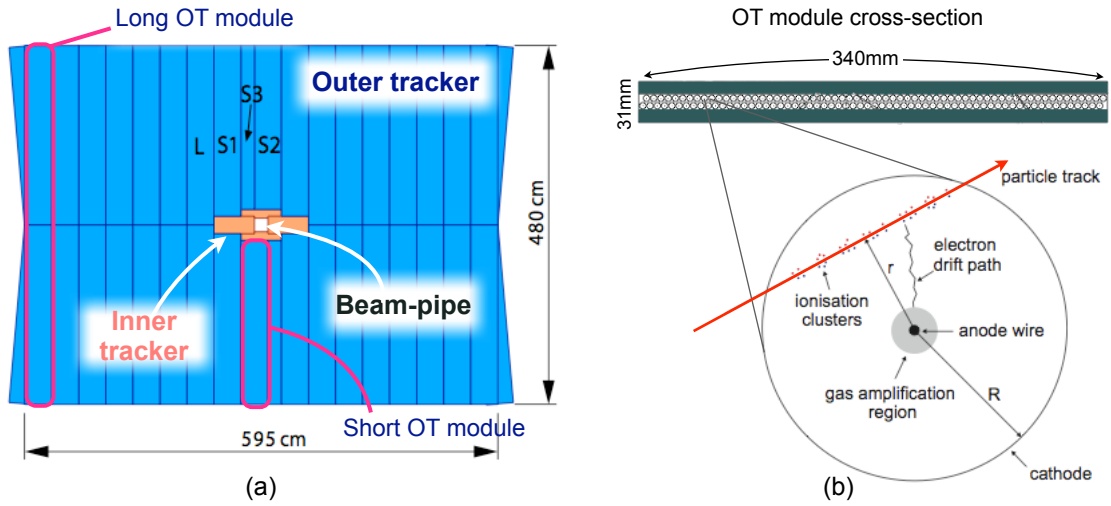

Figure 3.12: (a) Layout of the OT and IT around the beam-pipe. The dimensions of the long and short OT modules are highlighted (from[39]). (b) Cross-section of an OT module in the x-z plane and a magnified view showing the interior of one of the straw tubes (from[39]).

Long track reconstruction

The offline reconstruction of long tracks at LHCb is achieved by executing a sequence of algorithms. Due to the importance of long tacks in the physics studies presented in chapters 4 and 5, a brief description of each algorithm will now be given in the order in which they are executed.

1. VELO seeding: Long track reconstruction at LHCb commences with the reconstruction of track stubs in the VELO. These track stubs, commonly known as VELO seed tracks, are reconstructed by matching three-dimensional space points, known as VELO hits, that are created by combining r and ϕ VELO clusters. Since the integrated magnetic field inside the VELO is small ($\sim$0.05Tm), these track stubs are reconstructed by fitting a straight line to hits in at least 3 VELO modules. The resulting track segments serve as seeds for the other track finding algorithms.

2. Forward tracking: The forward tracking algorithm[40], shown schematically in figure 3.13, begins by combining each VELO seed track with every reconstructed hit in the T stations. Assuming no multiple scattering, for a given VELO seed and a single hit in the T stations the trajectory of the track through the detector can be determined. For each combination of a VELO seed track and a T station hit, the track trajectory is parameterised by a straight line in the y-z plane and by a parabolic fit in the x-z plane. A search for additional hits around this trajectory is then performed. In order to keep combinatorics low, this search is only carried out within a small cone surrounding the trajectory. Any track candidate that has confirming hits in each of the three T stations is reconstructed as a long track. About 90% of the long tracks that are reconstructed at LHCb are found by the forward tracking algorithm. In order to

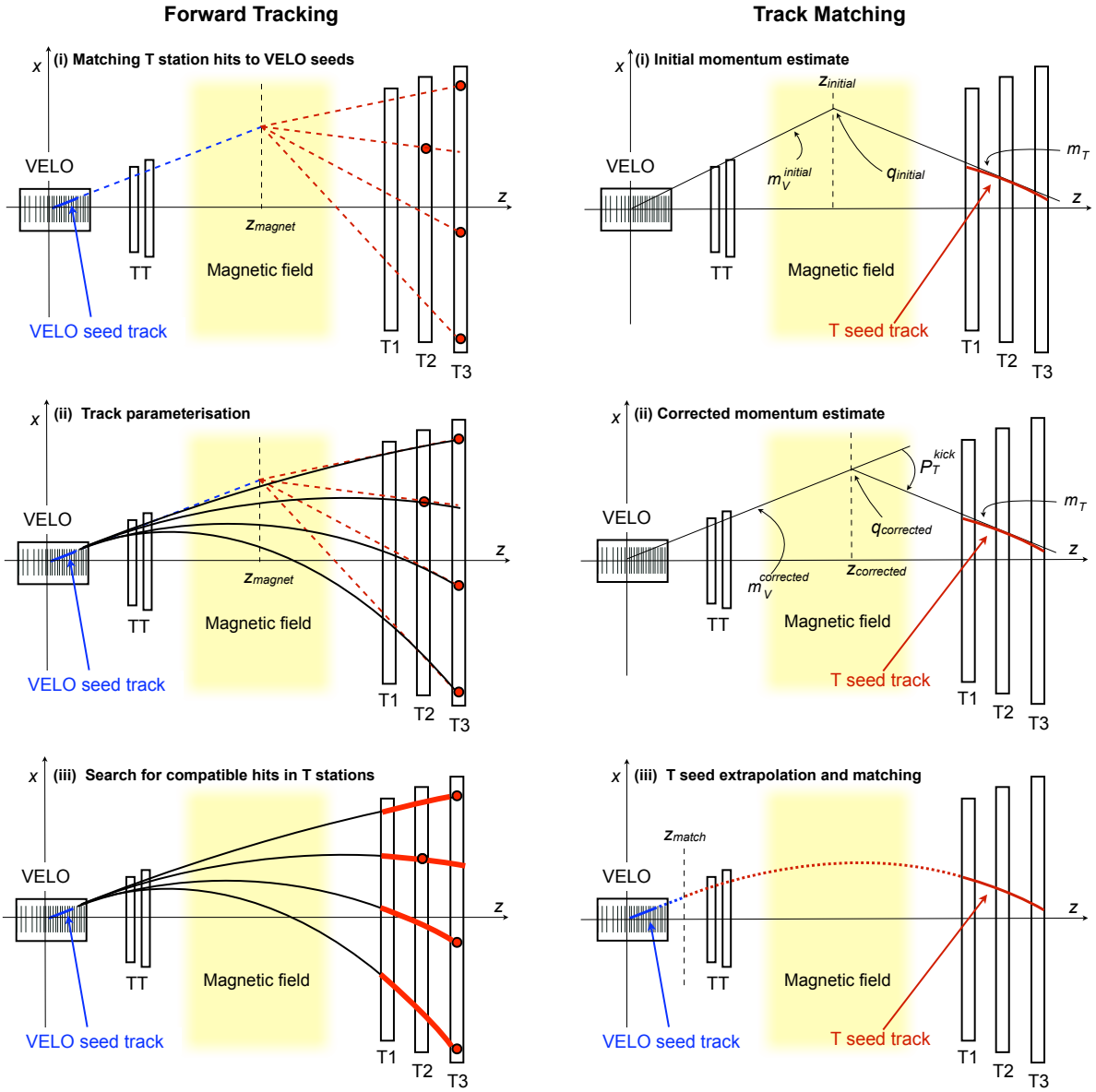

Figure 3.13: Schematic drawings showing the main steps in the forward tracking algorithm (left) and track matching algorithm (right).

reduce the number of clone tracks[8] that are found, the hits that are included in any of the long tracks found by the forward tracking algorithm are discarded for use in the subsequent track search algorithms.

3. T seeding: By combining T station hits that were not associated to tracks by the forward tracking algorithm, track stubs can also be reconstructed in the three tracking stations after the magnet (T1-T3)[41]. Unlike VELO seed tracks which are parameterised as straight lines, with a typical lever arm of 1.5m and an integrated field of $\sim$0.5Tm in the T station region, T seed tracks bend by a few cm over this distance and are therefore parameterised as parabolae.

4. Track matching: The track matching algorithm, shown schematically in figure 3.13, attempts to match the reconstructed T seed tracks to any VELO seed tracks that were not reconstructed as long tracks by the forward tracking algorithm. For this to be done, one or other of the seed tracks must be propagated through the magnetic field. Since the trajectory of a charged particle in a magnetic field is dependent on the momentum of the particle, this propagation is only possible if the momentum of the particle is known. Due to the presence of the stray B field, the momentum of the T seeds can be calculated with an uncertainty of $\sim$10%. However, a better momentum estimate can be obtained using the so called p-kick method which is shown schematically in figure 3.13. The p-kick method relies on two assumptions. Firstly, it is assumed that the particle originated from the primary interaction point located at the x-y-z coordinate (0,0,0). Secondly, the assumption is made that the effect of the magnetic field can be approximated by a single instantaneous kick to the particles trajectory at the point on the track, q, where the integrated magnetic field along the track in one direction is equal to the integrated field along the track in the opposite direction, i.e.

$$\int_{-\infty}^{q} B.dl = \int_{q}^{\infty} B.dl \tag{3.9}$$

As an initial estimate, q is assumed to lie on the x-y plane located at the z position, $z_{initial}$, where the integrated magnetic field along the z-axis betweeen the origin and $z_{initial}$ is equal to half of the total integrated field (i.e. 2.1Tm). The slope of the T seed at the third tracking station, m_T, is then extrapolated to this plane giving a point of intersection $q_{initial}$. The line joining $q_{initial}$ and the origin gives an initial estimate of the track slope inside the VELO, $m_V^{initial}$. For tracks that originate at a vertex near the primary interaction point and that have momenta $<$100GeV/c, the difference between these two slopes, $m_T - m_V^{initial}$, gives a momentum estimate with an uncertainty of 1-2%. The uncertainty on this momentum measurement can be reduced by estimating the location of q more precisely. An improved estimate of q can be achieved by finding the point on the path defined by the two slopes $m_V^{initial}$ and m_T where the values of integrated field in both directions along the path are equal. The z position of this point, $z_{corrected}$, defines a new focal plane in x-y. Propagating the slope of the T seed track to this new focal plane allows for a more accurate determination of the track slope in the VELO region, $m_V^{corrected}$, and consequently enables the track momentum to be calculated with a smaller uncertainty. For tracks with momenta of $<$100GeV/c this iterative p-kick method provides a momentum estimate with an associated uncertainty of $\sim$0.7%. Using the momen-

[8] A clone track is a track that does not correspond to the path of a real particle and results from the incorrect matching of detector hits.

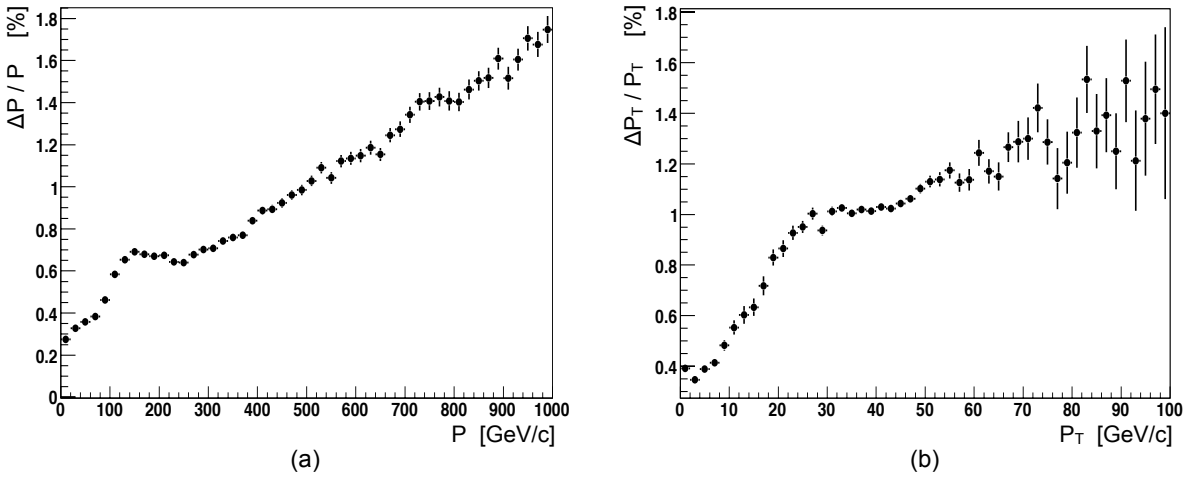

Figure 3.14: Expected momentum (a) and transverse momentum (b) resolutions for long tracks reconstructed at LHCb. The long tracks in the sample shown here are due to muons originating from two-photon fusion and Z boson decay.

tum obtained with the p-kick method, the T seeds are then extrapolated through the magnetic field to a plane, located adjacent to the last VELO station at z_{match} =0.754m, where they are matched to the VELO seeds.

5. TT search and track refit: Once a long track has been found using either the forward tracking or track matching algorithms, a search is performed in the TT station for compatible hits. Any compatible hits that are found are added to the track. For tracks with momenta less than 100GeV/c, the addition of two TT clusters to a long track reduces the uncertainty on the momentum estimate for the track to $\sim$0.35%. Finally, the reconstructed track is refitted using a Kalman filter[42] which improves the track fit by correctly taking into account the effects of multiple scattering and the energy dissipated in the detector materials.

Tracking performance

The momentum and transverse momentum resolutions of long tracks at LHCb have been examined using a Monte-Carlo sample containing long tracks due to muons originating from two-photon fusion and Z boson decay. The resolutions as a function of momentum and transverse momentum are shown in figures 3.14(a) and 3.14(b) respectively. The uncertainty on the momentum determination of long tracks with momenta $\sim$10GeV/c is expected to be $\sim$0.3%. To good approximation this uncertainty increases linearly with momentum and is expected to be $\sim$1.5% for tracks with momenta of 1TeV/c. The tracking efficiency at LHCb has been studied using Monte-Carlo simulation in ref. [43]. The average efficiency for reconstructing long tracks with $p > 5GeV/c$ was determined to be $(94.31 \pm 0.08)\%$ with a total ghost rate for long tracks of $(11.53 \pm 0.06\%)$.

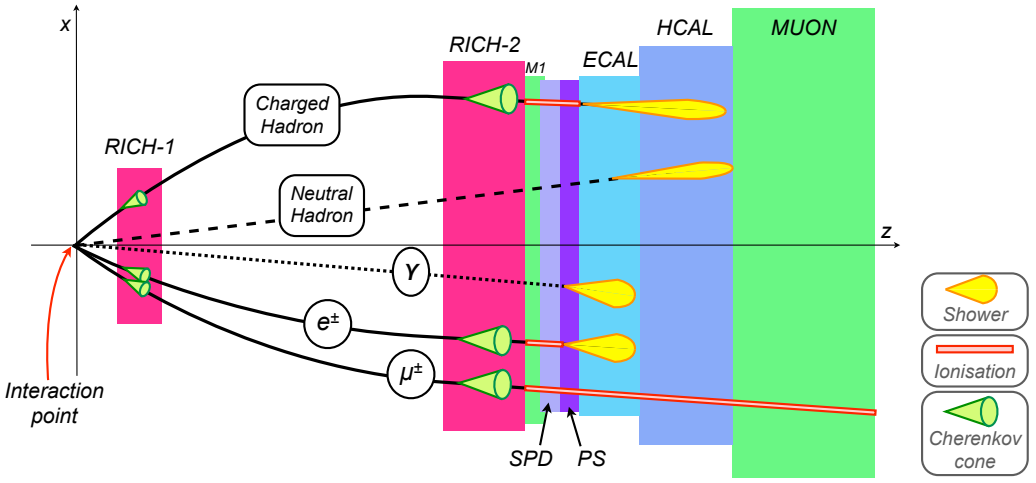

Figure 3.15: Schematic drawing showing how the information from different components of the LHCb particle identification system can be used to identify and measure the positions and energies of different particle types. It should be noted that, since neutral pions decay predominantly to two photons ($BR(\pi^0 \to \gamma\gamma) \simeq 0.99$) close to the interaction region ($c\tau_{\pi^0} \simeq 25nm$), the detector signature of a π^0 is similar to the signature of a photon. Though, due to the prescence of two photons in the final state, the electromagnetic shower will have a larger lateral size.

3.2.5 The particle identification system

At LHCb particle identification (PID) will be provided by: a calorimeter system consisting of a scintillator pad detector (SPD), a preshower detector (PS), an electromagnetic calorimeter (ECAL) and an hadronic calorimeter (HCAL); a muon system consisting of five detector stations (M1-M5); and two ring-imaging Cherenkov detectors (RICH-1 and RICH-2). Primarily electrons and photons will be identified by the ECAL, muons by the muon stations, charged hadrons by the HCAL and RICH detectors and neutral hadrons by the calorimeters. However, in practice the detectors will often be used in combination to identify the particles. An overview of how each component of the LHCb PID system can be used in conjunction with the other elements to identify a variety of different particle types is shown in figure 3.15. Each of the components of the PID system will be discussed in turn in the following sections.

The RICH detectors

One of the requirements of many $\mathcal{CP}$ measurements in the b system is the ability to distinguish between a variety of different hadronic final states - in particular the ability to distinguish between pions and kaons. As an example consider the decay $B^0_d \to \pi\pi$, which will be important for measuring the unitarity triangle angle γ, and must be separated from topologically identical decays such as $B^0_d \to K\pi$. The separation of charged hadrons will be achieved at LHCb by employing two Ring Imaging Cherenkov (RICH) detectors[44, 36] that will correctly identify charged particles by assigning their mass hypothesis.

Cherenkov radiation is emitted in a cone when a charged particle passes through a medium with a velocity v that is greater than the speed of light in that medium, i.e. $v > c/n$ where n is the refractive index of the material and c is the speed of light in a vacuum. The polar angle, θ_c, at which this light will be emitted relative to the particle direction of flight is given by

$$cos\theta_c = \frac{1}{n\beta} \tag{3.10}$$

where $\beta = v/c$. RICH detectors exploit this effect by determining the particle's velocity through a measurement of the emitted photons polar angle θ_c. In combination with the momentum information from the tracking system, this velocity measurement can then be used to determine the mass, and therefore the particle type, of any charged particle that passes through the detector. A particle will only radiate Cherenkov light when its momentum exceeds the threshold given by: $\beta_t = 1/n$. Materials with large refractive indices are therefore needed to identify low momentum particles. Conversely, for higher momentum values smaller refractive indices are often optimal since they result in smaller θ_c values thus aiding reconstruction. For these reasons RICH detectors often use a number of different radiators thereby enabling particle identification over a large momentum range.

As shown schematically in figure 3.16(a), the Cherenkov light that is produced by charged particles that pass through the radiator material of the LHCb RICH detectors is redirected via a set of mirrors to an array of Hybrid Photon Detectors (HPDs) located outside of the LHCb acceptance. The projections of these light cones form rings on the HPDs. In principle, by measuring the radius of the ring associated with a given particle track, the angle θ_c, and thus the particle's velocity, can be determined. This velocity measurement can then be combined with the momentum measurement from the tracking system to estimate the mass of the particle. In practice, LHCb uses a global likelihood fit to all photon hits in the event to assign particle hypotheses to all tracks in the event.

There are two RICH detectors in LHCb. They are called simply RICH-1 and RICH-2 and are located upstream and downstream of the magnet respectively.

RICH-1: The first RICH detector is located between the VELO tank and the TT box and covers the full LHCb acceptance. By placing the detector near to the interaction point, lower momentum particles, which have relatively large polar angles with respect to the beam-line, can be identified using a smaller detector volume than would be needed by a detector located after the tracking system. The presence of RICH-1 therefore enables the physical size, and by extension the cost, of RICH-2 to be reduced[9]. RICH-1 specialises in identifying low momentum particles with momenta between 1GeV/c and 60GeV/c. Two different radiators are used in RICH-1: a 5cm thick silica aerogel, with a refractive index of n=1.03, is located adjacent to the exit widow of the VELO tank and is used to identify particles with momenta below 10GeV/c; the primary radiator of RICH-1 is C_4F_{10} gas, with a refractive index n=1.0014, which is used to reconstruct particles with momenta of up to 60GeV/c.

[9]There is a major disadvantage to this layout: the prescence of RICH-1 inside the tracking system causes additional multiple scattering that degrades the momentum resolution.

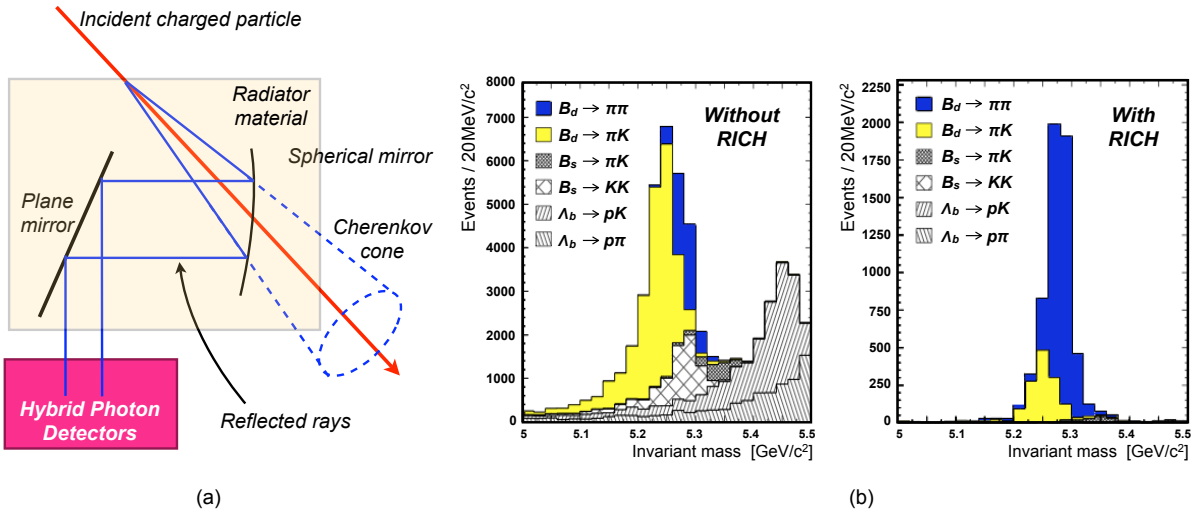

Figure 3.16: (a) Schematic drawing illustrating the operation of the RICH detectors at LHCb. The incident charged particle produces a Cherenkov cone that is redirected to a set of hybrid photon detectors via a set of mirriors. (b) The invariant mass distributions of $B_d \to \pi\pi$ candidates, due to both signal and a variety of background processes, with (right) and without (left) the information from the LHCb RICH detectors (from[44]).

RICH-2: The second RICH detector specialises in identifying higher momentum particles and therefore has a polar angle acceptance of 10-120mrad giving a momentum coverage of 20-100GeV/c. It only has one radiator - CF_4 gas with a refractive index of n=1.0005.

The combined RICH system will provide a 3σ separation between pions and kaons in the momentum range 1-100GeV/c. As an example, the impact of the information from the RICH detectors on the reconstruction of $B_d \to \pi\pi$ events is shown in figure 3.16(b).

The calorimeters

The calorimeter system[45] is designed to identify electrons, photons and hadrons and measure their positions and energies. This information is used both in the electronic L0 trigger, the earliest trigger stage at LHCb, to identify high P_T particles that are indicative of B hadron decays, and in the offline reconstruction.

The calorimeter system at LHCb, like many other particle physics experiments, is based on the exploitation of particle showering, due to both electromagnetic and hadronic interactions, that is caused by particles as they pass through a material. Electromagnetic showering, shown (qualitatively) in figure 3.17(a), can occur when charged particles or photons pass through matter and is due to two processes: the emission of bremsstrahlung radiation by charged particles and pair production caused by photon-nuclei interactions. The secondaries produced in these processes - mainly photons, electrons and positrons - can cause a cascade to develop

through repeated bremsstrahlung and pair production interactions. The electromagnetic showering of charged particles is primarily driven by the rate of energy loss via bremsstrahlung radiation - a rate that is given by

$$\left(\frac{dE}{dx}\right)_{brem} = -\frac{E}{X_0} \tag{3.11}$$

where E is the energy of the particle and X_0 is the distance, known as the radiation length, over which a charged particle will on average lose 63% of its energy through bremsstrahlung. For a particle of mass m_I and charge eZ_I traversing a material of density ρ, atomic number Z and mass number A, the radiation length is given by

$$X_0 \propto \left(\frac{m_I^2 A}{\rho Z_I^4 Z^2}\right) \tag{3.12}$$

This relation has two major implications for electromagnetic calorimetry. Firstly, since it is desirable to have a radiation length that is as small as possible, thereby reducing both the physical size of the calorimeter and the lateral shower dimension, the material chosen for the construction of an electromagnetic calorimeter should have a density, atomic number and mass number such that the ratio $(\rho Z^2/A)$ is as large as possible. Secondly, the fact that the energy loss via bremsstrahlung is inversely proportional to the incoming particle's mass squared has an important consequence: at LHC energies electrons and positrons are the only charged particles that will initiate electromagnetic showers. When an electron passes through a material with atomic number Z, energy losses due to bremsstrahlung will begin to dominate over the energy losses due to ionisation when the electrons energy exceeds 550MeV/Z. In contrast, bremsstrahlung only begins to dominate for muons, the second lightest charged particle after the electron, when the muons energy exceeds 22TeV/Z - corresponding to $\sim$270GeV for a muon passing through lead - a value that is higher than the typical energies of charged particles that will be produced at the LHC. Consequently, the energies and positions of charged hadrons, which have masses that are larger than the mass of the muon, are instead measured by recording the secondaries produced in strong interactions between the incoming hadron and the atomic nuclei of the detector material. At high energies these hadronic interactions are characterised by the multi-particle production of pions and nucleons originating from hadron-nuclei scattering processes and the nuclear decay of excited nuclei. These secondary particles can also interact via the strong interaction resulting in a particle shower that continues until all of the secondary particles are slowed down and stopped. Unlike electromagnetic showering, hadronic shower development is not characterised by the radiation length but is instead dependent on the nuclear interaction length[10], λ_I, of the absorbing material - a parameter that depends on the density and atomic number of the material in the following way:

$$\lambda_I \sim \frac{35A^{1/3}}{\rho} \tag{3.13}$$

[10]The nuclear interaction length of a material is the mean distance that a hadron will travel in that material before it comes close enough to an atomic nucleus for a strong interaction to occur.

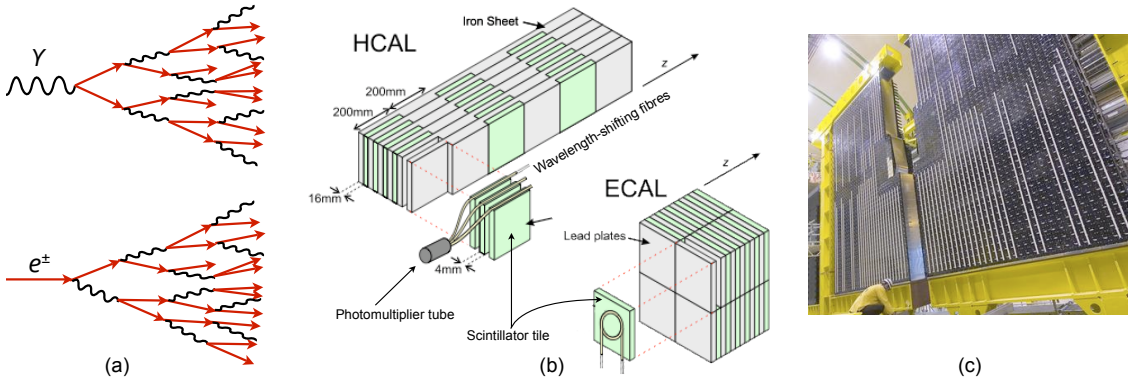

Figure 3.17: (a) Schematic drawing showing the progression of an electromagnetic shower, due to a combination of bremsstrahlung radiation and pair production, caused by either an incident photon or electron. Photons are represented by curvy black lines and electrons and positrons by red arrows. (b) The arrangement of the HCAL and ECAL scintillator and absorber (either lead or iron) tiles at LHCb. The positioning of the wavelength shifting fibres and photomultiplier tubes are also shown (from[45]).(c) The electromagnetic calorimeter during installation (from[33]).

In an analogous way to electromagnetic calorimeters, the absorber material of an hadronic calorimeter is usually chosen such that λ_I is as small as possible. Of particular importance for the operation of many hadronic calcorimeters is the fact that a portion of the showering initiated in a hadronic calorimeter is due to electromagnetic processes - primarily caused by the decay $\pi^0 \rightarrow \gamma\gamma$. In a similar way to electromagnetic calorimeters, the photons that result from this electromagnetic showering can be used to measure the energy of the incoming hadron.

As shown in figure 3.17(b), the calorimeters used at LHCb consist of alternating layers of absorber and detector material, a configuration that is generally referred to as a *sampling calorimeter*. The absorber layers are made from dense materials chosen to degrade the energy of incident particles and develop electromagnetic or hadronic showers while the detection layers are made from a scintillating material that records the fraction of the incoming particle's energy that is converted into photons. Since this is only a fraction of an incident particle's energy, the energy resolution of a sampling calorimeter is primarily determined by the relative fluctuations of this detected fraction.

The LHCb calorimeter system consists of four components that are positioned in the following order between M1 and M2: a scintillator pad detector (SPD), a preshower detector (PS), an electromagnetic calorimeter (ECAL) and an hadronic calorimeter (HCAL). Each of these components is divided vertically into two halves enabling the detectors to be retracted from the beam-line.

SPD/PS: The SPD and PS detectors provide valuable information about the initial shower development that improves the particle indentification capabilities of the calorimeter system. The SPD enables charged and neutral particles to be differentiated by recording the ionisation energy deposited by charged particles in a 15mm thick scintillator detector before showering occurs. The SPD is followed by a 12mm thick lead wall that is thick enough to initiate

electromagnetic showers but insufficient to cause significant hadronic showering. A second 15mm thick scintillator layer placed behind this lead wall, known as the PS, therefore enables electrons and hadrons to be differentiated. The scintillation light collected by both the SPD and PS is directed via wavelength shifting (WLS) fibres to multianode photomultipliers that are located outside the LHCb acceptance.

ECAL: The rest of the electromagnetic showering due to electrons and photons is recorded by the ECAL which is shown in figure 3.17(c). It consists of 66 alternating layers of 4mm thick scintillator sheets and 2mm lead sheets. Lead was chosen as the absorber material since its high atomic number (Z=82) encourages both bremsstrahlung and pair-production. The scintillation light produced in the ECAL is transported to a set of photo-multipliers via WLS fibres. The ECAL has an energy resolution over the range 1-200GeV of

$$\frac{\sigma(E)}{E} = \frac{10\%}{\sqrt{E}} \bigoplus 1.5\% \tag{3.14}$$

where the energy E is expressed in GeV and the symbol $\bigoplus$ denotes addition in quadrature. The first term on the right is statistical in nature and is due to the fact that only a portion of energy in the electromagnetic shower is recorded. The second term is due to systematic effects such as the detector non-uniformity or calibration uncertainty.

HCAL: Although hadrons may develop an initial shower in the ECAL, the majority of the hadron's energy will be deposited in the HCAL. The HCAL consists of alternating layers of iron and scintillator, being 16mm and 4mm thick respectively. Again WLS fibres transport the scintillation photons to the photo-multipliers. The energy resolution is

$$\frac{\sigma(E)}{E} = \frac{80\%}{\sqrt{E}} \bigoplus 10\% \tag{3.15}$$

The muon system

Since muons can not produce hadronic showers and are minimum ionising at LHC energies, they are not stopped by the calorimeter system[11]. They are therefore primarily identified by a separate set of detectors. The muon system at LHCb[46] contains a set of five detector planes (labeled M1-M5) and has an inner and outer polar angle acceptance of 20mrad (16mrad) and 306mrad (258mrad) in the bending (non-bending) plane. The first station, M1, is located upstream from the calorimeters while the other four stations, M2-M5, are located downstream from the calorimeters. This separation allows for an approximate momentum measurement to be made at the L0 trigger level. M2-M5 are interspersed with three 0.8m-thick iron plates that will absorb hadrons, photons and electrons thereby reducing the possibility that these particles will be mis-identified as muons. Each station is divided into four regions, R1-R4, with R1 closest to the beam line and R4 the furthest away. Since the particle flux will be highest near the beam-line and will be smaller for large polar angles, the granularity is finest in R1 and gets progressively worse in the regions further away from the beam-line. Additionally,

[11] However, muons do deposit a small amount of energy in the other detectors via ionisation.

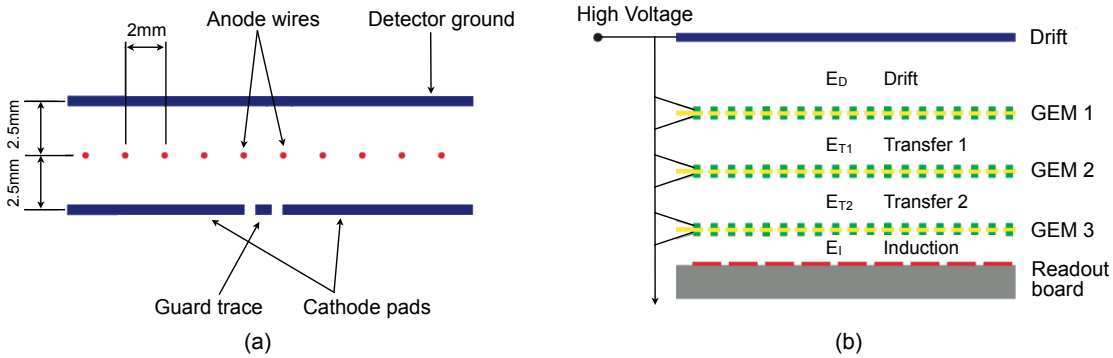

Figure 3.18: Schematic diagrams showing: (a) the cross-section of a Multi-Wire Proportional chamber (from[46]); (b) the cross-section of a triple GEM detector (from[46]).

since the bending force of the magnet is dominated by its x component, in order to provide a more accurate momentum measurement the granularity in the x direction is finer than in the y direction.

The muon stations are primarily composed of Multi-Wire Proportional Chambers (MWPC). As shown in figure 3.18(a), each of these chambers consist of a 5mm gas filled space with a series of wires aligned in the centre. Any muon that passes through one of the chambers will ionise the gas molecules and, due to a 3kV potential between the anode wires and the chamber wall, the liberated electrons will drift towards the anode wires. As the electrons are accelerated towards the wires they ionise further atoms in the gas resulting in an electron avalanche. The resulting ions and liberated electrons will provide a detectable signal.

Due to the fact that it is subject to a very high particle flux, the inner-most region of the M1 station is instrumented using a different detector technology - Gas Electron Multiplier (GEM) detectors. As shown in figure 3.18(b), these detectors consist of a gas volume and three layers of thin kapton foils that have multiple holes of diameter $\sim 70\mu$m. These foils are interleaved between anode and cathode planes. When a charged particle passes through the gap between the cathode and the first foil it ionises atoms in the gas. The resulting electrons are then accelerated by an electric field through the 3 foils. As the electrons pass through the holes in the foil, where the electric field is very high, greater and greater numbers of electrons are produced. Finally, after the last foil is traversed the charge is collected on cathode strips.

3.2.6 Muon identification

Muon detection is vital both in the L0 trigger stage, which looks for muons with high transverse momentum, and in the offline reconstruction. Since both of the physics channels studied in this thesis have dimuon final states, the following sections provide a brief summary of how muon identification is performed both in the trigger system and in the offline reconstruction.

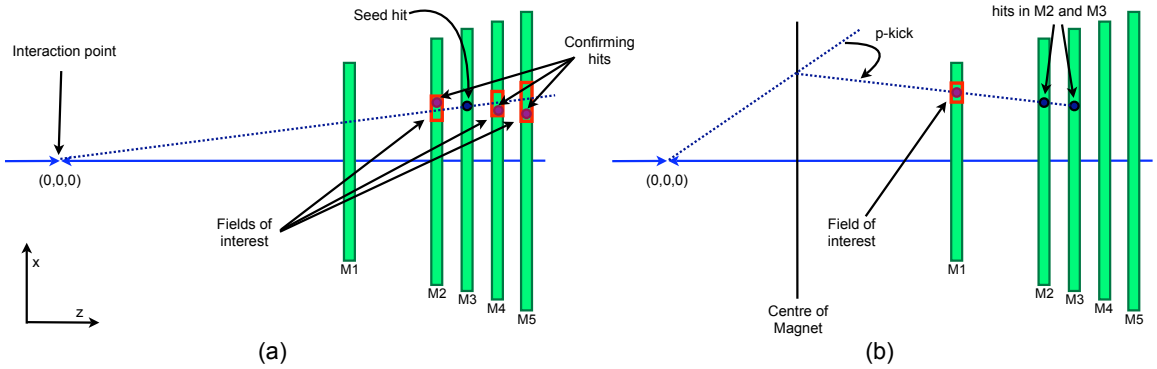

Figure 3.19: Schematic diagram illustrating muon track finding in the L0 trigger. (a) Beginning with a seed hit in M3 the algorithm searches for compatible hits in fields of interest in M2, M4 and M5. (b) If compatible hits are found in M2, M4 and M5, a search is performed in M1 by extrapolating the line joining the hits in M2 and M3 and opening up a field of interest. If a hit is found in M1, the line joining this hit and the hit in M2 is extrapolated to the centre of the magnet and the p-kick method is used to estimate the momentum of the muon candidate.

Muon identification in the trigger system

The Level-0 muon trigger looks for muon tracks that have large transverse momenta. Since the information from the tracking system is not available at the L0 trigger stage (see section 3.2.8 for more details), the track finding is performed using the muon system. For each hit in M3, the straight line passing through the hit and the interaction point is extrapolated to M2, M4 and M5. As shown in figure 3.19(a), a search is performed for hits in these stations in search windows, called fields of interest (FOI), that are approximately centred on the straight-line extrapolation. If compatible hits are found in the other three stations (M2, M4 and M5), a search is performed in M1 by making a straight-line extrapolation from M3 and M2 and identifying in the M1 field of interest the hit closest to the extrapolation point. Using the p-kick method described in section 3.2.5, the slope of the line joining the M1 and M2 hits in the x-z plane is then used to make a momentum estimate for the muon candidate (see figure 3.19(b)). For muons with momenta below 150GeV/c, the uncertainty on this momentum estimate has an uncertainty of $\sim$20%. Since the total absorption length of the muon system and the calorimeters is $20\lambda_I$, only muons with momenta above $\sim$6GeV/c will penetrate all the way to M5 and be reconstructed by the L0 trigger algorithm.

Muon identification in the other trigger levels is as follows. The L1 trigger reuses the muon objects found by the L0 trigger: the muon identification is not improved but a more accurate momentum estimate is obtained using the track slope provided by the VELO. Since the information from all of the sub-detectors is available in the High Level Trigger (see section 3.2.8), the L0 muon objects are not used in the HLT, instead muon identification is performed in the same way as in the offline reconstruction.

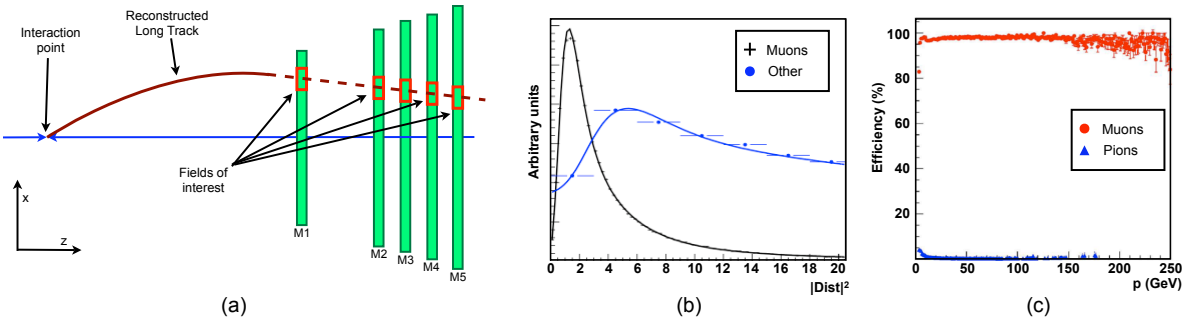

Figure 3.20: (a) Schematic diagram illustrating offline muon identification. (b) The squared distance between extrapolated tracks and hits inside the fields of interest for muons and non-muon sources (from[47]). (c) The efficiency for muon identification and rate of pion mis-identification as a function of momentum in the offline reconstruction.

Offline muon identification

As shown in figure 3.20(a), muon identification in the HLT and in the offline reconstruction is performed by first extrapolating long tracks with momenta above 3GeV to the muon system. Detector hits are then searched for in fields of interest (FOI) around the track. The size of the FOI are determined by a parameterised function of both the momentum of the track and the detector region. Tracks are considered as muon candidates if a minimum number of stations are found to have hits within the FOI. The number of required stations with associated hits depends on the momentum, p, of the track: for 3GeV/c<p<6GeV/c there must be associated hits in M2 and M3; if 6GeV/c<p<10GeV/c there must be associated hits in M2, M3 and either a hit in M4 or M5; if p>10GeV/c there must be associated hits in M2, M3, M4 and M5. As can be seen in figure 3.20(b), by comparing the average track-hit separation distance for all hits in the FOIs associated to the track, further improvements to the muon identification can be obtained. Figure 3.20(c) show the expected muon identification performance in the HLT and the offline reconstruction. For muons with momenta below 150GeV/c, an efficiency of $\sim$98% is expected with an associated pion mis-identification rate of $\sim$1%.

The issue of muon identification and hadron mis-identification will be dealt with in greater detail in chapter 4.

3.2.7 The trigger system

The trigger system at LHCb[48] will filter the proton-proton events before they are stored to disk. This is necessary for two reasons. Firstly, the frequency of visible interactions at LHCb ($\sim$10MHz) will be too high for all of the events to be written to disk. One fully reconstructed LHCb event will occupy 100kB of storage space, thus if every visible event was reconstructed and recorded to disk LHCb would require $\sim 10^7$TB of disk space per year to store these events. Even considering the massive computing resources required to reconstruct and analyse these

events, recording every event at LHCb is clearly impossible. Secondly, only a small fraction of these events are of interest to the LHCb physics programme. For example, since the $b\bar{b}$ production cross section at the LHC will be about 200 times smaller than the inelastic cross section and the inclusive branching ratio to b hadron decay channels of phenomenological interest is $O(10^{-3} - 10^{-5})$, the events of interest to the LHCb b physics programme only occur with a frequency of a few tens of Hz.

Since there is insufficient time available for full event reconstruction in the trigger system, events are filtered by successive stages. At the initial stage a fast selection is performed by applying loose cuts to a small set of simple variables. This allows for the fast rejection of a large portion of the background events while maintaining a high efficiency for the signal events. Due to the increasingly lower input rate, more time is available during the later trigger stages allowing for more advanced reconstruction and selection routines to be performed. The LHCb trigger system will reduce the visible event rate of $\sim$10MHz to the more manageable rate of $\sim$2kHz which will be stored to disk.

When the physics studies presented in this thesis were being conducted, the LHCb trigger system had three levels: a hardware trigger known as Level 0 (L0) and two trigger levels implemented in software, Level 1 (L1) and the High Level Trigger (HLT). Due to subsequent advances in computing power and networking technology[12], L1 and HLT have recently been merged[50]. While this has resulted in improvements to the trigger performance for a number of channels, particularly those having all hadronic final states, the impact on final states containing dimuons is expected to be minimal. L0, L1 and the HLT will be described in more detail in the following sections.

Level-0 (hardware)

The Level-0 trigger, which has an effective input rate of 10MHz and an output rate of 1MHz, is performed by dedicated electronics on the calorimeter, muon and pile-up systems. The electromagnetic and hadronic calorimeters provide: the largest transverse energy found for a number of different cluster types, electrons, photons, charged hadrons and neutral pions; and the total transverse energy in the event. The muon system provides the two highest transverse momentum muon candidates from each quadrant in the muon system, giving a maximum of eight candidates in total. Finally, the SPD detector provides the charged track multiplicity while the pile-up system provides the number of primary vertices in the event. The L0-trigger decision is taken after a fixed latency of 4μs, meaning that the front-end electronics must store 160 events in memory while the decision is pending.

There are two logical conditions that must both be met for an event to pass L0. They are:

[12]Due to advances in network switch technology, it is now possible to transfer the full detector readout from the front end electronics to the computing farm at the L0 accept rate of 1MHz. This has effectively eliminated the need for the Level 1 trigger as a distinct entity. The trigger system now has two stages L0 and HLT. While L0 has remained unchanged, some elements of L1 have been incorporated into the HLT while other features have been removed entirely.

1. Global requirements: Events are rejected on the basis of four global event variables. Since multiple interaction events could potentially consume a large proportion of the bandwidth and are not useful for many of the $\mathcal{CP}$ violation measurements, it is important that these events are not recorded to disk. This is achieved by using information from the pile-up detector and the SPD. An event is rejected if: the pile-up detector finds two or more vertices that are the origin of at least three tracks; for events where less than two muons are found, the pile-up multiplicity is larger than 112 or the SPD multiplicity is greater than 280. In order to guard against particles from the beam halo consuming a large portion of the bandwidth, an event is rejected if the total transverse energy from the calorimeters is less than 5GeV.

2. High P_T trigger: A distinguishing characteristic of b events compared to other proton-proton interactions is the presence of high P_T tracks. The L0 decision unit is sent the highest E_T electron, photon and hadron clusters from the calorimeters and the two highest P_T muons found by the muon system. One of these candidates must pass the respective cut on P_T or E_T given in table 3.4 in order for the event to pass L0. It should be noted that the transverse momentum requirement for a dimuon is applied to sum of the P_T's of the two muons, meaning that individually these muons can both have transverse momenta below the single muon threshold of 1.1GeV.

Particle Type	Hadron	Electron	Photon	π^0	Muon	dimuon ΣP_T^μ
Threshold	3.6	2.8	2.6	4.5	1.1	1.5

Table 3.4: L0 transverse energy and transverse momentum thresholds. The units are GeV for hadrons, electrons and photons and GeV/c for muons. The results of these cuts are logically ORed.

If an event is passed by L0, all of the data in the remaining detectors are digitised and buffered and a portion of it is passed to the computing farm where the L1 algorithms are run.

Level-1 (software)

L1 has an input rate of 1MHz and an output rate of 40kHz. In addition to the information from L0 decision unit, it uses the information from the VELO and TT detectors. It consists of a sequence of algorithms, implemented in software, that are executed on the nodes of a large computing farm. Since events containing b hadrons often contain tracks that have large impact parameters (due to the characteristic secondary vertices) and high transverse momenta, the strategy of the L1 trigger is to look for tracks with these features.

L1 commences by looking for tracks with large impact parameters. This is achieved in the following way. 2D VELO tracks are reconstructed in the r-z projection and used to evaluate the z position of the primary vertex. If more than one primary vertex is found the event is rejected. The impact parameter (IP) of these tracks in the r-z plane is then determined. Tracks that have IP$>150\mu$m or are matched to L0 muons are then reconstructed in 3D by adding the information from the VELO ϕ sensors.

There are two ways that the momenta of these 3D VELO tracks can be determined. Firstly, an attempt is made to match the tracks to L0 objects. This is achieved using the ϕ and dr/dz information from the tracks and L0 objects. A successful match provides a momentum estimate with an uncertainty of 6% for muons, 12% for electrons and 15% for hadrons. Secondly, since the magnetic field between the VELO and the TT is non-zero, by matching the 3D VELO tracks to clusters in the TT their momenta can be determined with an uncertainty of $\sim$20%. This second method is useful since the reconstruction efficiency for L0 hadrons and electrons is relatively low.

The 3D tracks are then used to determine if the event should be vetoed. Events will pass the L1 trigger if at least one of the following requirements is satisfied. Firstly, events containing a dimuon will pass if the dimuon invariant mass is above 2.6GeV/c^2 or if the invariant mass is above 0.5GeV/c^2 and the combined dimuon impact parameter is larger than 75μm. Secondly, if the event contains a photon or electron with a transverse energy above 3GeV the event is passed. Finally, an event is accepted if it passes a simultaneous cut applied to the transverse momenta and impact parameter significance of the two highest P_T tracks in the event.

If an event passes the L1 trigger the full digitised event is passed from the buffers in the readout electronics to the computing farm and the HLT algorithms are executed.

The High Level Trigger (software)

The HLT has access to all of the detector data and consists of a sequence of software algorithms that, like the L1 trigger, will be run on the nodes of the computing farm. It has an input rate of 40kHz and a nominal output rate of 2kHz - an output rate that can be adjusted depending on the computing resources that are available.

The first task of the HLT is to rerun the L1 algorithms using the information from the tracking stations T1-T3. This provides a momentum measurement with an uncertainty of $\sim$0.5% - an improvement that reduces the level of background by a factor of two while only reducing the signal efficiency by a few percent.

The remaining events are then fully reconstructed using tracking and particle identification algorithms that are similar to those used offline. Events that pass a set of inclusive and exclusive selections are then fully reconstructed and written to disk. Of significance for the physics studies outlined in chapters 4 and 5, it should be noted that all events found at this stage that contain a dimuon with a mass above 2.6GeV/c^2 will pass the HLT and will subsequently be written to disk.

3.2.8 Software

The LHCb software[51] is implemented in an object oriented framework called Gaudi. Gaudi is written in C++ and provides a number of services that allow sharing of basic functionality such as job steering, message logging, data access and data analysis. The applications

contained within Gaudi are composed of algorithms which exploit these services. All of the physics results that will be presented in the subsequent chapters of this thesis were obtained with the simulation, reconstruction and analysis software contained within this framework. This software can be logically divided into three parts: the first part contains two packages, called *Gauss*[52] and *Boole*[53], that simulate the proton-proton collisions that will occur at the LHC, model the detector response and digitise the resulting data so that it has the same form as the data that will be produced by LHCb when it is operational; the second part, which is performed by a package called *Brunel*[54], reconstructs physics objects using either the simulated data from Gauss and Boole or real data from LHCb; finally, the analysis of these reconstructed physics objects is achieved using the *DaVinci*[55] package. Each element of this chain will be described in turn.

Event generation: The event generation step simulates the proton-proton collisions that will occur at the LHC, i.e. it provides a description of the position and momentum four-vectors of all of the particles that are produced in a given collision. This step is delegated to an external generator that is steered by the Gaudi application known as Gauss. Currently the default generator that is used in the LHCb simulation is a version of PYTHIA 6.324[29] that has been tuned to reflect the conditions at LHCb and which uses the CTEQ5L set of parton distribution functions[27]. However, as will be described in chapter 5, it is also possible to interface other event generators with the LHCb simulation software. The decay of B hadrons is handled by another external package called EvtGen[56].

Detector simulation: The simulation of how the particles proceed through the detector is performed using the Geant4 toolkit[57] which is also controlled by Gauss. Geant4 simulates the impact of the magnetic field and the interactions with the detector material, e.g. multiple scattering, energy loss, photon conversions and further decays of unstable particles. It is capable of fully simulating the interactions of hadrons with momenta greater than 10MeV/c and leptons and photons with momenta greater than 1MeV/c. In order for this simulation to be accurate a full description of the LHCb detector is needed. The description used by Geant4 fully describes the active detector elements and other passive elements such as the support structures, shielding elements and the beam-pipe. The effects of the magnetic field are simulated using a field map based on measurments made after the magnet was installed. Each interaction of a particle with an active detector element is stored in as a hit-object containing the position and type of interaction.

Digitisation: The response of the detector electronics and the L0 trigger hardware is simulated by the Boole application. The response of each sub-detector to the hit-objects is described by a set of algorithms that have been tuned using test-beam data. The output from this stage has the same form as real data coming from the detector.

Reconstruction: The reconstruction of the digitised events, coming from either the detector or Boole, is performed by the Brunel package. Brunel includes various algorithms that associate hits from the sub-detectors, forms tracks and identifies the particles using the information from the calorimeters, the RICH detectors and the muon system.

Analysis: The event selection algorithms are executed using the DaVinci application. This process begins with the construction of particles and vertices from tracks and particle iden-

tification objects. The final state of interest can then be selected by making the appropriate particle combinations. Finally, Davinci provides the functionality for developing and applying offline selection algorithms that can be used to select physics processes of interest and reject background processes.

4 Measuring $\sigma_Z \cdot Br(Z \rightarrow \mu^+\mu^-)$ at LHCb

This chapter presents the trigger, reconstruction and selection efficiencies for recording $Z \rightarrow \mu^+\mu^-$ events at the LHCb experiment. These events can be used to make luminosity measurements, improve our understanding of the internal structure of the proton and test the Standard Model in a new energy regime.

4.1 Introduction

A measurement of the production cross-section of Z bosons in proton-proton collisions at LHC energies will provide an important test of the electroweak part of the Standard Model. A measurement of this cross-section via the decay channel $Z \rightarrow \mu^+\mu^-$, which provides a final state that is both clean and fully reconstructable, will enable a precise measurement of the differential cross-section distributions with respect to both the Z boson rapidity, $d\sigma/dy$, and the Z boson transverse momentum, $d\sigma/dP_T$. Since the longitudinal component of the Z momentum will directly depend on the proton parton distribution functions (PDFs), a measurement of the shape and overall normalisation of the $d\sigma/dy$ distribution will improve our knowledge of the PDFs. This will result in improvements to theoretical predictions that will have an impact on much of the physics at the LHC. In addition the low P_T region ($P_T \sim 1$GeV/c) of the $d\sigma/dP_T$ distribution, being sensitive to non-perturbative corrections that are related to the resummation of initial parton emissions, will provide an important constraint on QCD while the high P_T ($P_T \gg 1$GeV/c) region will be sensitive to physics beyond the Standard Model. LHCb will be able to measure the total and differential Z cross-section via this channel for events in the rapidity range $1.7 \leq y \leq 4.9$. This will provide a cross-check for the corresponding measurements at the CMS and ATLAS experiments, both of which will have a coverage of $|y| \leq 2.5$, while at the same time providing unique measurements at high Z rapidities.

Experimentally, for a given data set the cross-section within some fiducial volume v can be calculated from

$$\sigma_Z(v) \cdot Br(Z \rightarrow \mu^+\mu^-) = \frac{N_Z^{obs} - N_Z^{back}}{\varepsilon_Z^{total} \cdot \int \mathcal{L} dt} \tag{4.1}$$

where N_Z^{obs} is the number of observed $Z \rightarrow \mu^+\mu^-$ candidates, N_Z^{back} is the expected number of background events, ε_Z^{total} is the overall efficiency for recording $Z \rightarrow \mu^+\mu^-$ events and $\int \mathcal{L} dt$ is the integrated luminosity for the data sample. The overall efficiency can be expressed as the

product

$$\varepsilon_Z^{total} = A_Z^{geom\,(v)} \times A_Z^{kin} \times \varepsilon_Z^{trigger} \times \varepsilon_Z^{reco} \tag{4.2}$$

where $A_Z^{geom\,(v)}$ and A_Z^{kin} are the acceptances due to the detector topology and offline kinematic selection criteria respectively, while $\varepsilon_Z^{trigger}$ and ε_Z^{reco} are the trigger and reconstruction efficiencies. This chapter presents Monte-Carlo based estimates of the acceptances, efficiencies and level of background for the $Z \to \mu^+\mu^-$ channel at LHCb. These results are used to estimate the precision of a cross-section measurement within two fiducial volumes: the volume equivalent to the LHCb acceptance ($1.7 \leq y \leq 4.9$), from now on referred to as a *forward measurement*, and the full 4π volume i.e. a total cross-section measurement. Luminosity measurements at LHCb are discussed elsewhere (see[58, 59, 60] and chapter 5 of this thesis) and it is expected that measurements of $\int \mathcal{L}dt$ can be achieved with an uncertainty of $\sim$1-2%.

Previous work by members of the Roma LHCb group has shown that $Z \to \mu^+\mu^-$ events can be recorded and reconstructed at LHCb and used to determine the absolute luminosity[61]. In addition, the sensitivity of $\sigma_Z \cdot Br(Z \to \mu^+\mu^-)$ to different PDF sets was explored in[62]. A new single muon trigger stream was introduced in[63] which increased the level 1 trigger efficiency for $Z \to \mu^+\mu^-$ to 87% and the backgrounds to the selection coming from $b\bar{b}$ and minimum bias events were studied. In this chapter we consider changes to the level 1 dimuon trigger which improve the efficiency for $Z \to \mu^+\mu^-$ selection. More sources of background and in particular the dominant source due to π/K mis-identification is studied. An estimate is made of the systematic uncertainties that can be expected on a measurement of $\sigma_Z \cdot Br(Z \to \mu^+\mu^-)$, due to both experimental error and theoretical uncertainties in the next to leading order prediction and the PDFs. Finally, the capability to constrain the proton PDFs provided by a Z cross-section measurement at LHCb is explored.

The chapter is organised as follows. Section 4.2 provides some theoretical context. The event characteristics and experimental efficiency of $Z \to \mu^+\mu^-$ events at LHCb are given in section 4.3. Section 4.4 describes the various background processes. In section 4.5 a set of offline selection cuts are proposed and their effects on both the signal and background events are described. Systematic uncertainties on the efficiency and purity are discussed in section 4.6 while the overall expected measurement accuracy is detailed in section 4.7. Finally, in section 4.8 the potential to constrain the proton PDFs using this channel is discussed.

4.2 Theoretical context

As discussed in chapter 2, Z boson production at hadron colliders proceeds via the Drell-Yan process[24]. At leading order this consists of the annihilation of a quark and an anti-quark of the same flavour as shown in figure 4.1(a). At the LHC Z production will occur from either $\bar{u}u$ or $d\bar{d}$ with about 15% due to $s\bar{s}$. Since the colliding hadrons at the LHC will be protons this process must occur through collisions between valance quarks and sea anti-quarks or sea quarks and sea anti-quarks. As shown in chapter 2, the leading order (LO) partonic cross-

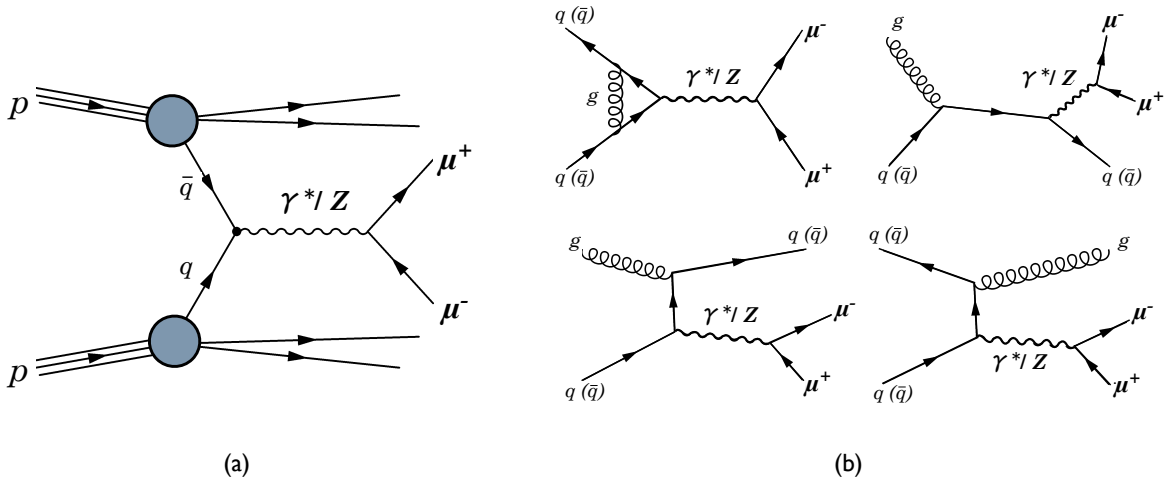

Figure 4.1: Feyman diagram showing: (a) Drell-Yan pair production at leading order, (b) the main higher order contributions to the Z production cross section.

section for this process is[64]

$$\hat{\sigma}_{q\bar{q}\to Z} = \frac{\pi}{3}\sqrt{2}G_F M_Z^2(g_V^2 - g_A^2)\delta(\hat{s} - M_Z^2) \tag{4.3}$$

Here G_F is the Fermi constant, M_Z is the mass of the Z boson and g_V and g_A are the vector and axial couplings respectively. Employing the Factorisation theorem the hadronic level cross-section can be expressed as the convolution of this partonic cross-section and a parameterisation of the proton's substructure

$$\sigma_{pp\to Z} = \int dx_1 dx_2 \hat{\sigma}_{q\bar{q}\to Z} \sum_q [f_{q/p_1}(x_1, Q^2) f_{\bar{q}/p_2}(x_2, Q^2) + (q \leftrightarrow \bar{q})] \tag{4.4}$$

where Q^2 defines the scale at which the process occurs, which in the case of Z production equals M_Z^2. Here $x_{1,2}$ is the momentum fraction of the incident proton carried by the colliding parton, either a quark or anti-quark, where the subscript signifies whether the parton is in the first or second proton. The fractional momenta carried by the interacting partons are related to the rapidity of the resulting Z boson in the following way: $x_{1,2} = M_Z e^{\pm y}/\sqrt{s}$, where $\sqrt{s}$ =14TeV. $f_{q/p_1}(x_1, Q^2)$ is the probability that proton p_1 contains a quark with a fraction x_1 of the proton's momentum and $f_{\bar{q}/p_2}(x_2, Q^2)$ is the probability that the proton p_2 contains an anti-quark with a fraction x_2 of the proton's momentum. As discussed in chapter 2, these probabilities are given by so-called parton distribution functions (PDFs) that describe the fraction of the incoming proton's momentum, x, carried by each type of parton as a function of the square of the momentum exchanged in the hard scatter, Q^2.

The higher order corrections to this cross section are substantial and are mainly due to quark-gluon interactions (see figure 4.1(b)). Figure 4.2 shows the predicted Z production cross section times leptonic branching ratio, for both the Tevatron and LHC, at leading order, next

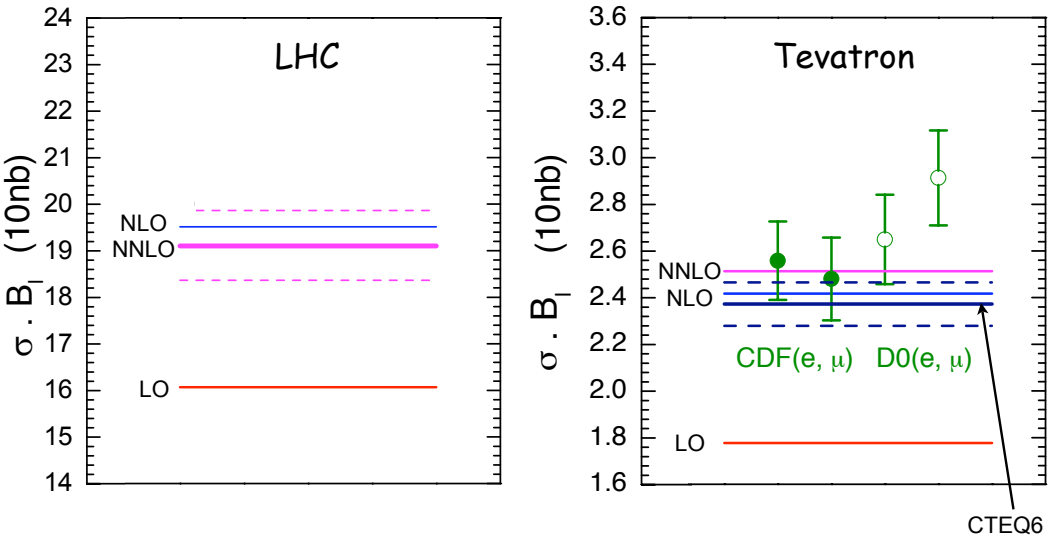

Figure 4.2: The predicted Z production cross section times leptonic branching ratio, in units of $10 \times nb$, at leading order (LO), next to leading order (NLO) and next to next to leading order (NNLO) for the LHC (left) and Tevatron (right) using the MRST 2004 PDF set. The CTEQ6 NLO prediction is also shown for the Tevatron results. (from[65]).

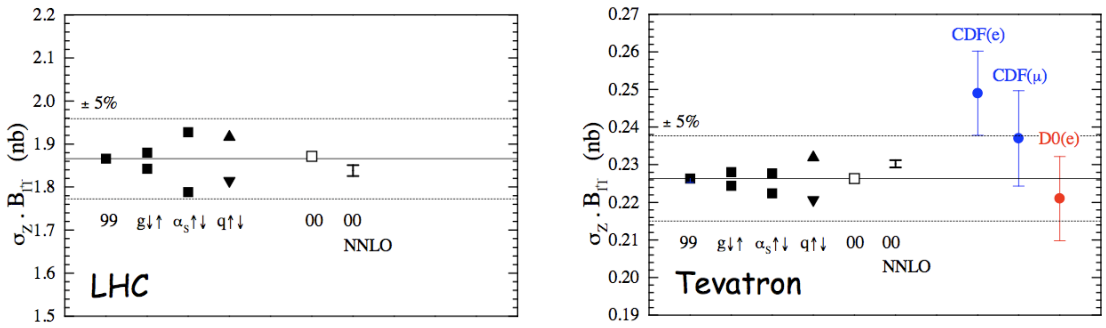

Figure 4.3: NNLO Z production cross section times leptonic branching ratio predictions for various PDF sets from MRST99 and MRST00. The measured Tevatron values (CDF and D0) are shown and are in good agreement with theory (from[65]).

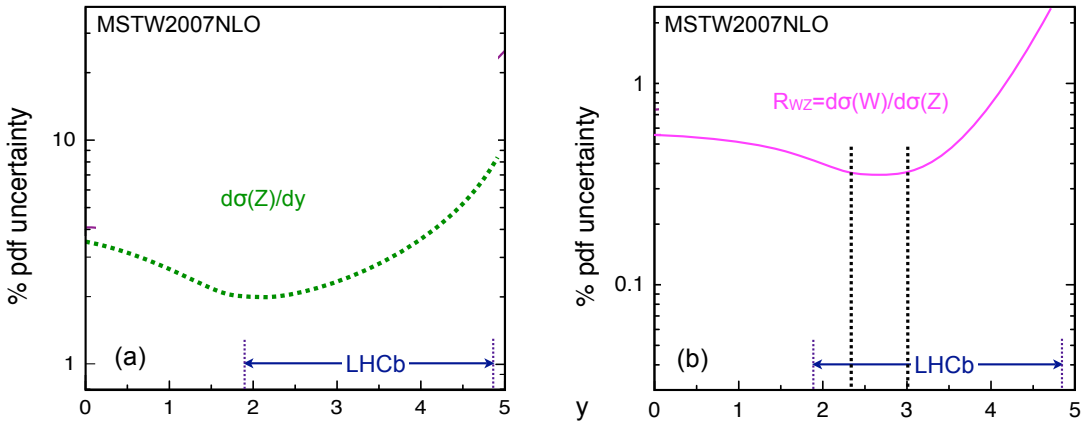

Figure 4.4: Percentage PDF uncertainties predicted by the MSTW2007 PDF set as a function of rapidity for: (a) the Z production cross-section and (b) the ratio $R_{WZ} = \sigma_W/\sigma_Z$. The PDF uncertainty on R_{WZ} reaches a minimum value of $\sim$0.4% in the highlighted rapidity range $2.25 < y < 3$ which lies within the LHCb acceptance. (From[69]).

to leading order (NLO) and next to next to leading order (NNLO). It should be noted that while the NLO correction is large, the NNLO correction[28] is small giving us confidence that the theoretical prediction will converge to a value near the NNLO value. The main contribution to the uncertainty on this predicted cross-section arises from the uncertainties associated with the proton PDFs. The current NNLO theoretical predictions for the $Z \to l^+l^-$ cross section for $p\bar{p}$ collisions at $\sqrt{s}$ =1.96TeV are in good agreement with the experimental values measured by the Tevatron experiments, CDF and D0, which have an associated measurement uncertainty of 6%[66, 67] (see figure 4.3). These predictions use parton distributions, evolved from measurements made at HERA and fixed target experiments, which are sensitive to different values of x than will be probed at the LHC. The percentage PDF uncertainty, as predicted by the MSTW2007 PDF set, on the Z production cross-section as a function of rapidity is shown in 4.4(a).

The parts of (x, Q^2) space that will be accessible to LHCb are shown in figure 4.5(a). Since LHCb is only instrumented in the forward region (1.9< y <4.9), only hard scattering subsystems with high rapidities can be reconstructed. Given the fact that these high rapidities only occur when the momenta carried by the interacting partons are highly asymmetric, the reconstruction of these events will probe two distinct regions of (x, Q^2) space. The production mechanism for Z bosons that will be reconstructed at the central LHC detectors will differ from those that will be reconstructed at LHCb. For Z bosons that can be reconstructed at ATLAS and CMS $x_1 \approx x_2 \approx 0.005$ and the Z will be predominantly produced in a collision involving a sea quark and sea anti-quark. At LHCb $x_1 \gg x_2$ and the collision will be between a valance quark and a sea anti-quark. For LHCb, as shown in figure 4.5(b), PDFs for most x_1 values have been determined from fixed target data and to a lesser extent HERA data and confirmed at higher Q^2 by W/Z production at the Tevatron. In the x_2 range, the PDFs have been measured by HERA alone but at much lower Q^2 values from where they must be evolved to W/Z energies using the DGLAP[25] equations. Figure 4.3 shows the NNLO cross section predictions for various PDF sets from MRST99 and MRST00 and indicates that the associated

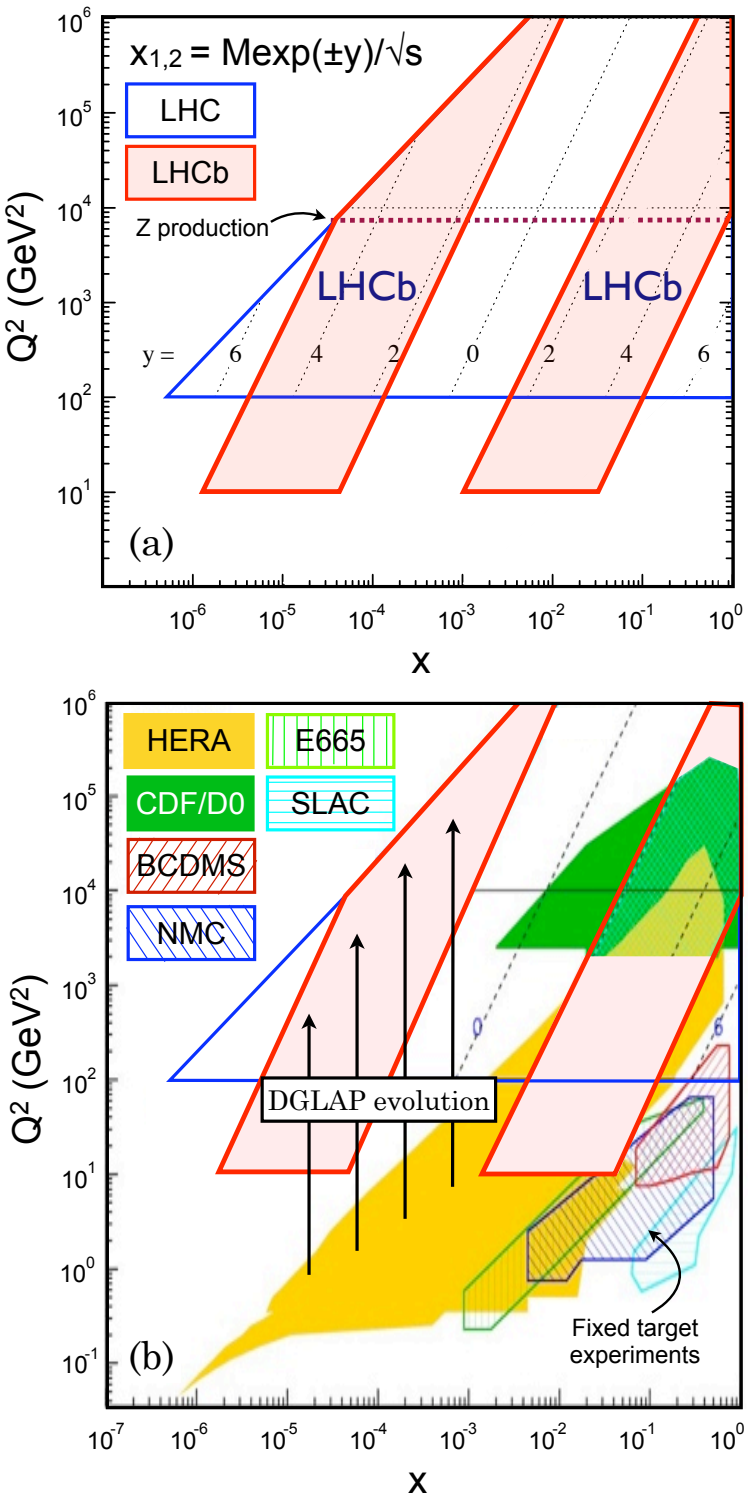

Figure 4.5: Plots of Q^2 versus x for the production of a particle of mass M. (a) Shows the regions accessible via Z events at LHCb. The Q^2 value at which Z production occurs is highlighted. (b) Shows the regions that have been accessed at a variety of other experiments. Predictions at LHCb are based primarily upon data from fixed target experiments and the Tevatron for high x values, while at low x predictions are dependent on the DGLAP evolution of HERA data.

uncertainty on the predicted cross-section due to PDF uncertainties is $\sim$4% (see[68]). Thus a measurement of the Z production cross section at LHCb with an experimental uncertainty $<$4% will allow us to constrain the PDF sets down to $x_2 = 4.84 \times 10^{-5}$ and up to x_1 =0.873. In addition it has been recently shown by the MSTW group that deviations in the normalisation or differential cross-section shape above 5% with respect to current predictions cannot be accomodated within PDF fits[69]. Thus any measured deviations from these predictions at this level would be an indication of either new physics or an inconsistency within QCD.

If the W cross-section is also measured the ratio of the two cross-sections, σ_W/σ_Z, can be determined. As shown in fig. 4.4(b) the latest set of predictions by the MSTW group suggest that the percentage uncertainty on this ratio due to PDF uncertainties will reach a minimum value ($\sim$0.4%) in the rapidity region 2.25$< y <$3 which lies within the LHCb acceptance. Since many of the theoretical and experimental uncertainties will cancel in this ratio, LHCb will be in a position to make a precise test of the Standard Model at the LHC.

4.3 Signal events

A Monte Carlo sample of 99500 $pp \to Z \to \mu^+\mu^-$ events was used in this analysis. These events were generated with PYTHIA 6.324[29] using the CTEQ5L[27] set of PDFs and the detector effects were simulated using the detector geometry described by Dbase v22r4 and Gauss v15r21. The detector digitization was performed by Boole v6r5 and event reconstruction by Brunel v24r5. The full Z/γ^* interference structure has not been simulated. Only the contribution from on-shell Z bosons has been considered. To speed up the generation process the generated events were required to contain a muon from the decaying Z boson that has a direction of flight that lies within 400mrad of the beam axis and a transverse momentum greater than 4GeV/c. Figure 4.6(b) shows the Z boson rapidity distribution at the LHC, as predicted by PYTHIA 6.324 and the CTEQ5L PDF set, and highlights the subsets corresponding to events that pass this generator cut and events that can be triggered and reconstructed at LHCb. The analysis of these events has been performed using the LHCb analysis package DaVinci v12r14.

4.3.1 Signal event characteristics

Since the Z boson has a very large mass of $\sim$91GeV/c^2 and a decay length of $\sim$0.1fm our signal events will have a simple and distinctive topology. Typically we should reconstruct two high transverse momentum, P_T ($\sim$45GeV/c), muons of opposite charge and low impact parameter significance, IPS[1], which together have an invariant mass near the Z mass. The event topology of such an event at LHCb is shown in figure 4.6(a). Figures 4.7 and 4.8 show the invariant mass, transverse momentum and impact parameter significance distributions of the muons in our signal events that pass the L0, L1 and HLT triggers and are then reconstructed.

[1]Defined to be the muon impact parameter divided by its uncertainty.

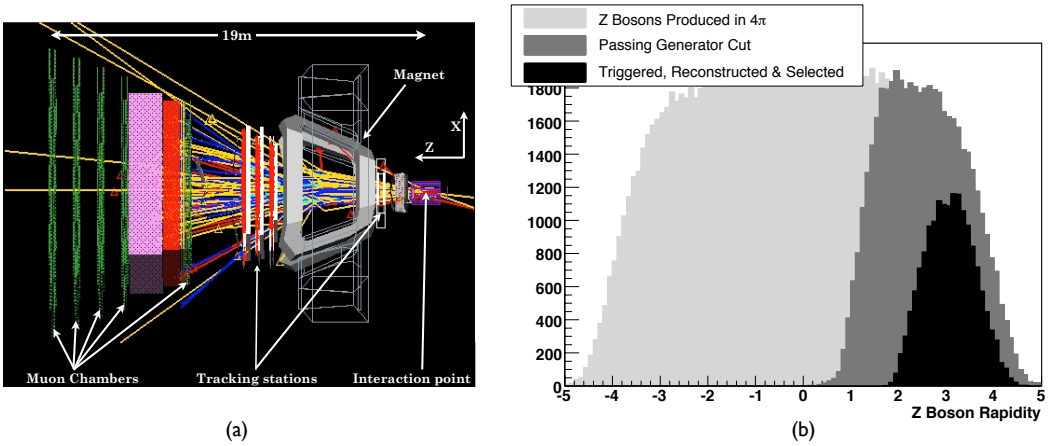

Figure 4.6: (a) Graphic produced using Panoramix, the LHCb event visualisation programme, showing an event containing a Z boson decaying to a $\mu^+\mu^-$ pair. The two muons coming from the Z decay at the interaction point can be clearly seen to pass through the five muon chambers. (b) Z boson rapidity distributions at the LHC predicted by PYTHIA 6.324 and the CTEQ5L PDF set. The subsets corresponding to events that pass the generator cuts outlined in section 3 and events that are triggered, reconstructed and selected at LHCb are highlighted.

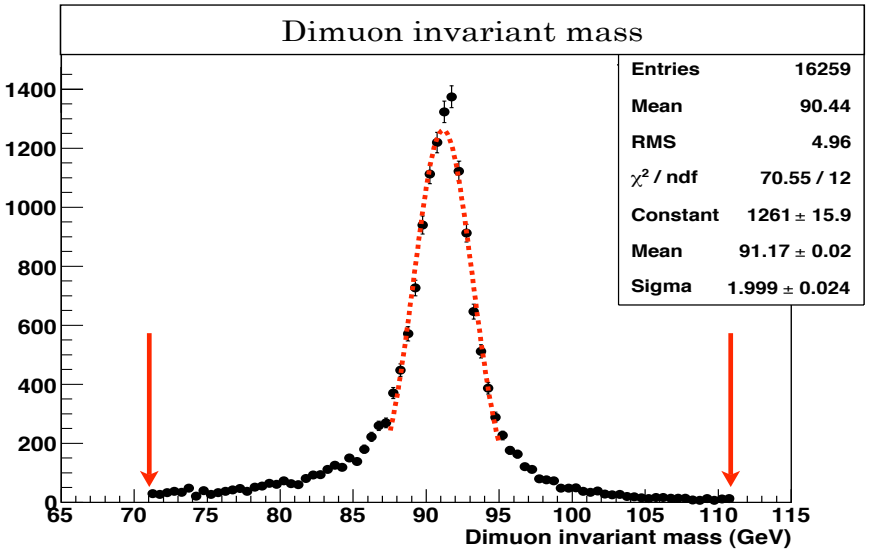

Figure 4.7: Invariant mass distribution of the $\mu^+\mu^-$ pair from *on mass shell* Z bosons. A gaussian has been fitted to the events in the mass range 87.5GeV/c^2 < $M_{\mu\mu}$ <95GeV/c^2 yielding a fitted Z boson mass of (91.17 ± 0.02)GeV/c^2. The proposed mass window cut discussed in section 5 is highlighted by the two arrows.

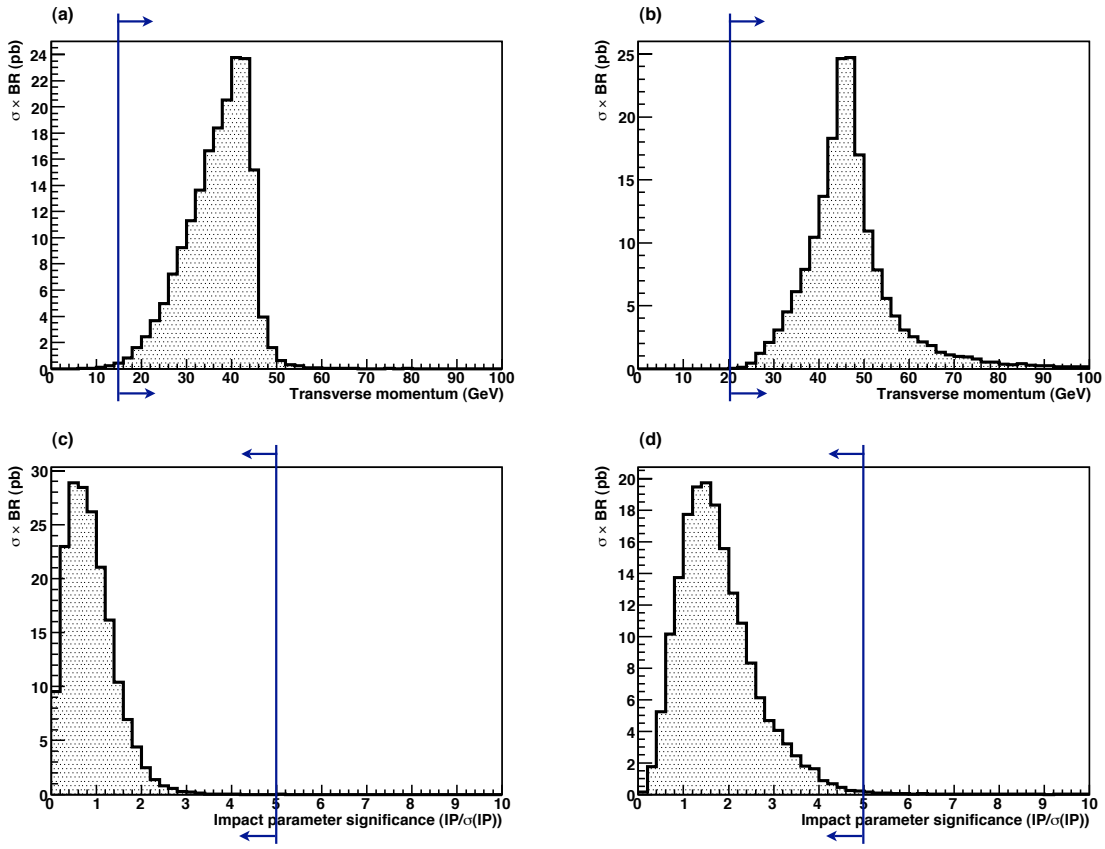

Figure 4.8: $Z \to \mu^+\mu^-$ event characterisics: (a) Transverse momentum (P_T) distribution for muon with lower P_T, (b) Transverse momentum (P_T) distribution for muon with higher P_T, (c) Muon impact parameter significance (IPS) distribution for muon with lower IPS and (d) Muon impact parameter significance distribution for muon with higher IPS. The offline kinematic cuts described in section 5 are highlighted.

4.3.2 Geometric acceptance

The geometric acceptance has been calculated for a Z cross-section measurement within two different fiducial volumes. Firstly for a measurement where the Z boson rapidity lies inside the range $1.7 < y < 4.9$, which we refer to as a *forward measurement*, and secondly for an extrapolation to a measurement of the total (4π) cross-section.

Since the geometric acceptance within these volumes will depend on the shape of the $d\sigma/dy$ distribution, a shape that varies depending on both the order at which the calculation is made and the order of the PDF set used, two separate geometric acceptance calculations for each fiducial volume have been made. The first calculation is based on the $d\sigma/dy$ distribution predicted by a NLO calculation obtained using the MCFM Monte-Carlo generator[70] and the MRST2001nlo[71] NLO PDF set, while the second is based on the distribution predicted by PYTHIA 6.324 using the the CTEQ5L LO PDF set. The predicted rapidity distributions,

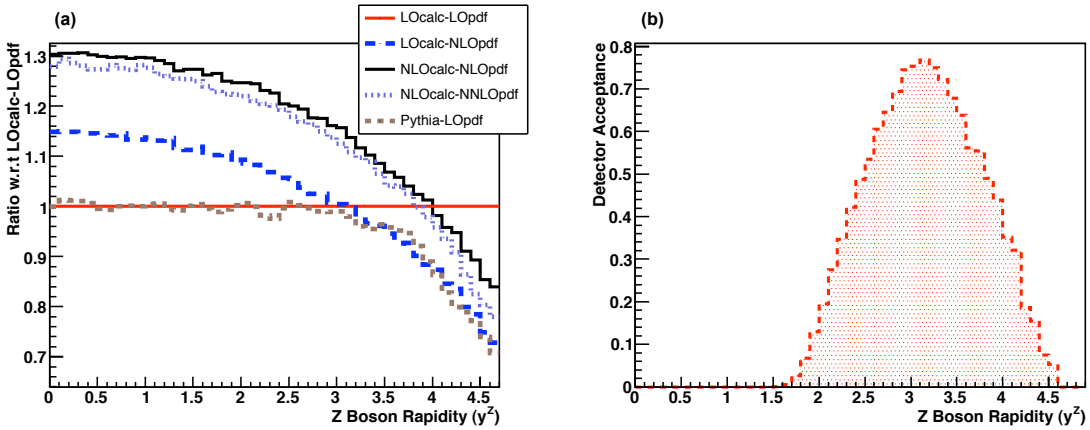

Figure 4.9: (a) Normalised $d\sigma/dy$ distributions predicted by a number of different order calculations and different order PDF sets. Aside from the PYTHIA distribution the predictions are due the MCFM generator. Each distribution has been normalised by dividing by the leading order (LO) prediction of the MCFM generator using the MRST2001lo LO PDF set. The NLO predictions of MCFM were found using the MRST2001nlo (NLOpdf) and MRST2001nnlo (NNLOpdf) PDF sets while the PYTHIA prediction was obtained with the CTEQ5L LO PDF set. (b) the detector acceptance of $Z \to \mu^+\mu^-$ events at LHCb as a function of Z boson rapidity.

which have been normalised by dividing by the LO MCFM prediction using the MRST 2001 LO PDF set[71], are shown in figure 4.9(a).

The geometric acceptance for each fiducial volume was calculated twice by multiplying the predicted NLO or PYTHIA rapidity distribution by the detector acceptance. The detector acceptance, which was determined using the sample of fully simulated events, has been defined to be the fraction of events in a given rapidity bin that, at Monte-Carlo truth level, contained a μ^+ and a μ^- from a decaying Z boson that were both *reconstructible* as long tracks. Here we have followed the standard LHCb definition of *reconstructible*, i.e. a reconstructible long track is one that, at Monte-Carlo truth level, has 3 radial and 3 ϕ VELO clusters and one x cluster and one stereo cluster in each of the three T stations[2]. The detector acceptance is shown as a function of Z boson rapidity in figure 4.9(b).

The calculated geometric acceptances for each fiducial volume are summarised in table 4.1. The NLO values for a cross-section measurement within $1.7 < y < 4.9$ and for an extrapolation to a total (4π) measurement were found to be, respectively, 0.4657 ± 0.0019 and 0.1224 ± 0.0021. These values correspond to $\sim 1.5\%$ and $\sim 5\%$ reductions on the values calculated using the PYTHIA distribution. Since, as was noted in section 4.2, the perturbation series in a calculation of the Z cross-section at the LHC is found to converge quickly we assume the calculated NLO values are more accurate than the LO values predicted by PYTHIA. The NLO values are therefore used throughout the rest of this chapter. In practice the acceptance for a measurement within the region that is instrumented at LHCb - i.e. a forward measurement - will be taken into account by making a bin by bin correction of the

[2] In other words, in each T station there must be at least one cluster in a layer with vertical (x) readout strips and one cluster in a layer with readot strips that are rotated by $\pm 5^\circ$ (stereo).

Calculation	Measurement within $1.7 < y < 4.9$	4π measurement
PYTHIA 6.324 and CTEQ5L	0.4724 ± 0.0019	0.1288 ± 0.0021
MCFM NLO and MRST2001nlo	0.4657 ± 0.0019	0.1224 ± 0.0021

Table 4.1: The calculated geometric acceptance values for a cross-section measurement within $1.7 < y < 4.9$ and for an extrapolation to a total (4π) measurement. The values have been determined using the Z boson rapidity distributions predicted by both a NLO calculation (MCFM and MRST2001nlo) and LO calculation (PYTHIA 6.324 and CTEQ5L). Statistical errors are shown.

reconstructed $d\sigma/dy$ distribution using the distribution shown in figure 4.9(b). The overall acceptance value for a forward measurement presented here, therefore, should be viewed as an indicative value.

It should be noted that MCFM does not include any parton showering. Parton showering, as was discussed in chapter 2, is used to approximate the effects of the higher order terms not included in a given perturbative calculation. The effects of parton showering are clearly visible in figure 4.9(a) - the leading order Pythia calculation, which includes parton showering, produces a Z rapidity distribution that is markedly different from the leading order MCFM calculation. In the future, therefore, these acceptance calculations should be repeated using an NLO calculation that includes parton showering.

4.3.3 Reconstruction and trigger efficiencies

The reconstruction efficiency, ε_Z^{reco}, and trigger efficiency, $\varepsilon_Z^{trigger}$, will be determined from data once it arrives. However, this section presents estimates of these efficiencies that were obtained using the full LHCb detector simulation.

The reconstruction efficiency, ε_Z^{reco}, is defined to be the fraction of events within the LHCb geometric acceptance that can be reconstructed offline. It can be expressed as the product of three components:

$$\varepsilon_Z^{reco} = (\varepsilon_{trk}^{(1)} \times \varepsilon_{match}^{(1)} \times \varepsilon_{id}^{(1)}) \times (\varepsilon_{trk}^{(2)} \times \varepsilon_{match}^{(2)} \times \varepsilon_{id}^{(2)}) \tag{4.5}$$

Here ε_{trk} is the efficiency of reconstructing the track of one of the muons coming from the Z boson decay. ε_{match} accounts for the efficiency of reconstructing the required number of hits in the muon chambers (see section 3.2.7) and matching them to this track. Finally, for tracks that have been matched to the required number of muon hits, ε_{id} is the efficiency of any additional muon identification criteria, e.g. calorimeter energy requirements, that will be used to increase the purity of the muon samples. The superscripts refer to muon 1 or muon 2. Possible methods for determining ε_{trk}, ε_{match} and ε_{id} from data and the expected

Stage	Symbol	Measurement within $1.7 < y < 4.9$	4π measurement
Detector acceptance	A_Z^{geom}	0.4657 ± 0.0019	0.1224 ± 0.0021
Reconstruction	ε_Z^{reco}	0.9245 ± 0.0014	0.9245 ± 0.0014
L0 algorithm	ε_Z^{L0}	0.9984 ± 0.0002	0.9984 ± 0.0002
L1 algorithm	ε_Z^{L1}	0.9536 ± 0.0012	0.9536 ± 0.0012
HLT algorithm	ε_Z^{HLT}	0.9626 ± 0.0011	0.9626 ± 0.0011
Kinematic acceptance	A_Z^{kin}	0.9059 ± 0.0017	0.9059 ± 0.0017
Total efficiency	ε_Z^{total}	0.3575 ± 0.0018	0.0940 ± 0.0020

Table 4.2: Acceptance, reconstruction and trigger efficiencies for $Z \to \mu^+\mu^-$ events at LHCb. The total efficiencies for a cross-section measurement within $1.7 < y < 4.9$ and for an extrapolation to a total (4π) measurement are given. Statistical errors are shown.

associated measurement uncertainties are discussed in section 4.6. From simulation ε_Z^{reco} has been determined to be $0.9245 \pm 0.0014(stat.)$.

The total trigger efficiency is defined from the combination of the conditional probabilities that an event passes each trigger stage.

$$\varepsilon_Z^{trigger} = \varepsilon_Z^{L0} \times \varepsilon_Z^{L1} \times \varepsilon_Z^{HLT} \tag{4.6}$$

Here ε_Z^{L0} is the fraction of events that can be reconstructed offline that would pass the L0 trigger algorithm, ε_Z^{L1} is the fraction of events that can be reconstructed offline and pass the L0 trigger that also pass the L1 trigger algorithm and, finally, ε_Z^{HLT} is the fraction of events that can be reconstructed offline and pass the L0 and L1 trigger stages that will also pass the HLT algorithm. The efficiency of each trigger stage will be greater than 95%. This represents an improvement over previous studies[63] due to improvements in the dimuon trigger line as a result of more precise determination of the muon charge that the author showed was possible at level 1[72].

At LHCb the reconstruction and trigger efficiencies for $Z \to \mu^+\mu^-$ events will be high. Table 4.2 summarises the acceptances and efficiencies for these events at LHCb. The acceptance due to our offline kinematic selection criteria, A_Z^{kin}, is discussed in section 5. The total efficiency, ε_Z^{total}, as a function of the Z boson rapidity and transverse momentum is shown in figures 4.10(a) and 4.10(c) while figures 4.10(b) and 4.10(d) show the variations in the reconstruction resolution of the Z boson rapidity and transverse momentum for events that are triggered, reconstructed and selected at LHCb.

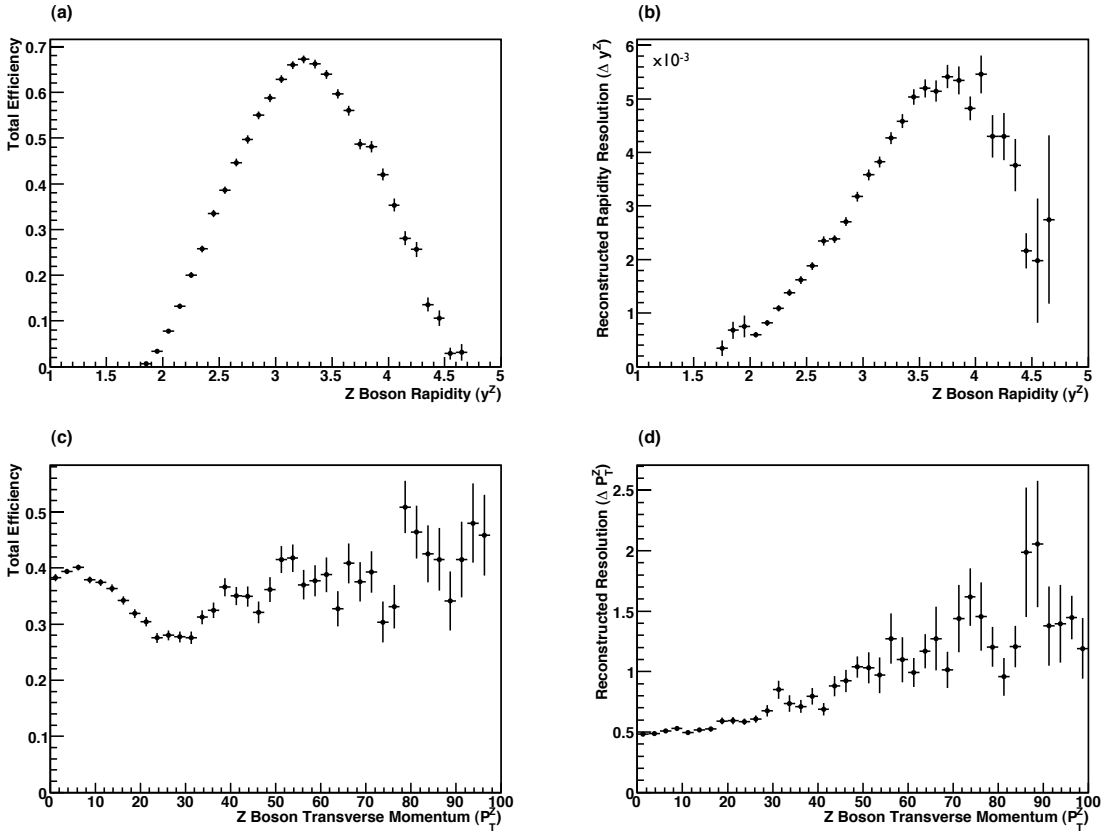

Figure 4.10: Total efficiency for triggering, reconstructing and selecting $Z \to \mu^+\mu^-$ events at LHCb: (a) as a function of Z boson rapidity and (c) as a function of Z boson transverse momentum (for events with $1.7 < y < 4.9$). (b) and (d) show the variations in the reconstruction resolutions for the Z boson rapidity and transverse momentum respectively.

4.4 Background processes

The backgrounds to our signal are electroweak processes such as $Z \to \tau^+\tau^-$ where both taus decay to muons and neutrinos, QCD processes such as $b\bar{b} \to \mu^+ + \mu^- + X$ and events where two hadrons with an invariant mass near the Z mass are both mis-identified as muons. Large four vector Monte-Carlo samples of each background type, generated using PYTHIA, have been analysed. The electroweak and QCD background samples that have been studied are summarised in table 4.3 and are described in the following sections.

For each of these background samples any event that contains at least two oppositely charged muons with pseudorapidity values in the range, $1.9 < \eta < 4.9$ and having $P_T > 1$GeV/c and $P > 8$GeV/c has been examined as a potential background event.

Background process	$\sigma \times BR$ (pb)	Events generated	$\int \mathcal{L}dt$ equivalent
$Z \to \tau^+\tau^- \to \mu^+\nu_\mu\bar{\nu}_\tau + \mu^-\bar{\nu}_\mu\nu_\tau$	72	$144K$	$2fb^{-1}$
$Z \to b\bar{b} \to \mu^+ + \mu^- + X$	82	$164K$	$2fb^{-1}$
W^+W^- *inclusive*	76	$152K$	$2fb^{-1}$
$jet + W^\pm \to \mu^\pm + X$	2×10^4	$8M$	$400pb^{-1}$
$b\bar{b} \to \mu^+ + \mu^- + X$	5×10^6	$50M$	$10pb^{-1}$
$c\bar{c} \to \mu^+ + \mu^- + X$	3.5×10^7	$350M$	$10pb^{-1}$
$J/\psi \to \mu^+\mu^-$	4.63×10^6	$46.3M$	$10pb^{-1}$
Single top inclusive	200	$400K$	$2fb^{-1}$
$t\bar{t}$ *inclusive*	470	$940K$	$2fb^{-1}$

Table 4.3: Electroweak and QCD background samples, produced using the PYTHIA Monte-Carlo generator, that have been used in this analysis.

4.4.1 Electroweak processes

Events where muons are produced either directly or indirectly by the decay of weak bosons can mimic the event characteristics of the process $Z \to \mu^+\mu^-$. The dimuon invariant mass, muon transverse momentum and muon impact parameter significance distributions for such events are shown in figure 4.11.

The Z decay channels $Z \to \tau^+\tau^- \to \mu^+\nu_\mu\bar{\nu}_\tau + \mu^-\bar{\nu}_\mu\nu_\tau$ and $Z \to b\bar{b} \to \mu^+ + \mu^- + X$ are both significantly suppressed by the square of the branching ratios $Br(\tau \to \mu\nu\bar{\nu})$ and $Br(b \to \mu + X)$ respectively. As can be seen in figure 4.11(a) the dimuon invariant mass distributions for both of these processes are peaked in the region $20GeV/c^2 - 40GeV/c^2$ and fall off for higher invariant masses. The muonic decay of single W bosons that have been produced in association with a jet that contains at least one muon, and the production of W^+W^- pairs that both subsequently decay to muons have also been considered. The former has an effective cross-section and invariant mass distribution that are similar to the two Z background channels, while the latter has a much lower cross-section but an invariant mass distribution that is flatter and extends into the higher mass region near the Z mass. All of the electroweak backgrounds have similar effective cross-sections of the order of 0.01pb near the Z mass; this is about four orders of magnitude lower than the signal cross-section in this region.

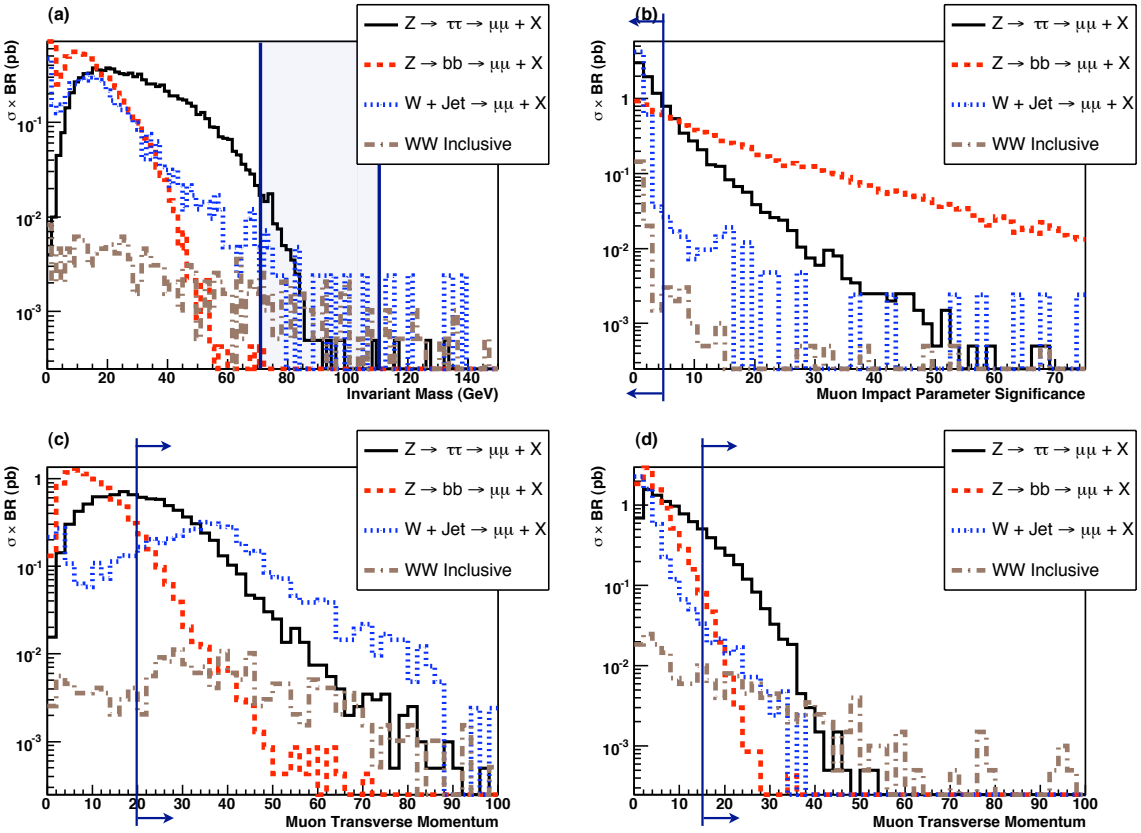

Figure 4.11: Kinematic distributions for various Electroweak background processes. (a) Dimuon invariant mass in units of GeV/c^2. (b) Impact parameter significance of the muon in each event with the higher transverse momentum value. (c) Transverse momentum (P_T) for the muon in each event with the higher P_T, in units of GeV/c. (d) Transverse momentum (P_T) for the muon in each event with the lower P_T, in units of GeV/c. The off-line kinematic selection criteria discussed in section 5 are highlighted. The y-axes are in log scale in units of picobarns.

4.4.2 QCD processes

It is expected that the main QCD background contribution will come from the decay $b\bar{b} \to \mu^+ + \mu^- + X$. This background has been estimated by studying event samples where both of the B hadrons produced in the initial interaction are forced to decay semi-leptonically to muons. The dimuon invariant mass distribution for such events, shown in figure 4.12(a), falls off rapidly with increasing invariant mass and is expected to have an effective cross-section in our signal region near the Z mass of $\sim$1pb. Typically the muons in these events will have much softer transverse momentum values and larger impact parameter significance values than our signal events (see figures 4.12(b), 4.12(c) and 4.12(d)). In a similar way the background contribution due to the decay $c\bar{c} \to \mu^+ + \mu^- + X$ has also been investigated. These events have dimuon invariant mass, muon transverse momenta and muon impact parameter significance distributions that are very similar to the $b\bar{b} \to \mu^+ + \mu^- + X$ events. The background contribution due to the decay of top quarks has also been estimated by examining $t\bar{t}$ and single top

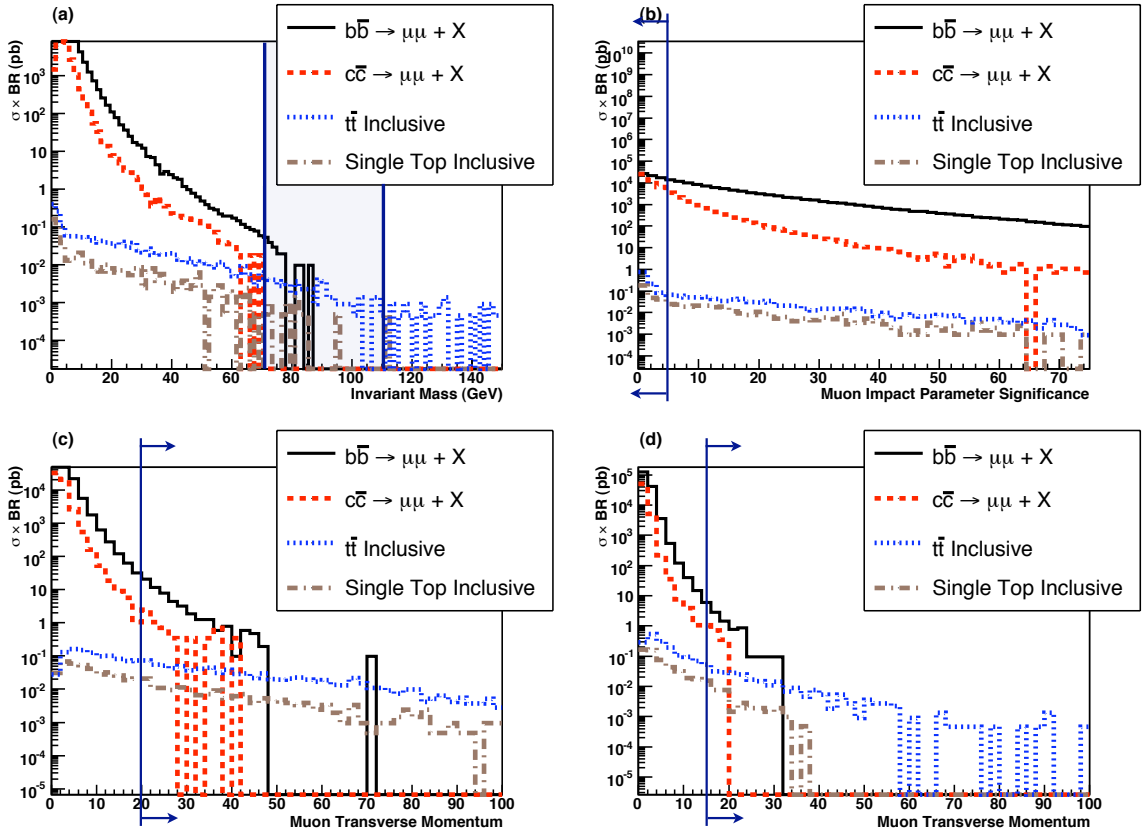

Figure 4.12: Kinematic distributions for various QCD background processes. (a) Dimuon invariant mass in units of GeV/c^2. (b) Impact parameter significance of the muon in each event with the higher transverse momentum value. (c) Transverse momentum (P_T) for the muon in each event with the higher P_T, in units of GeV/c. (d) Transverse momentum (P_T) for the muon in each event with the lower P_T, in units of GeV/c. The off-line kinematic selection criteria discussed in section 5 are highlighted. The y-axes are in log scale in units of picobarns.

events. The spectra for such events are harder but have a much smaller cross-section. The effective cross-section for these events in our signal region will be $\sim$0.01pb.

4.4.3 Hadron mis-identification

The last important source of background events comes from random combinations of oppositely charged pions or kaons that are both mis-identified as muons. The magnitude of this background contribution has been estimated in the following manner. Firstly it was necessary to make an estimate of the probability of pion/kaon mis-identification as a function of pion/kaon momentum since the current hadron mis-identification studies at LHCb have only dealt with pions and kaons that have momenta below $\sim$150GeV/c. This is achieved by assuming that there are two principal ways in which mis-identification can occur, decay in flight and *punchthrough*. The next two sections outline how these two contributions were estimated.

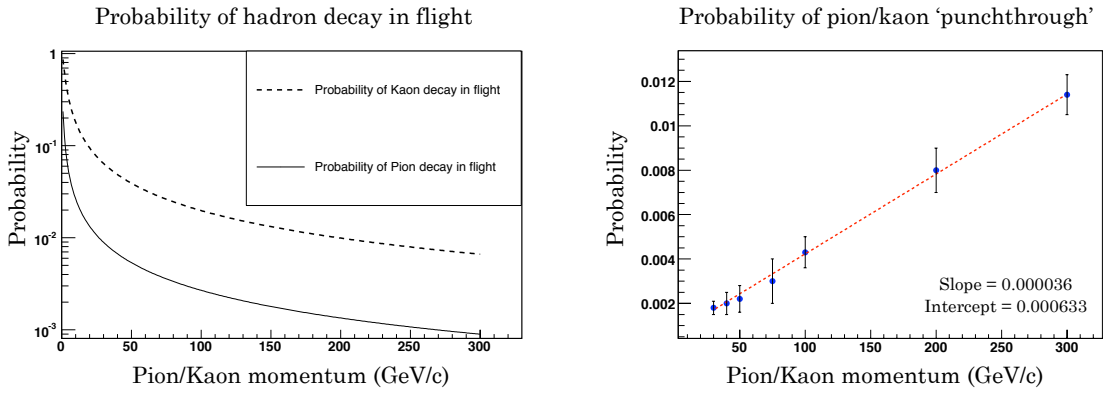

(a) (b)

Figure 4.13: Probability of pion/kaon mis-identification as a function of pion/kaon momentum due to (a) pion/kaon decay in flight and (b) pion/kaon punchthrough parameterised by the straight line fit (dashed line) to the RD5 measurements (from[73]) shown with error bars.

This is followed by a description of how this mis-identification probability was used to estimate the background from this source.

Decay in flight

This mis-identification occurs when a charged pion or kaon is produced at or near the primary vertex and subsequently decays into a muon and a neutrino ($Br(\pi^\pm \to \mu^\pm \nu_\mu) \approx 1$ and $BR(K^\pm \to \mu^\pm \nu) = 0.6343$) somewhere between the vertex locator (VELO) and the muon chambers. The resulting muon chamber hits can then be associated to the pion/kaon track in the VELO leading to the reconstruction of a muon with a track coming from the interaction region. This source of mis-identification can be theoretically estimated since it is possible to calculate the mean decay length in the laboratory frame. For pions this decay length is

$$c\tau_\pi^{Lab} = \gamma c\tau_\pi^{Rest} = \frac{cE_\pi\tau_\pi^{Rest}}{M_\pi} \approx \frac{cP_\pi\tau_\pi^{Rest}}{M_\pi} = 55.8P_\pi \tag{4.7}$$

while for kaons it is

$$c\tau_K^{Lab} = \gamma c\tau_K^{Rest} = \frac{cE_K\tau_K^{Rest}}{M_K} \approx \frac{cP_K\tau_K^{Rest}}{M_K} = 7.52P_K \tag{4.8}$$

Here c is the speed of light in vacuum, γ is the relativistic Lorentz factor and $E_\pi(E_K)$, $P_\pi(P_K)$ and $M_\pi(M_K)$ are the pions(kaons) energy, momentum and mass respectively. This leads to a pion probability of decay in flight in the $\sim 15m$ between the VELO and the muon chambers

of

$$1 - \exp(\frac{-0.269}{P_\pi}) \tag{4.9}$$

and a corresponding kaon decay in flight probability of

$$1 - \exp(\frac{-1.994}{P_K}) \tag{4.10}$$

where P_π and P_K are in units of GeV/c. These functional forms are illustrated in figure 4.13(a). It is assumed that the mis-identification probability from this source is equal to this decay in flight probability. It should be noted that this is an over-estimate since it assumes that every pion/kaon that decays in this way will result in the association of its VELO track and the corresponding muon chamber hits.

Punchthrough

This is due to pions or kaons that are sufficiently energetic to pass through the hadronic calorimeter and iron shielding, loosing some of their energy in the process, before depositing the remainder of their energy in the muon chambers. This occurrence is commonly referred to as hadron *punchthrough*. This contribution was dealt with in the following way. Firstly it was assumed that only pions or kaons that have penetrated all the way through to the final muon chamber M5 will be mis-identified. For this to happen the pion or kaon would have to traverse 21 interaction lengths. Measurements of the probability of such an occurrence for pions with a momentum of 30, 40, 50, 75, 100, 200 and $300 GeV/c$ have been made by the RD5 collaboration at CERN[73]. Figure 4.13(b) shows a straight line fit to these measurements. Based on this fit the punchthrough probability, S, can be parameterised as

$$S = 0.00063 + 3.6 \times 10^{-5} P_\pi \tag{4.11}$$

where P_π is the pion momentum in units of GeV/c. In what follows it is assumed that the kaon punchthrough probability will have the same momentum dependence. Comparing figures 4.13(a) and 4.13(b) we can expect punchthrough to be the dominant cause of mis-identification for pions with momenta greater than $\sim 80 GeV/c$ and kaons with momenta above $\sim 200 GeV/c$. Since typically the pions and kaons causing our background will have momenta values in the range $100 GeV/c - 1 TeV/c$, it would be beneficial to remove the punchthough contribution for high momenta hadrons. This can be achieved by requiring that any track must have less than $50 GeV$ of hadronic energy associated with it in order for it to be considered a muon track. The effect of this cut has been assessed using measurements of the energy lost by pions and kaons with momenta of 30, 50, 100 and $300 GeV/c$ when they pass through a calorimeter of depth $10\lambda_I$. These measurements were made by the RD5 collaboration using a calorimeter consisting of interleaved stainless steel plates and Honeycomb Strip Chambers (see[74]). In what follows it is assumed that the same amount of energy will be lost by pions and kaons passing through the LHCb hadronic calorimeter, which will have a depth of $7.3\lambda_I$

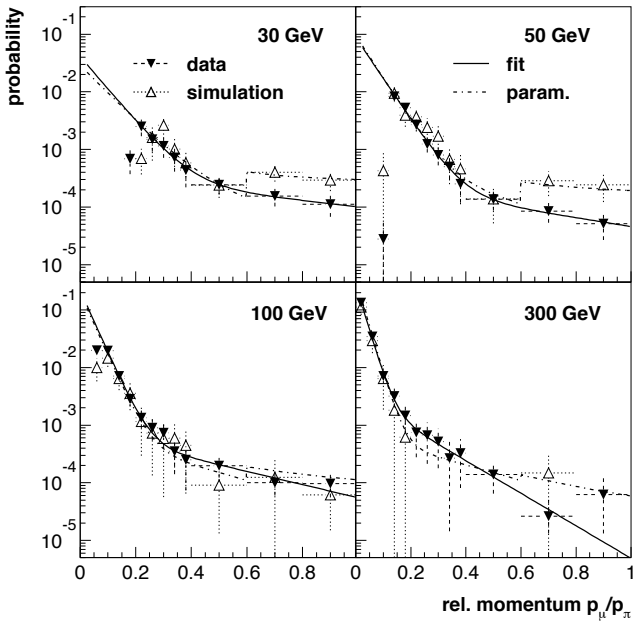

Figure 4.14: Probability that a pion will fully traverse a $10\lambda_I$ calorimeter and emerge with a momentum P_μ that is some fraction, z, of the initial pion momentum P_π. Four different data sets are shown having initial pion momenta of 30, 50, 100 and 300GeV/c. Data are represented by solid triangles while hollow triangles represent the full GEANT simulation. The solid line shows a fit of a double exponential to the data. From[74].

and that all of this energy will be collected. Figure 4.14, taken from[74], shows the probability that a pion will fully traverse a $10\lambda_I$ calorimeter and emerge with a momentum P_μ that is some fraction, z, of the initial pion momentum P_π. The RD5 collaboration have fitted a double exponential function of the form $f = a_1 \exp(b_1 z) + a_2 \exp(b_2 z)$, where z is the relative momentum P_μ/P_π, to the four data sets shown in figure 4.14. This fit is also in good agreement with the corresponding kaon data sets. Of the four fit parameters, a_1 and b_1 depend on the initial pion momenta values while a_2 and b_2 are constants. In order for a punchthrough pion or kaon to pass our proposed hadronic energy cut it will need to have a relative momentum in the range $(1 - \frac{50GeV/c}{P_\pi}) < z < 1$. The total probability for this to occur is

$$\int_{(1-\frac{50GeV/c}{P_\pi})}^{1} a_1 \exp(b_1 z) + a_2 \exp(b_2 z)\, dz \tag{4.12}$$

which decreases with increasing pion momenta as shown in figure 4.15. Based on this we expect that, for pions and kaons with momenta values above 100GeV/c and 200GeV/c respectively, the proposed hadronic energy cut will reduce the punchthrough contribution to a level that is two orders of magnitude lower than the decay in flight contribution. It should be noted that this is an overestimate of the punchthrough contribution since it does not take into account the reduction due to the fact that these pions and kaons would have to pass through all of the muon stations in order for them to be mis-identified.

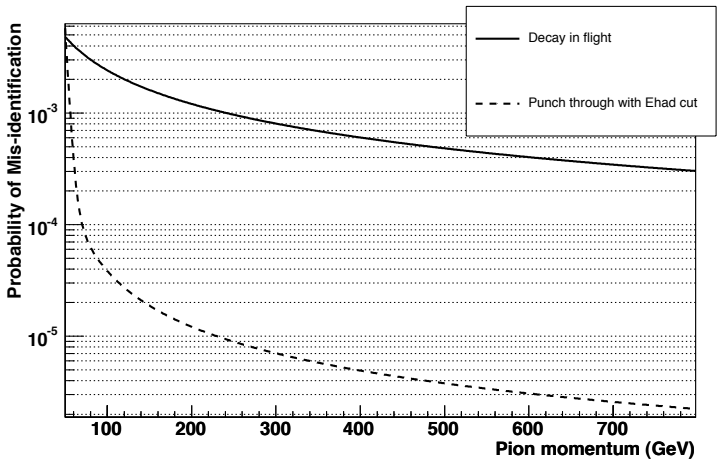

Figure 4.15: Probability of pion/kaon mis-identification as a function of pion/kaon momentum (in units of GeV) after the hadronic energy cut is applied (E_{Had} <50GeV) , due to decay in flight (solid line) and pion/kaon punchthrough (dashed line).

Background estimate

A sample of ten million minimum bias[3] events was generated using PYTHIA. Then, only considering pions and kaons that had pseudorapidity values in the range 1.9< η <4.9 and momenta satisfying P >8GeV/c and P_T >1GeV/c, all of the opposite charge pairwise hadron combinations (i.e. $\pi^+\pi^-$, $K^+\pi^-$, $K^-\pi^+$ and K^+K^-) in these events were recorded. The probability of mis-identification for each hadron was calculated and an overall weighting assigned to each dihadron combination based on these probabilities. The various distributions for these dihadron combinations using PYTHIA v6321, with and without applying the hadronic energy cut outlined above, are shown in figure 4.16. Note that applying the proposed hadronic energy cut reduces the effective cross-section of the pion/kaon background by two orders of magnitude in the signal region near the Z mass.

This background estimate was performed twice using two different PYTHIA versions, v6321 and v6406, in an attempt to estimate the theoretical uncertainty on the expected rate of such events. A large difference between the two versions, caused by a change in the way PYTHIA treats low-P_T events (MSUB 95) was found. Applying the kinematic cuts outlined in the next section to these samples gives an effective cross-section of 9.940pb for v6321 but only 0.032pb for v6406. There is much theoretical uncertainty on the modelling of low-P_T events and these numbers reflect that. Clearly this background must be found from the data themselves. For accounting purposes we will estimate this background in advance as (5 ± 5)pb.

[3]Corresponding to the PYTHIA process (ISUB) flags 11, 12, 13, 28, 53, 68, 86, 87, 88, 89, 91, 92, 93 ,94, 95, 106, 107 and 108.

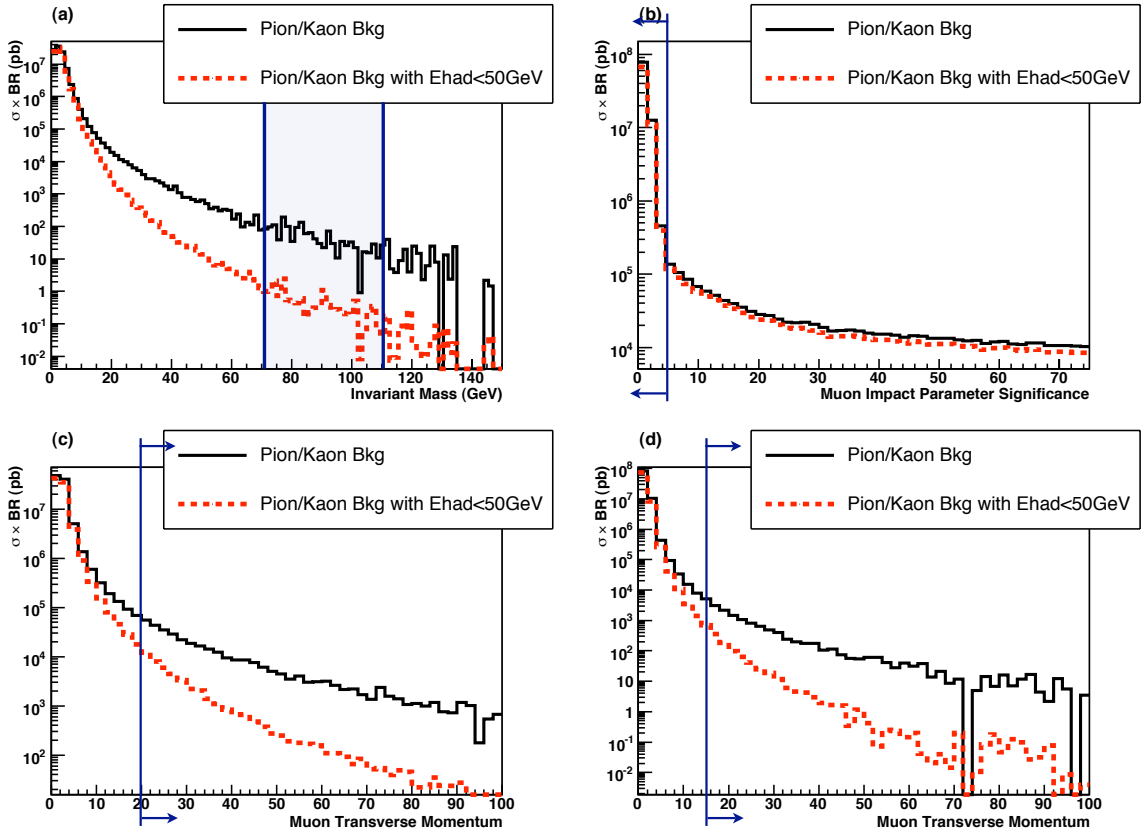

Figure 4.16: Kinematic distributions for background events due to Pion or Kaon mis-identification both for where an E_{had} cut is applied and when it is not. (a) Dimuon invariant mass in units of GeV/c^2. (b) Impact parameter significance of the muon in each event with the higher transverse momentum value. (c) Transverse momentum (P_T) for the muon in each event with the higher P_T, in units of GeV/c. (d) Transverse momentum (P_T) for the muon in each event with the lower P_T, in units of GeV/c. The off-line kinematic selection criteria discussed in section 4.5 are highlighted. The y-axes are in log scale in units of picobarns.

4.5 Signal selection and background reduction

Given the dimuon invariant mass, muon momenta and muon impact parameter significance distributions of our signal events as shown in figures 4.7 and 4.8, and the corresponding background distributions as shown in figures 4.11, 4.12 and 4.16, the following kinematic cuts are proposed:

1. The dimuon invariant mass must be in the range $71 GeV/c^2 < M_{\mu\mu} < 111 GeV/c^2$.
2. The muon with the highest transverse momentum must satisfy $P_T > 20 GeV/c$.
3. The muon with the lowest transverse momentum must satisfy $P_T > 15 GeV/c$.
4. Both muons must satisfy $IPS < 5$.
5. Both muons should have less than 50GeV of hadronic energy associated to their track.

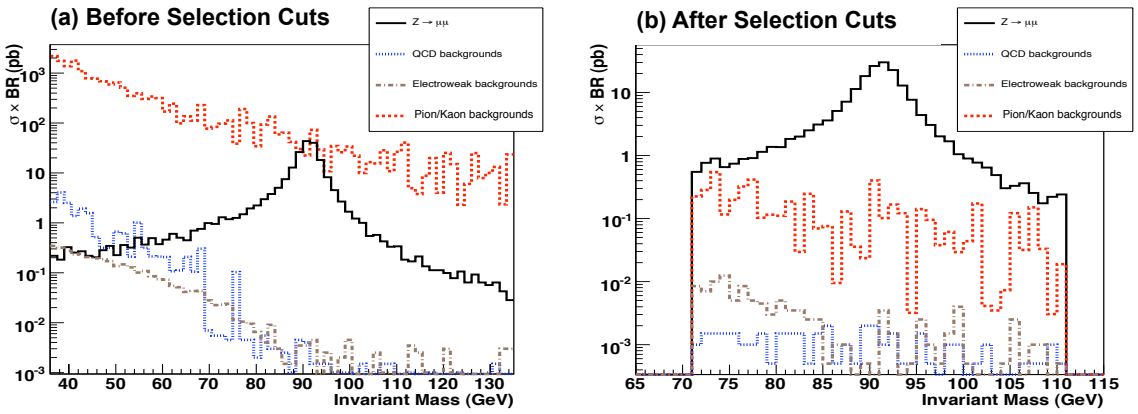

Figure 4.17: The dimuon invariant mass distributions for the signal and background processes: (a) Before selection cuts are applied and (b) After the application of the off-line kinematic selection criteria described in section 4.5.

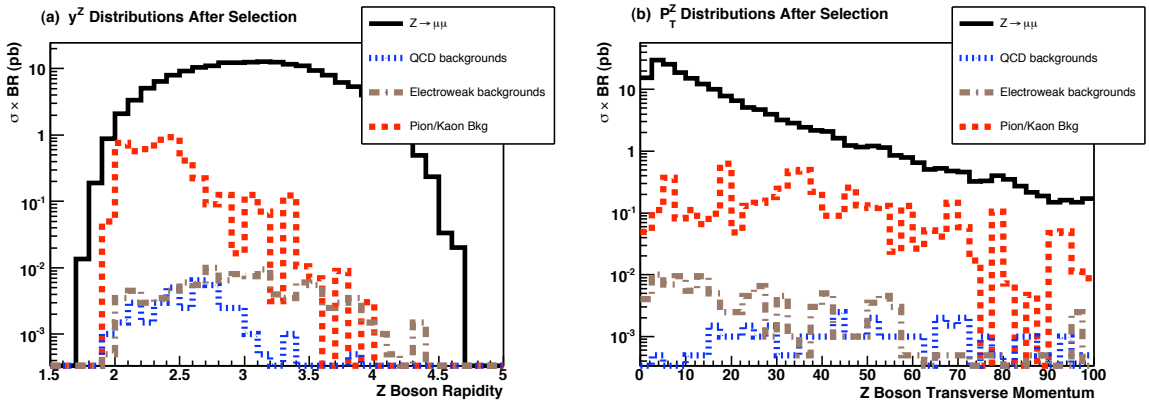

Figure 4.18: (a) Reconstructed Z boson rapidities for signal and background events that pass the offline kinematic selection criteria. (b) Reconstructed Z boson transverse momenta, in units of GeV/c, for signal and background events that pass the offline kinematic selection criteria.

The signal acceptance for these offline kinematic cuts, A_Z^{kin}, is defined to be the fraction of offline reconstructed $Z \to \mu^+\mu^-$ events passing all of the trigger stages that also satisfy these kinematic requirements. Using the full detector simulation A_Z^{kin} was determined to be 0.9059 ± 0.0017. Combining this with the geometric acceptance and the reconstruction and trigger efficiencies given in section 3 yields an overall efficiency of $0.3575 \pm 0.0018(stat.)$ $(0.094 \pm 0.002(stat.))$ for $Z \to \mu^+\mu^-$ events produced in the forward region $(1.7 < y < 4.9)$ (inside 4π). This gives an effective signal cross-section of $\sim$172.54pb which corresponds to $172,540 \pm 869(stat.)$ events in half a nominal year of LHCb running ($1 fb^{-1}$ of data).

Applying the cuts to the background samples described in section 4 reduces the background to a level that is $(3.0 \pm 2.9)\%$ of the expected signal rate. This equates to $\sim$5160 background events per $1 fb^{-1}$. The background is dominated by events caused by pion/kaon mis-

Process	Events per fb^{-1}
$Z \to \mu^+\mu^-$ (signal)	172540 ± 869
$Z \to \tau^+\tau^- \to \mu^+\nu_\mu\bar{\nu}_\tau + \mu^-\bar{\nu}_\mu\nu_\tau$	63.5 ± 5.6
$Z \to b\bar{b} \to \mu^+ + \mu^- + X$	$0 + 0.5$
W^+W^- *inclusive*	24 ± 3.5
$jet + W^\pm \to \mu^\pm + X$	35 ± 13.2
$b\bar{b} \to \mu^+ + \mu^- + X$	< 230 (CL=90%)
$c\bar{c} \to \mu^+ + \mu^- + X$	< 230 (CL=90%)
$J/\psi \to \mu^+\mu^-$	< 230 (CL=90%)
Single top inclusive	0.5 ± 0.5
$t\bar{t}$ *inclusive*	37 ± 4.3
$Pion/Kaon\ mis-identification$	5000 ± 5000
Total Background	5160 ± 5003

Table 4.4: The expected number of events for the signal and background sources per fb^{-1} of data after the selection cuts outlined in section 4.5 have been applied. The value for the signal process takes into account the overall experimantal efficiency and assumes a $Z \to \mu^+\mu^-$ cross-section of 1.8nb. Statistical uncertainties are shown.

identification at a rate of 5000 ± 5000 events per $1fb^{-1}$. In principle it should be possible to accurately assess the level of pion/kaon background from data once they arrives.

The effect of the cuts is shown in figure 4.17 which plots the invariant mass distributions of the signal and background processes before and after the cuts are applied. The level of background contamination after these cuts have been applied as a function of reconstructed Z boson rapidity and transverse momentum is shown in figure 4.18. These results are summarised in table 4.4. It should be noted the uncertainties given in table 4.4 are statistical only and are due to our limited Monte-Carlo sample sizes. Systematic uncertainties are discussed in the next section.

A major benefit of using a cut-based selection rather than a more abstract multi-variate technique is that assessing the impact of systematic shifts in the cut distributions is comparatively easy. In order to assess the robustness of the chosen selection criteria (i.e. to ensure that they are not near the edge of a region with much worse performance) a scan has been performed around the chosen kinematic cuts. The range of these scans was determined by the reconstruc-

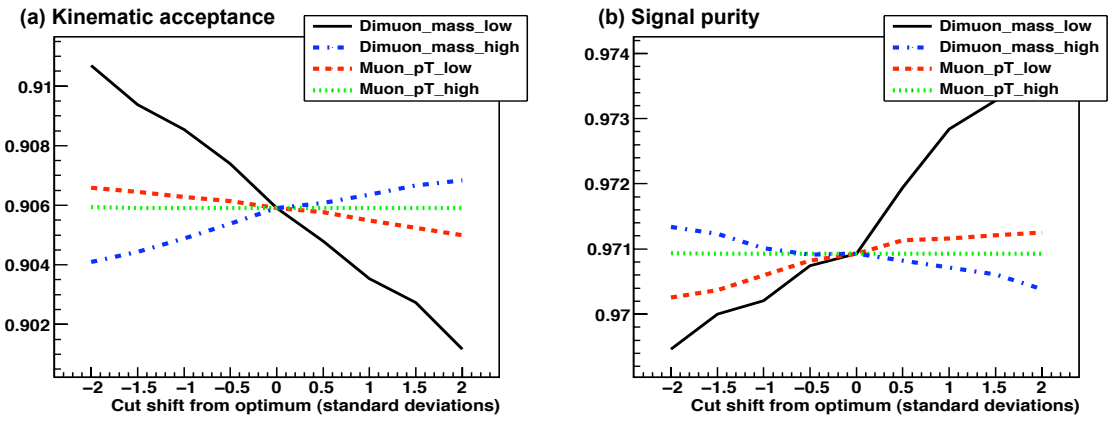

Figure 4.19: Changes in (a) kinematic acceptance and (b) signal purity as a function of variation of the cut values. The variations are between -2σ and $+2\sigma$ from the chosen cuts, where σ is the reconstruction resolution on each parameter.

tion resolution σ on each parameter. The effect on the kinematic acceptance and signal purity of $\pm 2\sigma$ variations on the selection criteria are shown in figures 4.19(a) and 4.19(b) respectively. From these plots it can be concluded that the chosen cut values are not near sensitive regions of parameter space, i.e. there are no rapid changes in either the acceptance or purity.

4.6 Systematic and statistical uncertainties

From equation 4.1 it can be seen that the accuracy with which a measurement of $\sigma_Z \cdot Br(Z \to \mu^+\mu^-)$ can be made will be limited by the statistical and systematic uncertainties on: the number of $Z \to \mu^+\mu^-$ candidates observed, the expected number of background events, the geometric and kinematic acceptances, the trigger and reconstruction efficiencies and the integrated luminosity. The uncertainties from each of these sources will now be discussed in turn. The estimated systematic uncertainties from each source are summarised in table 4.7.

4.6.1 Signal candidates

The uncertainty on the number of $Z \to \mu^+\mu^-$ candidates observed, N_Z^{obs}, will be purely statistical. Assuming a $Z \to \mu^+\mu^-$ cross-section of 1.8nb, and using the efficiency and acceptance values we have obtained from simulation, a 1% uncertainty on N_Z^{obs} will require 10,000 events which equates to $\simeq 46 pb^{-1}$ of data.

4.6.2 Expected backgrounds

The main contribution to the expected number of background events, N_Z^{back}, will come from $b\bar{b} \to \mu^+ + \mu^- + X$ events and events due to pion/kaon mis-identification.

Pions/kaons mis-id: It will be possible to measure the background due to pion and kaon mis-identification from data. This can be achieved by measuring the muon mis-identification rate of a pure sample of pions or kaons. For example for pions this can be achieved by examining the pions coming from the decays $K_s \to \pi^+\pi^-$ and $\Lambda \to p\pi^-$. Combining these mis-identification probabilities with the measured rate of events containing a di-hadron combination with an invariant mass in the range $71GeV/c^2 < M_{hh} < 111GeV/c^2$ will enable the background to be evaluated. Assuming samples of 100,000 pions and kaons in our momentum range ($P_h > 100GeV/c$), we estimate that the systematic uncertainty on such a measurement will be ± 500 events per fb^{-1} of data.

B meson decay: The number of background events from $b\bar{b} \to \mu^+ + \mu^- + X$ given in table 4.4 assumes the $b\bar{b}$ cross-section at the LHC will be $500\mu b$. However, the current predicted value of this cross-section, based on extrapolation from SPS and Tevatron data, is in the range 175 to $950\mu b$[75]. The uncertainty on this cross-section is therefore estimated to be $\pm 500\mu b$: equating to a systematic uncertainty on this background source of ± 100 events per fb^{-1} of data.

4.6.3 Acceptances

The acceptances, A_Z^{geom} and A_Z^{kin}, describing the effect of geometric and kinematic cuts, will be determined from simulation. The value of A_Z^{geom}, presented in section 3, has been calculated to NLO using MCFM and the MRST2001nlo PDF set while A_Z^{kin} has been obtained using a leading order event generator (PYTHIA) and a LO PDF set (CTEQ5L). It should also be noted that these values have been determined using a Monte-Carlo sample of limited size and an untuned detector simulation. In addition, our understanding of the muon P_T and dimuon invariant mass distributions, which are used in our kinematic selection, will depend on our understanding of two parameters, the momentum scale s and the momentum resolution, both of which will be determined from data. The likely systematic uncertainties from higher order corrections, PDF uncertainties, the size of our Monte-Carlo sample, the detector simulation and the determination of the momentum scale and momentum resolution will now be discussed in turn.

Higher order corrections: As already stated in section 4.3, A_Z^{geom} will be sensitive to the production angle of Z bosons in LHC collisions and hence will depend on the differential production cross-section $d\sigma/dy$ of the Z bosons. The geometric acceptance estimates presented in this chapter have been determined to NLO. Production mechanisms at NNLO or higher orders can produce different event topologies and will result in different $d\sigma/dy$ distributions. This uncertainty in the predicted $d\sigma/dy$ shape will not introduce an additional systematic uncertainty on a cross-section measurement within the instrumented region ($1.7 < \eta < 4.9$) - we will measure the shape by making a bin-by-bin correction using the distribution shown in fig-

ure 4.9. It will, however, introduce a systematic uncertainty on any extrapolated measurement outside the instrumented region, a total cross-section measurement for example. This systematic uncertainty has been estimated by comparing the geometric acceptances calculated using the $d\sigma/dy$ distributions produced by a NLO calculation using either a NLO or NNLO PDF set (MRST2001nlo and MRST2001nnlo[76]). The change in the geometric acceptance for a total cross-section measurement was determined to be 0.08% - this value is taken to be the systematic uncertainty from this source. The comparison between NLO and a full NNLO calculation will be done before data-taking (using, for example, the FEWZ Monte-Carlo generator[77]). We do not anticipate that this will alter our systematic uncertainty estimate significantly.

PDF uncertainties: The choice of PDF set will have an affect on the $d\sigma/dy$ distributions and will consequently affect the acceptances. Again, this will only introduce a systematic uncertainty on the total cross-section measurement not on a measurement in the forward region where the LHCb detector can reconstruct $Z \to \mu^+\mu^-$ events. The uncertainty in the acceptance due to uncertainties in the PDF sets was evaluated using the MRST and CTEQ *error* PDF sets MRST01E[78] and CTEQ6mE[79]. The MRST(CTEQ) PDF parameterisation is based on 15(20) parameters, P_i, that are tuned to their most likely values using a χ^2 minimisation to the experimental data. Since these parameters are correlated, both the MRST and CTEQ groups transform them into a set of linearly independent eigenvectors, Q_i, that have a diagonal covariance matrix. The different error PDF sets are produced by varying a given eigenvector by $+1\sigma$ or -1σ and transforming back into the P_i parameter space. This results in a total of 30 MRST (40 CTEQ) PDF sets. The percentage change in the geometric acceptance for a total cross-section measurement for each of these PDF sets was evaluated. These results are shown in figure 4.20 and are summarised in tables 4.5 and 4.6. Adding the positive and negative changes separately in quadrature results in an overall percentage uncertainty on the geometric acceptance for a total cross-section measurement of $^{+2.340}_{-2.704}$ for the CTEQ sets and $^{+1.257}_{-1.732}$ for the MRST sets. Since the estimated uncertainties on the CTEQ PDF sets are larger than those on the MRST PDF sets we, for now, use the CTEQ values when calculating the overall systematic uncertainty. In the meantime work with theorists is currently on going to define a more consistent procedure for such evaluations. It should be noted that these PDF uncertainties will be the dominant systematic uncertainty in any measurement of the total (4π) Z production cross-section using data from LHCb.

Monte-Carlo statistics: The statistical uncertainties on the distribution shown in figure 4.9(b), which is used to determine the acceptance, will be a source of systematic uncertainty. Currently, as can be seen in figure 4.21, with rapidity bins of width 0.1 the uncertainty on each bin is smallest for rapidities corresponding to the middle of the LHCb detector, where they reach a minimum value of $\sim 1.4\%$, and get progressively larger towards the detector edges where they are $>10\%$. Clearly this uncertainty is dependent on both the choice of bin size and the size of the Monte-Carlo sample used. The sample used in this study consists of 99,500 events that pass the generator cuts outlined in section 4.3 - of these $\sim$35,000 contain a dimuon pair that originated from a decaying Z and are both reconstructible at Monte-Carlo truth level. Figure 4.21 also shows the expected uncertainty, using the same bin size, that would be obtained with Monte-Carlo samples that are 10 and 100 times larger than the samples used in this study -

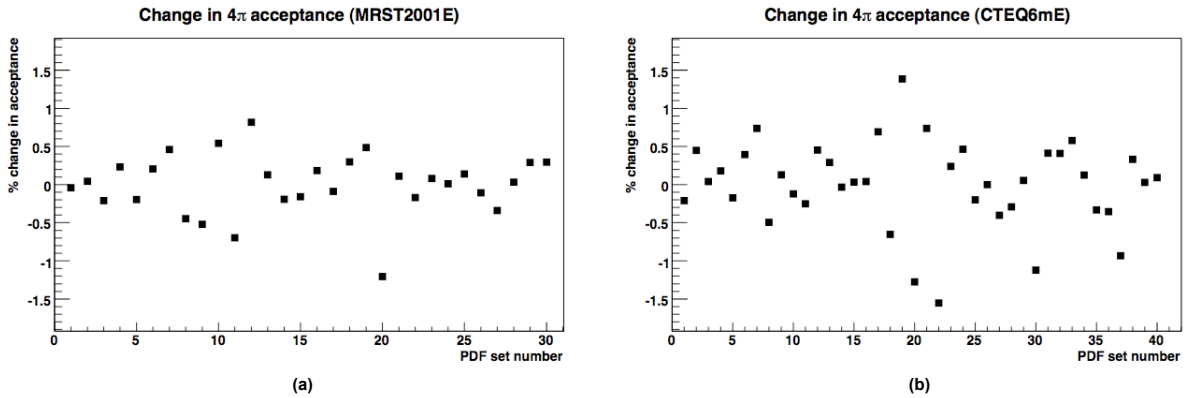

Figure 4.20: Percentage variations in the acceptance of $Z \to \mu^+\mu^-$ events for a total cross-section measurement at LHCb for various PDF sets. The variations from the MRST error sets are shown in (a) while (b) shows the variations due to the CTEQ error sets. The PDF set numbers refer to the $\pm 1\sigma$ variations in the eigenvectors Q_i. For example sets 1 and 2 are produced by varying the eigenvector Q_1 by $+1\sigma$ and -1σ respectively.

corresponding to 10^6 and 10^7 events respectively. With a sample that is 10 times larger the uncertainty on each bin in the range $2.3 < y < 4$ would be less than 1% while if a sample 100 times larger is used the uncertainty would be less than 1% over the range $1.9 < y < 4.4$ with uncertainties in the centre of the detector as small as $\sim 0.1\%$. For a cross-section measurement in the forward region or an extrapolation to 4π, the size of the sample used in this study contributes a systematic uncertainty of 0.45%. However, if we want to measure the differential distributions with an uncertainty of $\leq 1\%$ in each bin a larger Monte-Carlo sample will be required. For now the uncertainty arising from this source is neglected and we assume a sample of at least 10^7 events will be generated in the future.

Detector material model: Since the acceptance values must be obtained from simulation, any uncertainties in the detector material description must be taken into account. It is expected that the detector simulation will be retuned using data once they arrive. After such retuning was done at CDF[66] it was found that detector uncertainties had a negligible contribution to the systematic uncertainty on the acceptance for $Z \to \mu^+\mu^-$ events. We conservatively estimate the systematic uncertainty from this source to be 0.1%.

Momentum scale and momentum resolution: The resolutions and pulls of the muon P_T and dimuon invariant mass distributions will depend on two parameters - an overall momentum scale s and a resolution σ - both of which must be determined from data. Since cuts are applied to both the dimuon invariant mass and muon P_T in our offline selection, the uncertainty on the determination of s and σ will lead to a systematic uncertainty on the calculated kinematic acceptance. Since the values of σ and s will effect the width and maximum of the reconstructed Z peak respectively, the mass peak can be used to determine both parameters. It is currently expected that with $10 pb^{-1}$ of data, the momentum resolution and momentum scale can be determined with uncertainties of 0.1% and 7% respectively. A variation of the width of the P_T resolution results in a change to A_{kin} of $\sim 0.05\%$. In contrast, the uncertainty on the

CTEQ6mE	4π measurement	
Eigenvector	$\Delta A_{+1\sigma}$ (%)	$\Delta A_{-1\sigma}$ (%)
Q_1	−0.211	0.450
Q_2	0.040	0.180
Q_3	−0.175	0.395
Q_4	0.735	−0.496
Q_5	0.130	−0.124
Q_6	−0.250	0.454
Q_7	0.290	0.033
Q_8	0.032	−0.041
Q_9	0.693	−0.652
Q_{10}	1.385	−1.276
Q_{11}	0.737	−1.552
Q_{12}	0.238	0.465
Q_{13}	−0.199	0.001
Q_{14}	−0.403	−0.291
Q_{15}	−0.056	−1.122
Q_{16}	0.412	0.408
Q_{17}	0.579	0.125
Q_{18}	−0.331	−0.356
Q_{19}	−0.934	0.332
Q_{20}	0.027	0.092

Table 4.5: Percentage changes to the acceptance of $Z \to \mu^+\mu^-$ events for a total cross-section measurement at LHCb for $\pm 1\sigma$ variations in the 20 CTEQ eigenvectors Q_i.

momentum scale is expected to have a larger impact on A_{kin}. A 0.1GeV/c uncertainty on the momentum scale results in a $\sim$0.15% uncertainty on A_{kin}.

4.6.4 Reconstruction efficiency

As was pointed out in section 3 the reconstruction efficiency can be determined from data and is expressible as the product of three components,

$$\varepsilon_Z^{reco} = (\varepsilon_{trk}^{(1)} \times \varepsilon_{match}^{(1)} \times \varepsilon_{id}^{(1)}) \times (\varepsilon_{trk}^{(2)} \times \varepsilon_{match}^{(2)} \times \varepsilon_{id}^{(2)}) \tag{4.13}$$

We will now outline methods, based on those used by the CDF collaboration[66], that will allow these terms to be measured from data.

MRST2001E	4π measurement	
Eigenvector	$\Delta A_{+1\sigma}$ (%)	$\Delta A_{-1\sigma}$ (%)
Q_1	−0.039	0.044
Q_2	−0.210	0.232
Q_3	−0.196	0.205
Q_4	0.461	−0.448
Q_5	−0.519	0.542
Q_6	−0.698	0.819
Q_7	0.128	−0.192
Q_8	−0.158	0.184
Q_9	−0.090	0.297
Q_{10}	0.487	−1.204
Q_{11}	0.112	−0.169
Q_{12}	0.081	0.010
Q_{13}	0.140	−0.107
Q_{14}	−0.339	0.036
Q_{15}	0.291	0.296

Table 4.6: Percentage changes to the acceptance of $Z \to \mu^+\mu^-$ events for a total cross-section measurement at LHCb for $\pm 1\sigma$ variations in the 15 MRST eigenvectors Q_i.

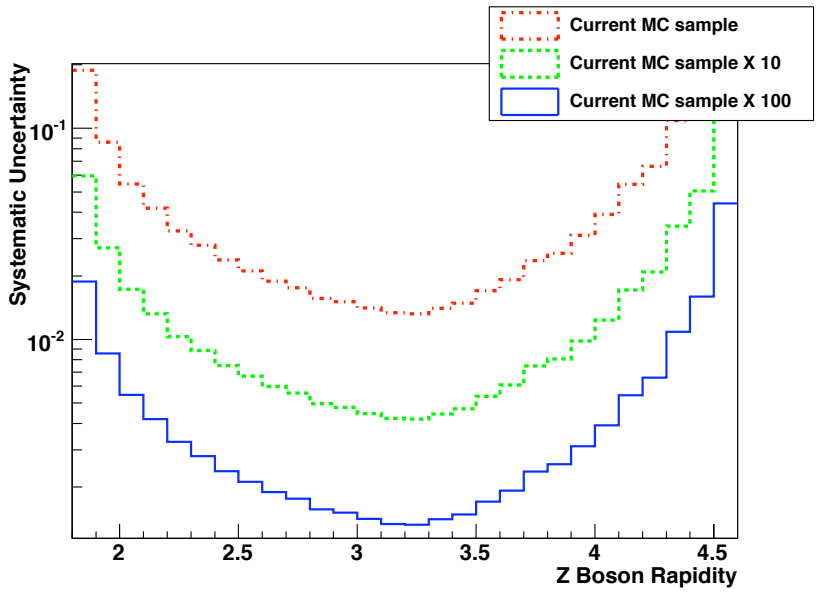

Figure 4.21: Systematic uncertainty due to the limited size of the Monte-Carlo sample used to determine the geometric acceptance. The uncertainty due to the size of the sample used in this study and samples that are 10 and 100 times larger are shown.

Tracking efficiency: ε_{trk} can be determined from data using a pure unbiased sample of $W \to \mu\nu$ candidate events selected using a tight set of selection criteria based on muon chamber information. The fraction of events in such a sample that have a reconstructed track that points to the appropriate muon chamber deposit will give ε_{trk}. Assuming a tracking efficiency of more than 95%, we estimate that a measurement of ε_{trk} using 10^4 muon stubs, equivalent to less than $10pb^{-1}$ of data, will have an associated systematic uncertainty of 0.1%. It should be pointed out that this is the uncertainty on a measurement of the average tracking efficiency - ideally the tracking efficiency should be determined as a function of the track momentum, ϕ and pseudorapidity. The precision to which the tracking efficiency can be determined in this 3D bins is clearly dependent on the number of high momentum tracks available and the bin sizes.

Matching efficiency: The efficiency to reconstruct hits in the muon chambers and match them to reconstructed tracks, ε_{match}, can be found using a data set containing events with at least one high P_T muon, for example events that pass the single muon trigger line and having P_T >10GeV/c. The muon in these events is then combined with all the opposite sign high P_T tracks in the event. If a combination has an invariant mass close to the Z mass and the track points to an active area in the muon chambers the track is considered a candidate. The fraction of these candidate tracks that are actually reconstructed offline as muons will be equal to ε_{match}. With $50pb^{-1}$ of data and a matching efficiency greater than 95%, we estimate that a measurement of ε_{match} will have an associated systematic uncertainty of 0.1%. Once again this quoted uncertainty refers to a measurement of the average matching efficiency for high momentum muons - determining the efficiency as a function of muon momentum, ϕ and η is clearly superior but the accuracy and granularity with which this can be done will be limited by the number of high momentum muons available.

Identification efficiency: The efficiency of any muon identification cuts used to improve the muon purity, ε_{id}, can be determined using a clean sample of muons that have been selected without using the cuts you wish to examine. Such a sample can be obtained from $Z \to \mu^+\mu^-$ events that have passed the trigger via any stream bar the dimuon trigger stream (selecting events from the dimuon stream would bias the sample). One of the legs of the Z can then be used to tag the Z, while the other can be used as a probe to measure the muon id efficiency. The efficiency will be equal to the number of probe muons that pass the id cuts divided by the total number of probe muons. Assuming an id efficiency of 99% and a sample of 10^4 muons, equivalent to $\sim 50pb^{-1}$, an average measurement of ε_{id} using this method will have an associated systematic uncertainty of 0.1%.

4.6.5 Trigger efficiency

It will be possible to determine the trigger efficiency, $\varepsilon_Z^{trigger}$, using a sample of candidate $Z \to \mu^+\mu^-$ events found without requiring a dimuon trigger. Such a sample can be obtained by combining the triggered muon in events passing the single muon trigger with another high P_T track in the event and requiring that the resulting invariant mass is near the Z mass. The number of background events within this sample can be taken into account by fitting a func-

tion to the invariant mass distribution outside the mass window. The ratio of the number of these candidates that also pass the dimuon trigger to the total number of candidates will be equal to the trigger efficiency for a single muon, ε_μ. The dimuon trigger efficiency, $\varepsilon_{\mu\mu}$, will be approximately the square of this number (i.e. $\varepsilon_{\mu\mu} = \varepsilon_\mu^2$), however, angular correlations within the detector will have to be taken into account. This can be done using Monte-Carlo simulation. The uncertainty on such a determination of the trigger efficiency will depend on the size of the candidate sample. With 50,000 candidate events, equivalent to $250pb^{-1}$ of data, the uncertainty will be 0.1%.

4.6.6 Luminosity

The luminosity will be determined accurately at LHCb by either measuring the rate of the rare QED process $pp \to pp + \mu\mu$[59, 60], which will be discussed in the next chapter, or by using the LHCb vertex locator (VELO) to measure the characteristics of beam-gas events near the interaction point[58]. Currently, as we shall see, it is estimated that with $1fb^{-1}(2fb^{-1})$ of data a luminosity measurement can be made at LHCb with an associated uncertainty of 1.9%(1.7%) using the measured rate of the $pp \to pp + \mu\mu$ process[60]. It should be noted that the systematic uncertainty due to this source will only effect the overall normalisation of the differential distributions $d\sigma/dy$ and $d\sigma/dP_T$ but not their shapes. Thus, even if the luminosity can not be determined to this level, a measurement of the Z cross-section at LHCb can still provide constraints on both the proton PDFs and QCD.

4.7 Expected measurement accuracy

4.7.1 Total cross-section measurement

Assuming a central value of 1800pb for $\sigma_Z(4\pi) \cdot Br(Z \to \mu^+\mu^-)$, the efficiencies given in sections 4.3 and 4.5, and the estimated systematic uncertainties given in section 4.6 and summarised in table 4.7, an integrated luminosity of $100pb^{-1}$ would yield the following total (4π) cross-section measurement

$$\sigma_Z(4\pi) \cdot Br(Z \to \mu^+\mu^-) = 1800 \pm 13.8(stat.)^{+42.5}_{-50.8}(syst.) \pm 54(lumi.) \quad pb \tag{4.14}$$

The measurement is already systematics dominated. Here we have assumed that the luminosity can be determined using the beam-gas technique, described in[58], with an associated measurement uncertainty of 3%. The systematic uncertainty is $\sim$2.5% and is mainly due to uncertainties in the PDF set used to make the extrapolation to 4π. With one full year of data taking at LHCb ($2 \times 10^{32} cm^{-2} s^{-1}$) the luminosity uncertainty will fall to about $\sim$1.5%.

Source	Estimated systematic uncertainty (%)	
	Forward measurement	4π measurement
$b\bar{b}$ cross-section	0.1	0.1
Pions	0.2	0.2
Background total	0.22	0.22
Higher order corrections	0	0.08
PDFs	0	$^{+2.34}_{-2.70}$
Detector description	0.1	0.1
P_T resolution	0.05	0.05
Momentum scale	0.15	0.15
Acceptance total	0.19	$^{+2.34}_{-2.70}$
Trigger	0.1	0.1
Tracking	0.1	0.1
Track muon chamber matching	0.1	0.1
Muon identification	0.1	0.1
Efficiency total	0.26	0.26
Non luminosity total	0.39	$^{+2.36}_{-2.82}$
Luminosity	1.92	1.92

Table 4.7: Estimated systematic uncertainties on a total Z cross section measurement and a cross-section measurement within the LHCb acceptance using $1000 pb^{-1}$ of data.

4.7.2 Forward measurement

A much more precise result can be obtained by restricting the cross-section measurement to the forward region ($1.7 < y < 4.9$) where we expect

$$\sigma_Z(1.7 < y < 4.9) \cdot Br(Z \to \mu^+\mu^-) = 482.6 \pm 3.7(stat.) \pm 1.7(syst.) \pm 14.5(lumi.) \quad pb \tag{4.15}$$

Again, with only $100 pb^{-1}$ of data we expect the largest source of uncertainty to come from the luminosity measurement. Combined, the statistical and (non-luminosity) systematic sources contribute $\sim 1\%$ to the overall uncertainty.

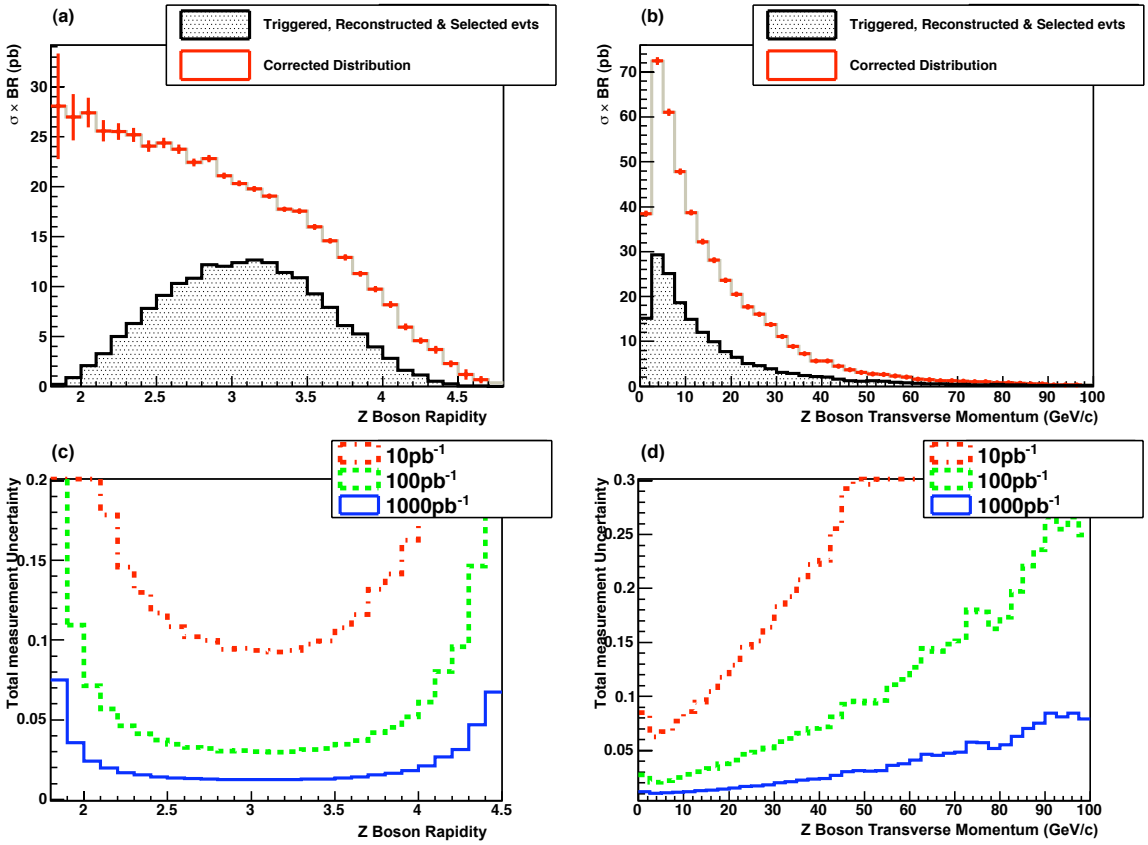

Figure 4.22: (a) and (b) show, respectively, the expected measurements of the differential Z cross-section with respect to Z boson rapidity and transverse momentum at LHCb. The raw (triggered, reconstructed and selected) event rate is in black (solid histogram) while the measured cross-section, which includes the appropriate correction for the experimental efficiency, is in red (points with error bars). Here the errors correspond to a measurement using $100 pb^{-1}$ of data. (c) and (d) show the expected measurement uncertainties (statistical and systematic), using 10, 100 and $1000 pb^{-1}$ of data, as a function of Z boson rapidity and transverse momentum. The uncertainty due to the determination of the absolute luminosity has not been included.

4.7.3 Differential distributions

Figures 4.22(a) and 4.22(b) show, respectively, the measured and corrected Z boson rapidity and transverse momentum distributions for events reconstructed at LHCb ($1.7 < y < 4.9$). Here the filled histograms correspond to events that have been triggered, reconstructed and selected and the points with error bars to the distributions after they have been corrected using the estimated acceptance and efficiency values given in sections 4.3 and 4.5. The error bars shown on the corrected distribution correspond to the expected statistical and systematic uncertainties obtained using $100 pb^{-1}$ of data.

The expected uncertainties on a measurement using 10, 100 and 1000 pb^{-1} of data are shown as a function of both Z boson rapidity and transverse momentum in figures 4.22(c) and 4.22(d)

respectively. Here it is assumed that the non-luminosity sources of systematic uncertainties are flat with respect to the Z rapidity and transverse momentum and contribute an uncertainty of $\pm 0.36\%$ for data samples of 100 and $1000 pb^{-1}$ and $\pm 2.3\%$ for $10 pb^{-1}$ of data. The systematic uncertainty due to the determination of the luminosity has not been included since, for the purposes of providing constraints on the proton PDFs and QCD, we are primarily concerned with the shape of the distributions and not their overall normalisation. With $1000 pb^{-1}$ of data the total uncertainty reaches minimum values ($\sim 1\%$) in the low-P_T region (P_T <25GeV/c) and for Z boson rapidity values in the range $2.5 < y < 4$.

The effects of background contamination and detector resolution have not been included in these distributions. Assuming the backgrounds from pion/kaon mis-identification can be estimated accurately from data the effect of background contamination will be negligible contributing an uncertainty of $\sim 0.1\%$ per bin (see figure 4.18). Although not dealt with here it is envisioned that the effects caused by the detector resolution will be studied before data-taking begins.

4.8 PDF sensitivity

The potential ability of a measurement of the $d\sigma/dy$ distribution at LHCb to constrain the proton PDFs has been investigated using the latest PDF error set from the MSTW group (MSTW2007nlo[26]). Unlike previous PDF sets from this group (MRST2001 etc.) the latest set is parameterised by 20, rather than 15, parameters. Thus the MSTW2007 set includes a best fit PDF set, corresponding to a minimum χ^2 fit of the 20 parameters to a variety of experimental data, and 40 error PDF sets where, as described in section 6.3, a given error PDF set is produced by altering one of the 20 linearly independent eigenvectors, Q_i, by plus or minus 1σ.

The percentage changes, caused by these $\pm 1\sigma$ changes to the eigenvectors, to the $d\sigma/dy$ distribution for Z bosons at the LHC predicted by the best fit PDF set have been examined. A comparison between the variations due to the $\pm 1\sigma$ changes to each of the 20 eigenvectors and the expected uncertainty on a measurement of the $d\sigma/dy$ distribution at LHCb is shown in figure 4.23. Here the dashed black line corresponds to a $+1\sigma$ change and the solid red line to a -1σ change while the measurement uncertainties using 100 or $1000 pb^{-1}$ are given by the dashed green line and solid blue line respectively. Examining figure 4.23 we can conclude that measurements of the $d\sigma/dy$ distribution at LHCb will be sensitive to different eigenvectors, and thus different physical parameters, than the corresponding measurements at the central LHC experiments, ATLAS and CMS, which will cover the range $|y| < 2.6$. This is unsurprising since, as noted in section 4.2, Z production at LHCb occurs in a different region of $x - Q^2$ phase space than Z production at ATLAS and CMS.

In addition to examining the uncertainty attributable to each eigenvector we have investigated the overall uncertainty associated with the latest MSTW fit. The overall uncertainty can be computed by combining, in quadrature, the changes to the $d\sigma/dy$ distribution caused by the $\pm 1\sigma$ alterations to each eigenvector. In most instances the two percentage changes to the

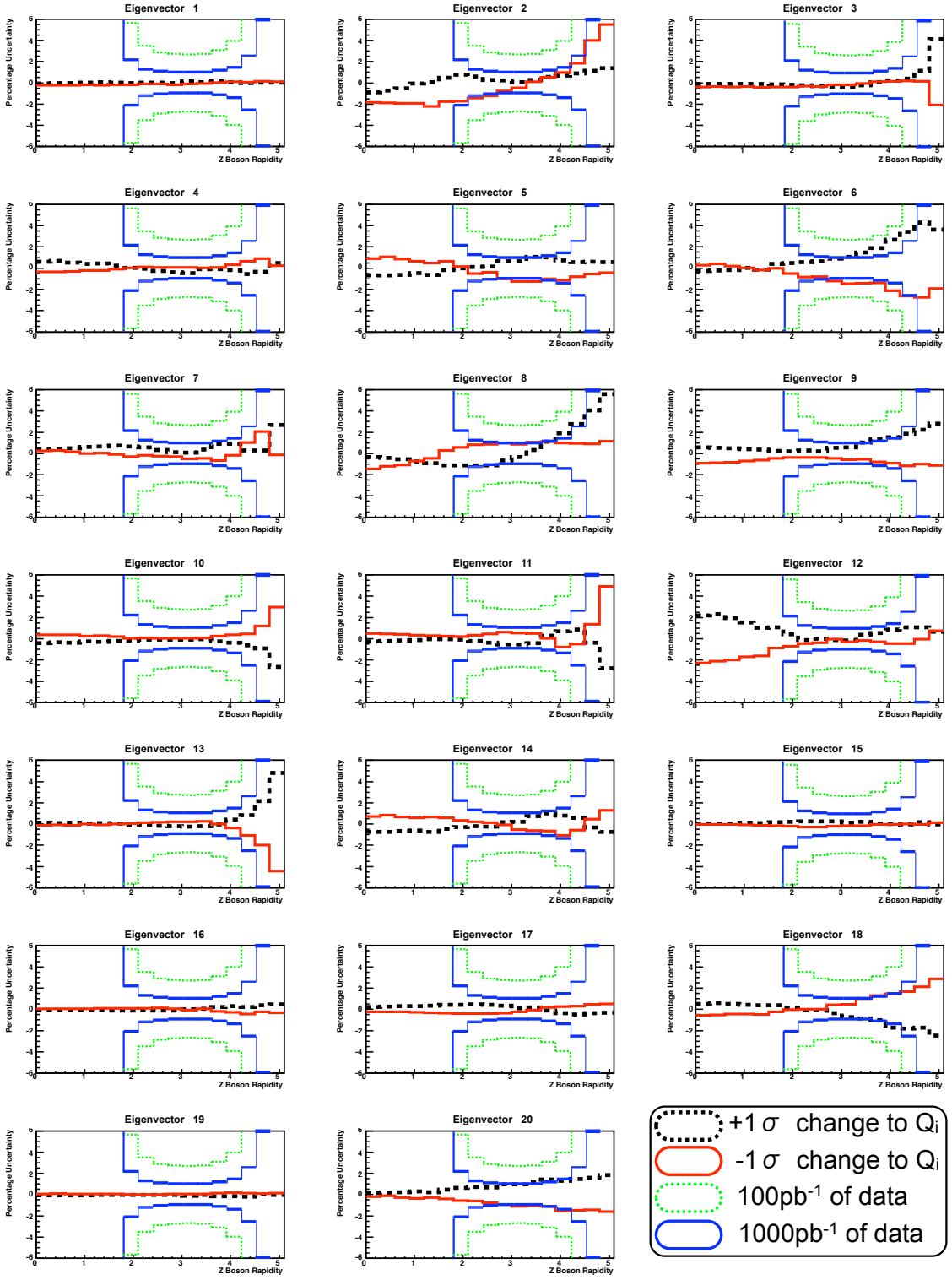

Figure 4.23: Percentage PDF uncertainty as a function of Z boson rapidity for the 20 eigenvectors, Q_i, of the new MSTW2007NLO PDF set. The $+1\sigma$ and -1σ variations of the 20 eigenvectors are shown in black and red respectively. The total uncertainties expected on a measurement at LHCb using $100pb^{-1}$ and $1000pb^{-1}$ of data are shown.

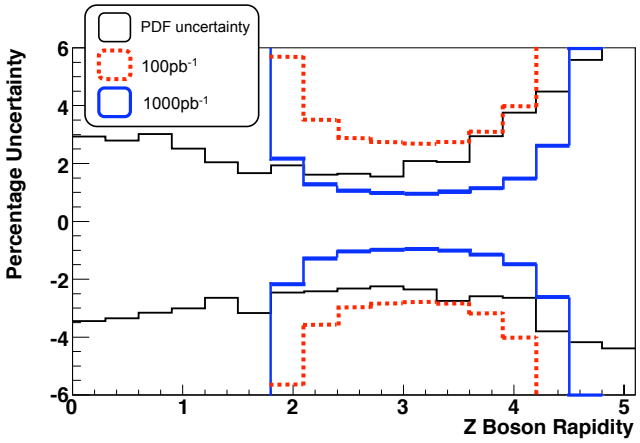

Figure 4.24: The overall percentage PDF uncertainty as a function of Z boson rapidity, determined using the MTSW2007nlo error PDF sets. The total uncertainties expected on a measurement at LHCb using $100pb^{-1}$ and $1000pb^{-1}$ of data are shown.

$d\sigma/dy$ distributions lie in opposite directions. In this case one of the changes will contribute to the overall positive uncertainty while the other will contribute to the negative uncertainty. However, in a small number of cases both changes lie in the same direction and a different procedure must be followed: in the case where both changes are negative(positive) the contribution to the overall negative(positive) uncertainty is equal to both changes summed in quadrature while the positive(negative) contribution is zero. Figure 4.24 shows the overall PDF uncertainty on the $d\sigma/dy$ distribution, computed in this manner, and the expected experimental uncertainties on a measurement at LHCb using 100 or $1000pb^{-1}$ of data. The overall PDF uncertainty, represented by the solid black line, being $\sim$3% at y=0 reaches a minimum of $\sim$2% in the centre of the LHCb detector before increasing to $\sim$5% at large rapidities. From figure 4.24 we can conclude that, with as little as $100pb^{-1}$ of data, measurements of the Z cross-section at LHCb can begin to constrain the proton PDFs while with $1000pb^{-1}$ significant improvements to our understanding of the PDFs at LHC energies can be made.

4.9 Conclusions

A high rate of $Z \to \mu^+\mu^-$ events will be recorded and reconstructed at LHCb. A set of simple offline selection criteria has been proposed that will reduce the background to a low level that will be dominated by the combinatoric backgrounds due to pion and kaon mis-identification. It is expected that these backgrounds can be well understood from real data. With $100pb^{-1}$ of data and ignoring luminosity uncertainties, the Z cross-section can be measured in the forward region with a $\sim$1% precision which is mainly attributable to systematic uncertainties coming from a number of sources (tracking, muon id, track matching). Comparisons to measurements made by ATLAS and CMS can be made by either examining the overlap region ($1.7 < y < 2.6$) in the distribution $d\sigma/dy$ or extrapolating to a total (4π) cross-section measurement. For a 4π

measurement the systematic uncertainty will rise to $\sim$2.5% due to the theoretical uncertainties on the proton PDFs. Assuming the luminosity can be determined, LHCb will rapidly be able to make a unique measurement of $\sigma_Z \cdot Br(Z \to \mu^+\mu^-)$ at high rapidities while providing an important cross-check for the corresponding measurements at the central LHC detectors, CMS and ATLAS. This measurement will constrain the proton parton distribution functions via the $d\sigma/dy$ distribution and, in conjunction with a measuement of the W cross section, precisely test the electroweak sector at LHC energies.

5 Luminosity measurements at LHCb using $pp \rightarrow p + \mu^+\mu^- + p$ events

As was seen in chapter 4, a determination of the absolute luminosity is required in order to measure the Z boson production cross-section. This chapter outlines the feasibility of using the elastic two photon process $pp \rightarrow p + \mu^+\mu^- + p$ to make luminosity measurements at LHCb.

5.1 Introduction

The measurement of a cross-section, σ, within a fiducial volume v is given by $\sigma(v) = N/(\varepsilon\mathcal{L})$ where N is the number of events observed, ε is the efficiency for recording and reconstructing those events and $\mathcal{L}$ is the integrated luminosity.Knowledge of the integrated luminosity is therefore required to make any cross-section measurement. In general there are three methods for determining the absolute luminosity at a colliding beam experiment:

1. A simultaneous measurement of a pair of cross-sections that are connected with each other quadratically via the optical theorem. A well known example of this is the measurement of the total inelastic cross-section and the elastic cross-section at very high pseudorapidities $|\eta| \simeq 9$ (see for example[80]). While such a measurement will be made at the central general purpose LHC detectors, ATLAS and CMS, which have dedicated forward detectors for this purpose, it is not a viable technique at LHCb as the detector instrumentation only extends to $\eta = 4.9$.
2. Direct measurement of the beam currents and shapes. While the beam currents can be accurately determined using beam transformers, the beam profiles are more difficult to determine directly and usually constitute the dominant source of uncertainty on a luminosity measurement using this technique. There are a number of methods for determining the beam profile, for example the Van Der Meer scan method[81] where the colliding beams are moved transversely across each other and the wire scan method[82] where the profiles are measured by passing wires through the beams. Luminosity measurements at the LHC experiments based on these techniques are expected to have associated uncertainties of $\sim 10\%$. A recently proposed method[58] for determining the beam profiles at colliding beam experiments utilises the precision vertex detectors found at modern HEP experiments to reconstruct beam gas interactions near the beams' crossing point. This method, which will be implemented at LHCb, is expected to result in a luminosity measurement with an associated uncertainty of $\sim 3-5\%$.

3. The final way to measure the luminosity is to record the event rate of a process with a cross-section that can be accurately calculated from theory. The accuracy of a luminosity measurement using this method is usually limited by the theoretical uncertainty on the calculated cross-section. Two candidate processes have been identified for such a measurement at LHCb: $W^{\pm}$ and Z production which has been investigated previously [61, 63, 83] (also see chapter 4) and which is expected to yield a luminosity measurement with a $\sim$4% uncertainty due to uncertainties in our understanding of the proton Parton Distribution Functions (PDFs); and elastic $\mu^+\mu^-$ pair production via two-photon fusion, $pp \to p + \mu^+\mu^- + p$, which has a cross-section which is better known with a theoretical uncertainty of $< 1\%$ but has a much lower event rate. This chapter builds on the work of A. Shamov and V. Telnov[59] and outlines the progress that has been made towards making a luminosity measurement at LHCb using the event rate of this second process.

Knowing the cross-section for elastic $\mu^+\mu^-$ pair production via two-photon fusion, $\sigma_{el}(v)$, within some fiducial volume v, the absolute luminosity for a given data-set at LHCb can be calculated from

$$\int \mathcal{L}dt = \frac{N_{el}^{obs} - N_{el}^{back}}{\varepsilon_{el}^{total} \cdot \sigma_{el}(v)} \tag{5.1}$$

Where N_{el}^{obs} is the number of observed $pp \to p + \mu^+\mu^- + p$ candidate events, N_{el}^{back} is the expected number of background events and ε_{el}^{total} is the total efficiency at LHCb for recording $pp \to p + \mu^+\mu^- + p$ events produced within the volume v. The total efficiency can be expressed as the product

$$\varepsilon_{el}^{total} = A_{el}^{geom} \times A_{el}^{kin} \times \varepsilon_{el}^{trigger} \times \varepsilon_{el}^{reco} \tag{5.2}$$

where A_{el}^{geom} and A_{el}^{kin} are the acceptances due to the detector topology and offline kinematic selection criteria respectively, while $\varepsilon_{el}^{trigger}$ and ε_{el}^{reco} are the trigger and reconstruction efficiencies.

This chapter presents Monte-Carlo based estimates of the acceptances, efficiencies and level of background for the $pp \to p + \mu^+\mu^- + p$ channel at LHCb and is organised as follows: section 5.2 briefly reviews dimuon production via two photon fusion and discusses the uncertainty on cross-section predictions for this process; section 5.3 outlines the event characteristics and experimental efficiency of $pp \to p + \mu^+\mu^- + p$ events at LHCb and, additionally, outlines a new L0 dimuon trigger stream designed to improve the trigger efficiency for these events; section 5.4 describes the various background processes; in section 5.5 a set of offline selection cuts are proposed and their effects on both the signal and background events are described; section 5.6 discusses a possible method that will enable the effects of multiple interaction bunch crossings to be determined; finally, section 5.7 gives the expected systematic and statistical uncertainties on the proposed luminosity measurement.

5.2 Accuracy of predicted cross-section

This section provides a brief review of dimuon production via two-photon fusion and discusses the accuracy of current cross-section predictions for this process. For more complete discussions see[59],[84] and[65].

5.2.1 Elastic $\mu^+\mu^-$ production via photon fusion

Within the Equivalent Photon Approximation (EPA) the two-photon muon pair production cross-section at the LHC can be calculated as a convolution of the direct cross-section of two colliding photons that produce a muon pair and the fluxes of virtual photons, dn_1 and dn_2, surrounding the two colliding protons

$$d\sigma = \sigma_{\gamma\gamma\to\mu^+\mu^-} dn_1 dn_2 \tag{5.3}$$

For low Q^2 elastic events where the impact parameter of the colliding protons is large the protons behave as point-like particles and the virtual photon fluxes, dn_1 and dn_2, will be equal to

$$dn_{QED} = \frac{\alpha}{\pi}\frac{d\omega}{\omega}\frac{dq^2}{q^2}\left(1 - \frac{q^2_{min}}{q^2}\right) = \frac{\alpha}{\pi}\frac{d\omega}{\omega}\frac{\vec{q}_T^{\,2} d\vec{q}_T^{\,2}}{(\omega^2/\gamma^2 + \vec{q}_T^{\,2})^2} \qquad \text{[59]} \tag{5.4}$$

where $q(\omega, \vec{q})$ is the four-momentum of the photon, $\gamma = E/m_p$ is the Lorentz factor of the colliding proton, m_p is the mass of the proton and α is the fine structure constant. Here the process is only sensitive to the proton mass and charge which are known very accurately with measurement uncertainties below 0.001%. However, for higher Q^2 events the impact parameters are smaller and the process is sensitive to the proton's electric and magnetic form factors G_E and G_M and the virtual photon fluxes are given by

$$dn_{elastic} = dn_{QED}\frac{G_E^2 - q^2/(2m_p G_M)^2}{1 - (q/2m_p)^2} \tag{5.5}$$

The predicted cross-section for elastic collisions of the type illustrated in figure 5.1(a) will have contributions from both the point-like process and the process that is sensitive to the electromagnetic form factors. Using the LPAIR generator[85], we have determined that the mean Q^2 of these two photon events is $< Q^2 >= 0.001 GeV^2$. For such low Q^2 events the appropriate electromagnetic form factor measurements have been made by J. J. Murphy et. al. [86] and can be parameterised by

$$G_E = 1 - bQ^2 \tag{5.6}$$

where $b = (0.110 \pm 0.007)[fm]^2 = (2.83 \pm 0.18) GeV^{-2}$. The uncertainty on the predicted cross-section due to the electomagnetic form factor measurements will therefore be of the order $4\Delta b < Q^2 >= 0.065\%$.

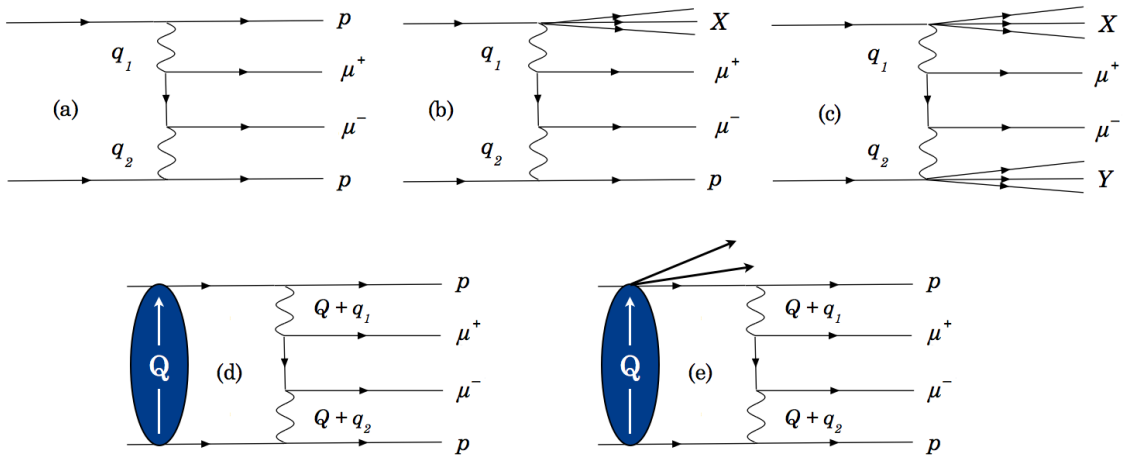

Figure 5.1: Feyman diagrams showing $\mu^+\mu^-$ production via two-photon fusion. (a) elastic case, (b) semi-inelastic case, (c) fully-inelastic case, (d) elastic case showing a possible rescattering correction where the colliding protons interact via the strong interaction and the energy of the protons is altered, (e) a rescattering correction where the colliding protons interact via the strong interaction and additional particles are produced.

5.2.2 Inelastic $\mu^+\mu^-$ production via photon fusion

For dimuons produced via photon fusion where one or both of the colliding protons dissociate during the collision process we have for each inelastic vertex a virtual photon flux of the form

$$dn_{inelastic} = dn_{QED}\frac{W_2(q^2,M^2)}{2m_p}dM^2 \approx dn_{QED}\frac{|q^2|}{4\pi^2\alpha}\frac{\sigma_T^{\gamma p}+\sigma_S^{\gamma p}}{M^2-m_p^2}dM^2 \qquad [59] \qquad (5.7)$$

Here: $W_2(q^2,M^2)$ is the inelastic scattering structure function, M is the invariant mass of the hadronic system produced in the dissociation, and $\sigma_T^{\gamma p}$ and $\sigma_S^{\gamma p}$ are the γp cross-sections for transversely polarised and scalar interactions respectively. Feyman diagrams for events where one proton dissociates and for events where both protons dissociate, from now on refered to as semi-inelastic and fully-inelastic events respectively, are shown in figures 5.1(b) and 5.1(c). Due to uncertainties in the momentum distributions of the quarks within the proton and the collective excitations of these quarks the matrix element describing inelastic vertices is not as well known as the matrix element for elastic vertices. This results in much higher uncertainties in the predicted cross-section for inelastic dimuon production via photon fusion. For the purposes of a luminosity measurement it is therefore not advantageous to include such events. In the subsequent sections of this chapter it is shown that the inelastic contribution can be suppressed using offline kinematic cuts.

5.2.3 Rescattering corrections

In addition to the inelastic processes shown in figures 5.1(b) and 5.1(c), which take into account the strong interaction *within* the colliding protons, any strong interactions *between* the colliding protons must also be accounted for. In these so-called rescattering processes the strong interaction is not mediated by a point-like object and can be viewed as a pomeron exhange between the protons. Figures 5.1(d) and 5.1(e) show schematic representations of such processes for the elastic case where only the energy of the proton is affected and where additional particles are produced during the interaction respectively. It has been shown by Khoze et. al. [65] that for a $\mu\mu$ pair produced with a mass of $20GeV/c^2$ at a rapidity of zero and having a dimuon transverse momentum below 50MeV/c, the (negative) correction caused by the process shown in figure 5.1(d) gives a contribution of $<0.4\%$. In addition, since at LHCb the final forward protons are not detected, a positive correction must be made to take into account events of the type shown in figure 5.1(e) where the photon interacts coherently with the whole system produced in the course of the proton's diffractive dissociation - in other words where the photon interacts with the proton excitation in the proton-pomeron vertex. It is currently estimated that this positive contribution has a magnitude of the order of 0.1%[1]. Finally, taking both the positive and negative corrections into account an overall correction due to these rescattering effects of 0.3% is expected. It was also shown in[65] that, unlike the purely QED elastic events described in section 5.2.1, events containing these rescattering effects do not result in a sharp peak at $\phi_{\mu\mu} = 0$ in the dimuon acoplanarity [2] distribution. Therefore, in conclusion, by selecting events with $P_T^{\mu\mu}$ <50MeV/c the uncertainty on the predicted cross-section for dimuons produced via elastic two photon fusion can be reduced to about 0.3% and, additionally, by examining the acoplanarity values of the produced dimuons the rescattering corrections can be estimated.

5.3 Signal events

A Monte Carlo sample of 1×10^5 $pp \to p + \mu^+\mu^- + p$ events was used in this analysis. These events were generated with a version of the LPAIR[3][85] event generator, which performs a full Leading Order (LO) matrix element calculation, and the detector effects were simulated using the detector geometry described by Dbase v22r4 and Gauss v15r21. The detector digitization was performed by Boole v6r5 and event reconstruction by Brunel v24r6. To speed up the generation process each muon in the generated events were required to have

1. Pseudorapidities in the range $1.6 < \eta < 5$
2. A transverse momentum of $P_T > 0.9GeV/c$

[1] It should be noted that at the time of writing these contributions are the subject of current theoretical investigation. The quoted value of 0.1% may therefore change in the near future.

[2] Here we define the dimuon acoplanarity by $\phi_{\mu\mu} = \pi - cos^{-1}((P_x^+ P_x^- + P_y^+ P_y^-)/(P_T^+ P_T^-))$ where the superscripts, + and -, refer to the μ^+ and μ^- respectively.

[3] The author is most grateful to Andrey Shamov and Valery Telnov for providing a copy of their modified version of the LPAIR generator.

3. A momentum of $P > 7.5 GeV/c$

Within the fiducial volume, v, defined by these production cuts LPAIR predicts a cross-section of $\sigma_{el}(v) = (88.77 \pm 0.32) pb$. The analysis of these events outlined in this chapter has been performed using the LHCb analysis package DaVinci v12r14.

5.3.1 Signal event characteristics

The experimental signature of elastic $\mu^+\mu^-$ pairs produced via two-photon fusion is very distinctive. These events will contain a $\mu^+\mu^-$ pair produced back to back in the transverse plane, thus having small acoplanarity values peaked at zero, and no other particles. In addition the muon pair will have: an invariant mass, $M_{\mu^+\mu^-}$, that will be peaked towards zero and will fall off for higher mass values, and a pair transverse momentum, $P_T^{\mu\mu}$, that also peaks at low values and falls off exponentially for higher transverse momentum values. The particle multiplicity, dimuon invariant mass, pair transverse momentum and acoplanarity distributions for $pp \to p + \mu^+\mu^- + p$ events that pass the L0 and L1 triggers and are reconstructed are shown in figure 5.2.

5.3.2 Geometric acceptance

The geometric acceptance, A_{el}^{geom}, is defined to be the fraction of events satisfying the generator level production cuts (1-3) that contain two muons that are reconstructable as long tracks at Monte-Carlo truth level. Using the sample of 1×10^5 fully simulated $pp \to p + \mu^+\mu^- + p$ events and the DaVinci analysis package we have determined A_{el}^{geom} to be $0.9207 \pm 0.0009(stat.)$.

5.3.3 Efficiencies

The reconstruction efficiency, ε_{el}^{reco}, and trigger efficiency, $\varepsilon_{el}^{trigger}$, will be determined from data once they arrive. However, this section presents estimates of these efficiencies that were obtained using the full LHCb detector simulation. A proposed new dimuon stream at the L0 trigger level that has been used in this analysis and that will allow $pp \to p + \mu^+\mu^- + p$ events to be recorded at LHCb is also outlined.

Reconstruction efficiency

The reconstruction efficiency, ε_{el}^{reco}, is defined to be the fraction of events within the LHCb geometric acceptance that can be reconstructed offline. It can be expressed as the product of three components:

$$\varepsilon_{el}^{reco} = (\varepsilon_{trk}^{(1)} \times \varepsilon_{match}^{(1)} \times \varepsilon_{id}^{(1)}) \times (\varepsilon_{trk}^{(2)} \times \varepsilon_{match}^{(2)} \times \varepsilon_{id}^{(2)}) \tag{5.8}$$

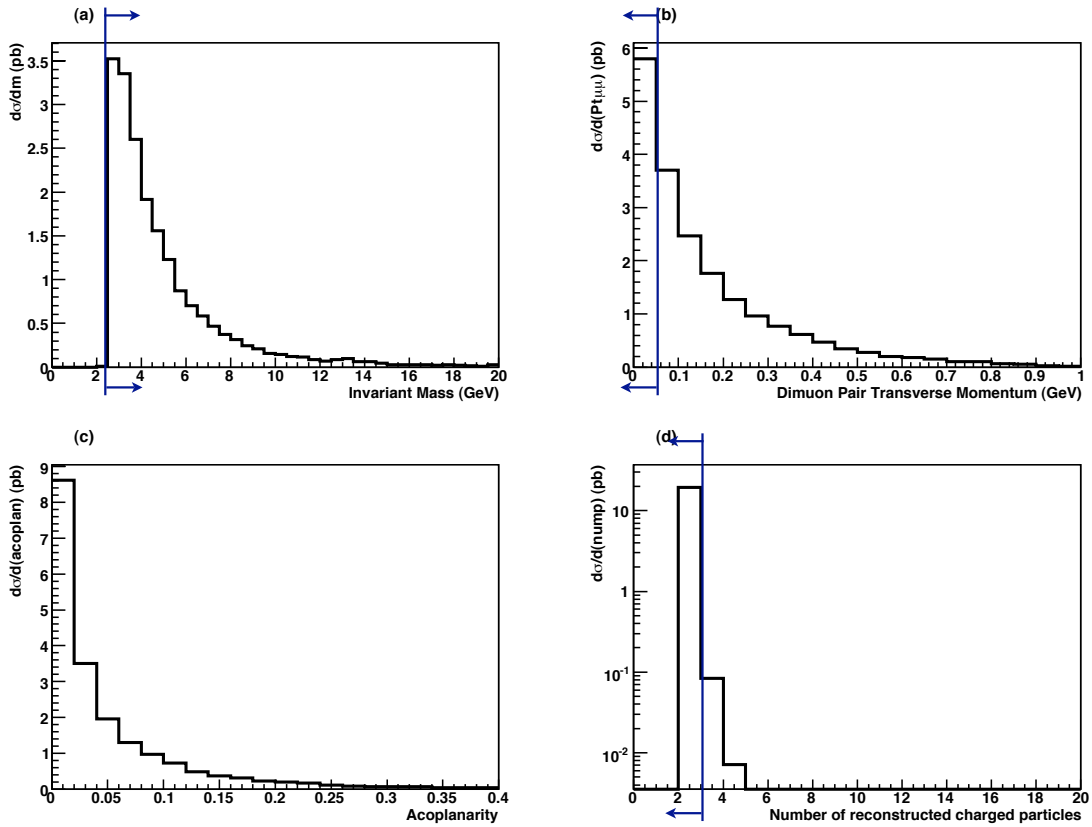

Figure 5.2: Event characteristics of fully simulated and triggered events containing dimuon pairs produced via elastic two-photon fusion. (a) Dimuon invariant mass. (b) Dimuon pair transverse momentum. (c) Dimuon acoplanarity. (d) Event particle multiplicity. The offline kinematic cuts described in section 5 are highlighted.

Here ε_{trk} is the efficiency of reconstructing the track of one of the muons coming from the elastic two-photon fusion process. ε_{match} accounts for the efficiency of reconstructing hits in the muon chambers and matching them to this track. Finally, for tracks that have been matched to the required number of muon hits, ε_{id} is the efficiency of any additional muon identification criteria, e.g. calorimeter energy requirements, that will be used to increase the purity of the muon samples. The superscripts refer to muon 1 and muon 2. Possible methods for determining ε_{trk}, ε_{match} and ε_{id} from data and the expected associated measurement uncertainties are discussed in section 5.7. From simulation ε_{el}^{reco} has been determined to be $0.635 \pm 0.002(stat.)$.

Proposed modification to the L0 trigger

In its current implementation (up to and including DaVinci v19r8) for an event to pass the L0 "dimuon" trigger level it is required that

1. The sum of transverse momenta of all the muons in the event, $\sum P_T^{\mu}$, must be greater than or equal to 1.5GeV/c.
2. A total global transverse energy, E_T, from the electromagnetic and hadronic calorimeters is 5GeV or more.

It should be noted that the first condition makes no requirement on the number of muons reconstructed by the L0 trigger system and an event containing only one muon with $P_T > 1.5GeV/c$ can be passed by this stream. The second requirement is designed to guard against muons from the beam halo consuming a large amount of the bandwidth. Since $pp \rightarrow p + \mu^+\mu^- + p$ events only contain two muons and no other particles they will only rarely result in an E_T satisfying the second requirement and thus practically none of our signal events pass the L0 trigger. Consequently we propose to introduce a new dimuon line at the L0 level that will allow $pp \rightarrow p + \mu^+\mu^- + p$ events to pass while at the same time keeping the bandwidth consumed by halo muons to a low level. The new stream has the following two requirements

1. The sum of transverse momenta of all the muons in the event, $\sum P_T^{\mu}$, must be greater than or equal to 1.5GeV/c.
2. The L0 trigger system must reconstruct more than one muon.

Preliminary investigations of this new dimuon trigger stream suggest that it will allow beam halo events to pass at a rate of $\sim 200Hz$ which constitutes 0.02% of the total L0 accept rate [88].

Having more than one trigger stream at the L0 level that passes $pp \rightarrow p + \mu^+\mu^- + p$ events would be useful for determining the L0 efficiency for these events. It is currently envisioned that there will be a random trigger stream at both the L0 and HLT levels, however, given the extremely small cross-section for $pp \rightarrow p + \mu^+\mu^- + p$ events at LHCb this stream will be of limited use for such a purpose. An alternative way of triggering these events at L0 might be to require low activity in the event and an SPD multiplicity of 2. This possibility should be investigated in the future.

Trigger efficiencies

Due to the fact that the Higher Level Trigger (HLT) is under development it has not been included in our efficiency studies. Instead the old L1 trigger level has been used as a substitute. The HLT will be investigated for the $pp \rightarrow p + \mu^+\mu^- + p$ channel in the future before data taking begins. The total trigger efficiency is defined from the combination of the conditional probabilities that an event passes each trigger stage.

$$\varepsilon_{el}^{trigger} = \varepsilon_{el}^{L0} \times \varepsilon_{el}^{L1} \tag{5.9}$$

Here ε_{el}^{L0} is the fraction of events that can be reconstructed offline that would pass the L0 trigger algorithm which includes the new dimuon stream outlined in the previous section, ε_{el}^{L1} is the fraction of events that can be reconstructed offline and pass the L0 trigger that also pass the L1 trigger algorithm. Table 5.1 summarises the acceptances and efficiencies for

Stage	Symbol	Efficiency
Detector acceptance	A_{el}^{geom}	0.9207 ± 0.0009
Reconstruction	ε_{el}^{reco}	0.5351 ± 0.0016
L0 algorithm	ε_{el}^{L0}	0.6190 ± 0.0022
L1 algorithm	ε_{el}^{L1}	0.7135 ± 0.0026
Kinematic acceptance	A_{el}^{kin}	0.2697 ± 0.0030
Total efficiency	ε_{el}^{total}	0.0587 ± 0.0008

Table 5.1: Acceptance, reconstruction and trigger efficiencies at LHCb for $pp \to p + \mu^+\mu^- + p$ events that pass the generator cuts defined in section 5.3. Statistical errors are shown.

$pp \to p + \mu^+\mu^- + p$ events at LHCb. The calculation of the acceptance due to our offline kinematic selection criteria, A_{el}^{kin}, is discussed in section 5.5.

5.4 Background processes

The strongest backgrounds to our signal are events containing dimuon pairs produced via inelastic two-photon fusion and double pomeron exchange. These processes have been studied by interfacing the LPAIR and DPEMC Monte-Carlo generators to the full LHCb detector simulation. In addition a number of other Standard Model processes such as $b \to \mu^- + Y$, $\bar{b} \to \mu^+ + X$ and events where two hadrons are both mis-identified as muons have been considered. These backgrounds have been investigated at four vector level by examining large Monte-Carlo samples generated using the PYTHIA and DPEMC generators. The background samples that have been studied are summarised in table 5.4 and are described in the following sections.

5.4.1 Dimuon pairs produced via inelastic two-photon fusion

Monte-Carlo samples of 2.5×10^4 and 1×10^4 events have been generated and analysed for the semi-inelastic and fully-inelastic two-photon fusion processes respectively. These events were produced with the LPAIR generator using the soft proton structure functions of A. Suri and D. Yennie[89]. The LHCb detector effects were simulated using the detector geometry described by Dbase v22r4 and Gauss v15r21. The detector digitization was performed by Boole v6r5 and event reconstruction by Brunel v24r6. To speed up the generation process both muons in the generated events were required to satisfy the production cuts (1-3) described in section 5.3.

Background process	$\sigma \times BR$ (pb)	Events generated	$\int \mathcal{L}dt$ equivalent
Studied with full LHCb simulation			
$pp \to p + \mu^+\mu^- + X$ ($\gamma\gamma$)	42.52	$25K$	$588 pb^{-1}$
$pp \to Y + \mu^+\mu^- + X$ ($\gamma\gamma$)	28.01	$10K$	$357 pb^{-1}$
$pp \to Y + \mu^+\mu^- + X$ (DPE)	112.68	$25K$	$222 pb^{-1}$
Studied at 4 vector level			
$b \to \mu^- + Y$, $\bar{b} \to \mu^+ + X$	5×10^6	$50M$	$10 pb^{-1}$
$c \to \mu^- + Y$, $\bar{c} \to \mu^+ + X$	3.5×10^7	$350M$	$10 pb^{-1}$
$\gamma^*/Z \to \mu^+\mu^-$	2×10^4	$10M$	$500 pb^{-1}$
$J/\psi \to \mu^+\mu^-$	4.63×10^6	$46.3M$	$10 pb^{-1}$

Table 5.2: Standard Model background samples that have been used in this analysis. The two-photon fusion ($\gamma\gamma$) and double pomeron exchange (DPE) samples were produced with the LHCb detector simulation software chain (Gauss, Boole and Brunel) and the LPAIR and DPEMC Monte-Carlo event generators respectively. The samples that have been studied at 4 vector level were produced using the PYTHIA Monte-Carlo generator

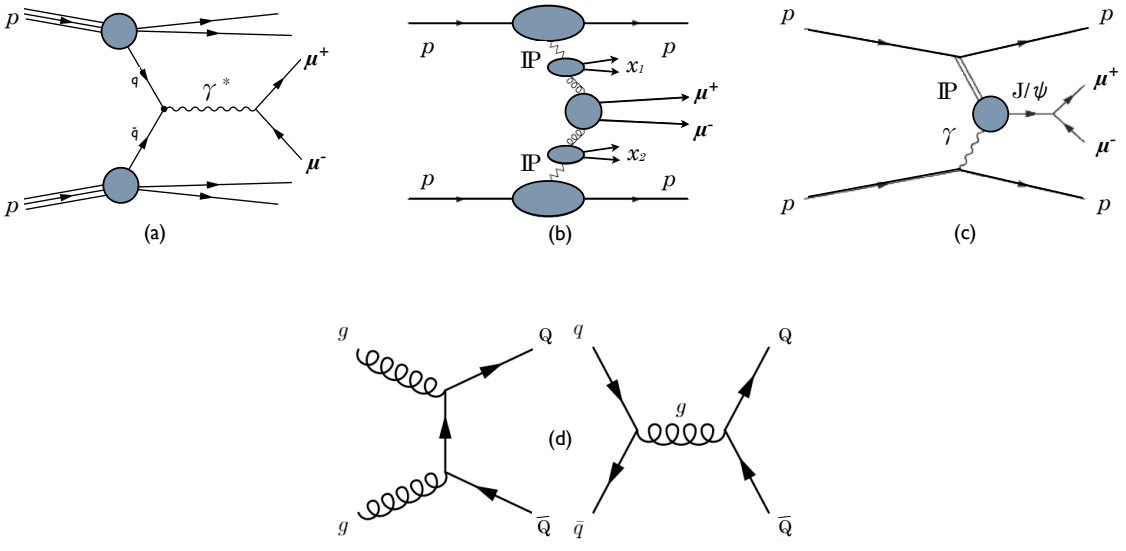

Figure 5.3: Feyman diagrams showing a variety of background processes. (a) dimuon production via the Drell-Yan process, (b) dimuon production via double pomeron exchange, (c) dimuon production from photon-pomeron interactions - in this case mediated by J/ψ, (d) the leading order modes for heavy quark production, gluon fusion on the left and quark anti-quark annihilation on the right.

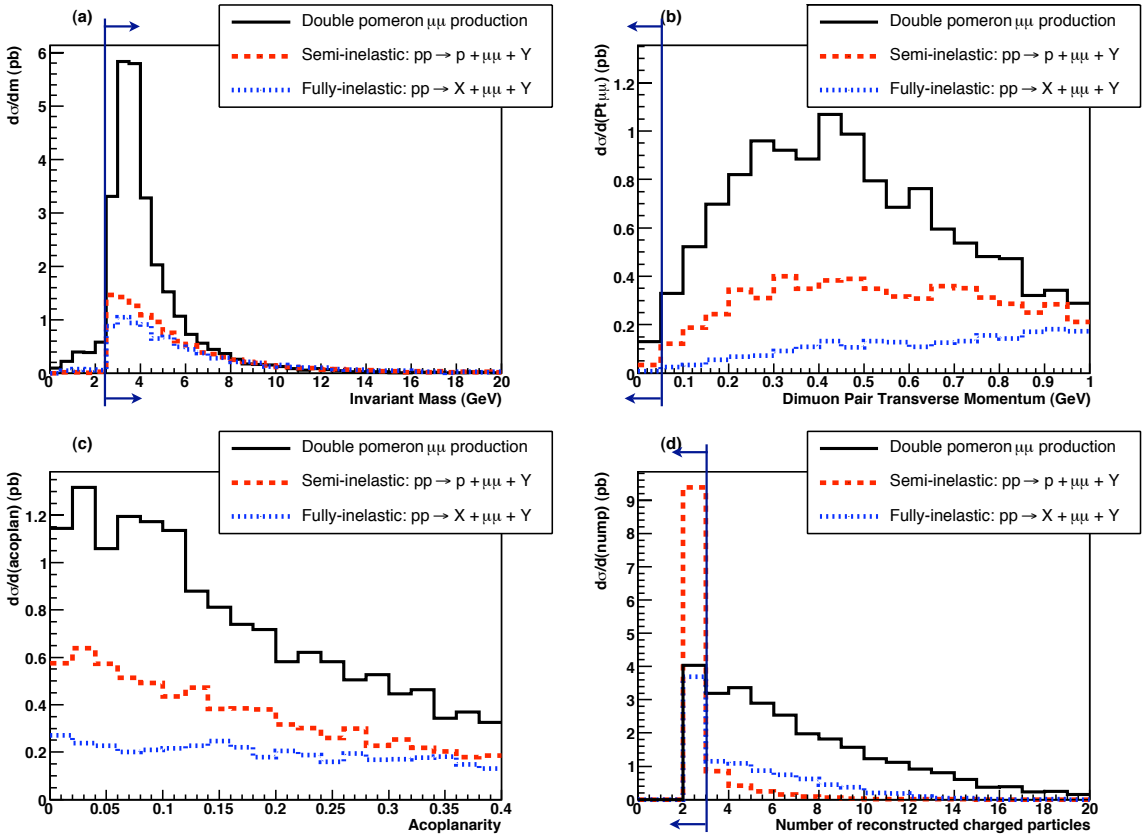

Figure 5.4: Fully simulated and triggered events that contain a $\mu^+\mu^-$ pair produced via double pomeron exchange or inelastic two photon fusion. (a) Dimuon invariant mass. (b) Dimuon pair transverse momentum. (c) Dimuon acoplanarity. (d) Event particle multiplicity. The offline kinematic cuts described in section 5 are highlighted.

Figure 5.4 shows the dimuon invariant mass, pair transverse momentum, acoplanarity and particle multiplicity distributions for events within these samples that are fully reconstructed and that pass the L0 and L1 trigger levels. By comparing these four distributions with the corresponding elastic distributions shown in figure 5.2 it can be seen that for dimuons produced via inelastic two-photon fusion: the invariant mass distributions are very similar to the distribution for elastic events; the acoplanarity distributions are relatively flat compared to the corresponding distributions for the elastic events; the dimuon pair transverse momentum distributions peak at higher values ($\sim 600 MeV/c$ for semi-inelastic events and $1100 MeV/c$ for fully-inelastic events) than for elastic events; the particle multiplicity distributions have larger tails than our signal events.

5.4.2 Dimuon pairs produced via double pomeron exchange

A sample of 2.5×10^4 dimuon events produced via double pomeron exchange have been examined. Figure 5.3(b) shows the Feynman diagram for this process. These events were gener-

	H194l	H194nl	H194nlEx	ZEUSnl	H1nl	ZEUS+H1nl
BPR	13.03	23.41	112.68	570.84	73.02	84.52
CF	3.14	3.30	7.42	5.76	5.63	5.19

Table 5.3: Cross-section predictions, in picobarns, for dimuon events produced via double pomeron exchange due to the Boonekamp, Peschanski and Royon (BPR) and Cox-Forshaw (CF) models using the six different Pomeron PDF sets described in the text.

ated with the DPEMC[90] event generator. Within DPEMC these dimuons are produced via the Drell-Yan process within the pomeron-pomeron collision. Since DPEMC applies a cut of $q^2 > 1GeV^2$ to the initial state parton showers of such processes and the events that we are interested in typically have values less than this, only the P_T of the pomeron system and not the P_T of the colliding quarks relative to the parent pomerons will contribute to the dimuon pair P_T [4]. To correct for this a gaussian of width 350MeV/c has been added to the P_T of the partons partaking in the initial state shower, a value that is consistent with previous theoretical studies [91]. The effects of the LHCb detector have been simulated using the geometry described by Dbase v22r4 and Gauss v15r21. The detector digitization was performed by Boole v6r5 and event reconstruction by Brunel v24r6. To speed up the generation process only events containing a dimuon pair with individual pseudorapidities in the range $1.7 < \eta < 5.1$ and a mass above 2GeV/c^2 have been generated.

The cross-section for these events at the LHC has been calculated using two different theoretical models, the inclusive double pomeron exchange model of Boonekamp, Peschanski and Royon (BPR)[92] and the factorized model of Cox and Forshaw[93]. In addition, the uncertainty due to uncertainties in our knowledge of the Pomeron parton distribution functions has been estimated using six different sets of Pomeron PDFs based on data collected at the HERA e-p collider. The PDF sets considered are: the leading order (LO) and next to leading order (NLO) fits to data collected by the H1 experiment in 1994[94] and a more recent extended NLO fit to the same data[95] (labeled respectively H194l, H194nl and H194nlEx in table 5.3); the NLO fits to ZEUS and H1 data collected between 1997-2000 and a fit to the combined data-set from both experiments[96] (labeled respectively ZEUSnl, H1nl and ZEUS+H1nl in table 5.3). Table 5.3 summarises the twelve cross-sections predictions using the BPR and CF models and the six Pomeron PDF sets. While the predictions using the CF model vary between $3-7pb$, suggesting an associated PDF uncertainty of $\sim 50\%$, the BPR predictions are about an order of magnitude larger and vary to a greater degree depending on the Pomeron PDF set choice. We have taken the cross-section to be $113pb$ and have conservatively assigned an uncertainty due to the theoretical modelling and knowledge of the Pomeron flux and PDFs to be $\pm 113pb$.

The dimuon mass, pair tranverse momentum, acoplanarity and particle multiplicity distributions for events within this sample that pass the L0 and L1 trigger levels and are then recon-

[4] The author is most grateful to Andrey Shamov for bringing this point to his attention.

structed are shown in figure 5.4. With the exception of the particle multiplicity distribution, which is flatter and extends up to high values, the distributions for these events have shapes that are similar to those for dimuons produced via semi-inelastic two photon fusion.

5.4.3 Other Standard Model backgrounds

In addition to these backgrounds, the contamination due to four other Standard Model processes - dimuons produced via the Drell-Yan process $\gamma^*/Z \to \mu^+\mu^-$, $b\bar{b}$ events where both b quarks decay semi-leptonically to muons $b \to \mu^- + Y$, $\bar{b} \to \mu^+ + X$, $c\bar{c}$ events where both c quarks decay semi-leptonically to muons $c \to \mu^- + Y$, $\bar{c} \to \mu^+ + X$ and dimuons produced via the decay of J/ψ particles - has also been investigated. The leading order Feynman diagrams for dimuons produced via the Drell-Yan process and $b\bar{b}$ are shown in figures 5.3(a) and 5.3(d) respectively. These processes have been studied at four-vector level using event samples generated using the PYTHIA event generator. For each of these background samples any event that contains at least two oppositely charged muons with pseudorapidity values in the range, $1.9 < \eta < 4.9$ and having $P_T > 1$GeV/c and $P > 8$GeV/c has been examined as a potential background event. Aside from these criteria, the reconstruction and trigger efficiencies for these samples is conservatively assumed to be 100%. The particle multiplicity for these four-vector events has been estimated by counting the number of stable charged particles with momenta above 500GeV/c that have pseudorapidity values lying within $1.9 < \eta < 4.9$. The sizes of the samples used are summarised in table 5.4 while the particle multiplicity, dimuon acoplanarity, invariant mass and pair transverse momentum distributions for these processes are shown in figure 5.5. Unlike our signal process the dimuon acoplanarity distributions are relatively flat and fall off less dramatically for higher values. The dimuon pair transverse momentum distributions for these processes peak at much higher values (>1.4GeV/c) than our signal and combined have an effective cross-section of ~ 200pb for values below 50MeV/c. The particle multiplicity distributions peak between 10 and 25 and fall off to ~ 4pb for events containing less than three charged particles within the LHCb acceptance while the dimuon invariant mass distributions peak at low mass values and, with the exception of the Drell-Yan distribution which peaks again at the Z pole ($\sim 91 GeV/c^2$), fall off exponentially for higher masses.

5.4.4 Hadron mis-identification

The last important source of background events comes from random combinations of oppositely charged pions or kaons that are both mis-identified as muons. The magnitude of this background contribution has been estimated in the same manner as in chapter 4. Firstly, having assumed that there are two principal ways in which mis-identification can occur, decay in flight and hadron punchthrough, the probability of mis-id as a function of hadron momentum was estimated (for details on how this was achieved see section 4.4.3). These mis-id probabilities were then combined with the expected rate of random π/K combinations from a variety of sources. Most of these sources have been studied using a sample of ten million

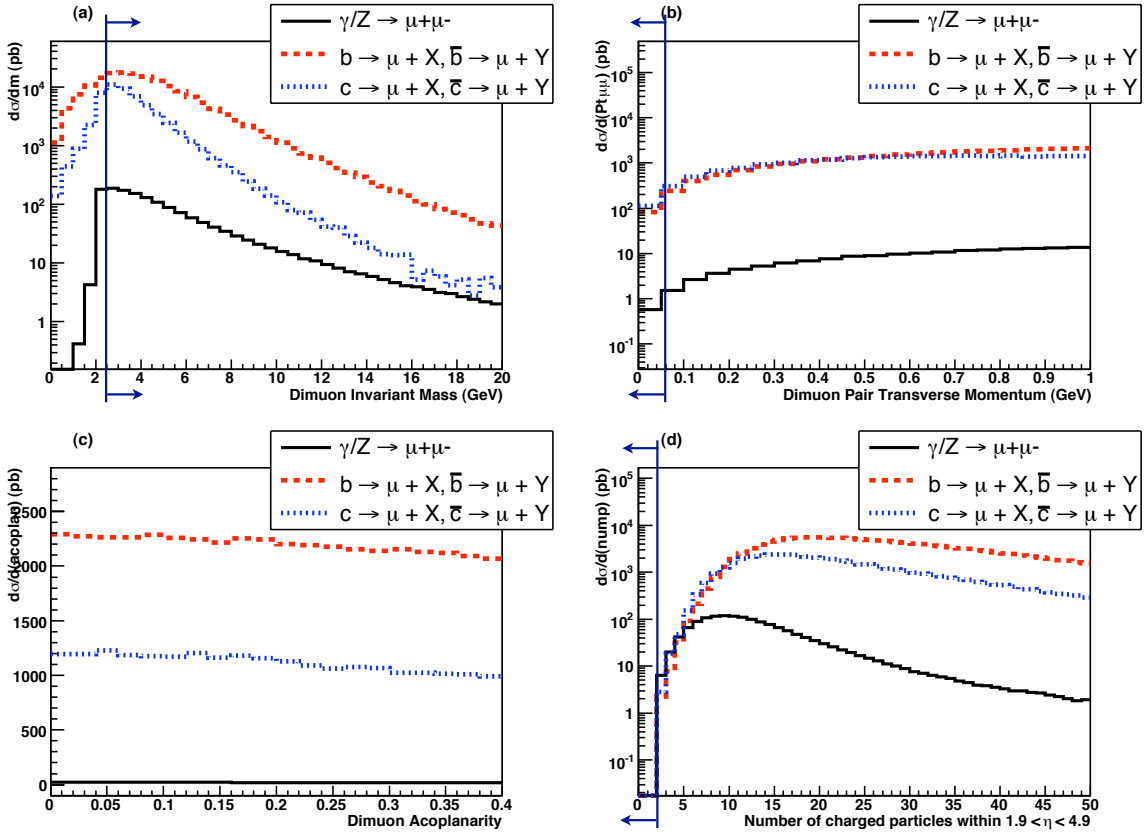

Figure 5.5: Monte-Carlo level events containing a dimuon pair produced via a number of Standard Model processes, here we have assumed a reconstruction and trigger efficiency of 100%. (a) Dimuon invariant mass. (b) Dimuon pair transverse momentum. (c) Dimuon acoplanarity. (d) Event particle multiplicity. The offline kinematic cuts described in section 5 are highlighted.

minimum bias[5] events generated using PYTHIA. In addition an attempt was made to quantify the level of contamination due to di-hadron production via double pomeron exchange since the characteristics of these events may be similar to those of our signal process. This was done by examining two event samples generated with the DPEMC generator. One sample containing two million events where a di-jet is produced inclusively via double pomeron exchange and one containing one million events where two gluons are produced exclusively via double pomeron exchange. Using these two DPE samples and the minimum-bias sample and only considering pions and kaons with pseudorapidity values in the range $1.9 < \eta < 4.9$ and momenta satisfying $P > 8GeV/c$ and $P_T > 1GeV/c$, all the oppositely charged pairwise hadron combinations (i.e. $\pi^+\pi^-$, $K^+\pi^-$, $K^-\pi^+$ and K^+K^-) in these events were recorded. The probability of mis-identification for each hadron was calculated and an overall weighting assigned to each dihadron combination based on these probabilities. Aside from these criteria it was assumed that the reconstruction and trigger efficiencies for these samples is 100%. The particle multiplicity for these four-vector events has been estimated by counting the number of

[5]Corresponding to the PYTHIA process (ISUB) flags 11, 12, 13, 28, 53, 68, 86, 87, 88, 89, 91, 92, 93 ,94, 95, 106, 107 and 108.

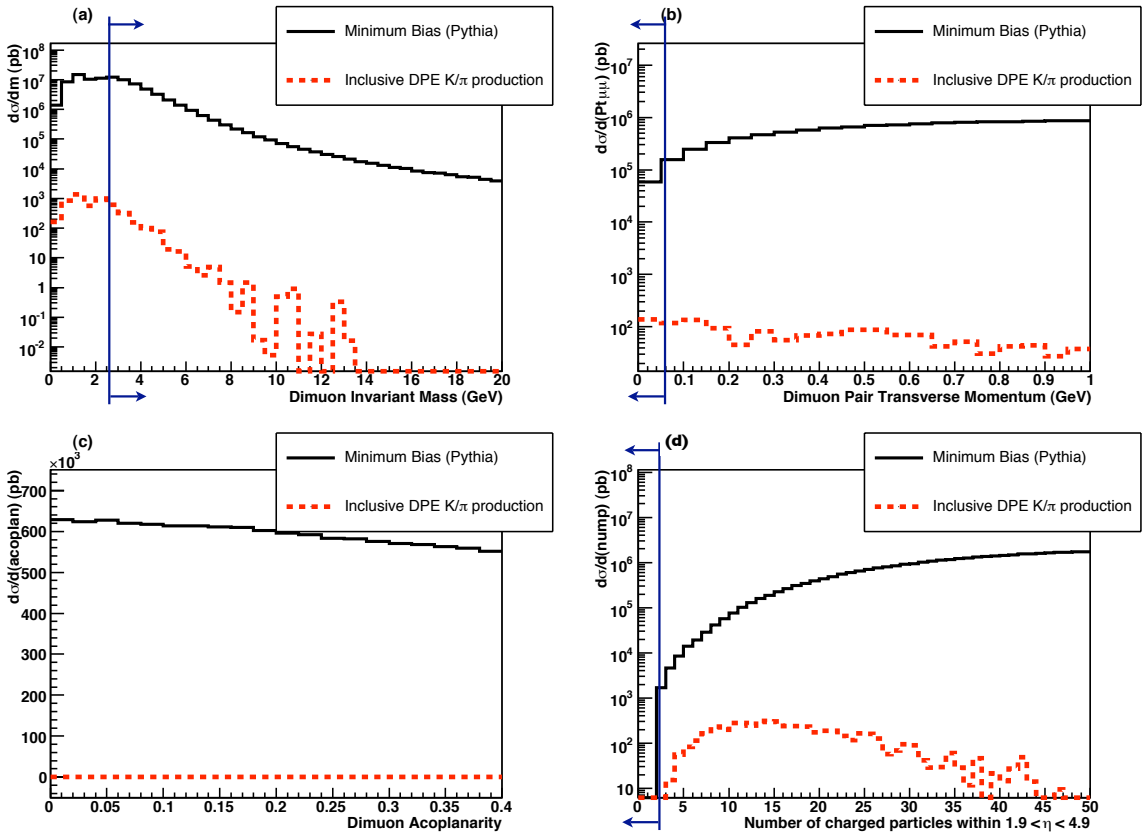

Figure 5.6: Parameter distributions for combinations of oppositely charged kaons and pions coming from minimum-bias and double pomeron exchange events. Here the distributions have been scaled according to the hadron mis-id probabilities discussed in the text and we have assumed a reconstruction and trigger efficiency of 100%. (a) Dimuon invariant mass. (b) Dimuon pair transverse momentum. (c) Dimuon acoplanarity. (d) Event particle multiplicity. The offline kinematic cuts described in section 5.5 are highlighted.

stable charged particles with momenta above 500GeV/c that have pseudorapidity values lying within $1.9 < \eta < 4.9$.The various distributions for these di-hadron combinations are shown in figure 5.6.

5.5 Signal selection and background reduction

Given the particle multiplicity, dimuon invariant mass, pair transverse momentum and acoplanarity distributions of our signal events as shown in figure 5.2, and the corresponding background distributions as shown in figures 5.4, 5.5 and 5.6, the following kinematic cuts are proposed:

1. The dimuon pair transverse momentum must satisfy $P_T^{\mu\mu} < 50 MeV/c$.

2. There must be exactly two reconstructed charged particles in the event.
3. The dimuon invariant mass must be in the range $2.6 GeV/c^2 < M_{\mu\mu} < 20 GeV/c^2$.
4. The mass region $3 - 3.2 GeV/c^2$ is excluded.

Criteria 1, in addition to its effectiveness at reducing the backgrounds described in section 5.4, has the effect of reducing the uncertainty on the predicted signal cross-section, due to rescattering corrections and uncertainties in the electromagnetic form factors of the proton, to $<1\%$. The invariant mass cuts 3 and 4 are designed to further reduce the background contribution coming from the decays $Z \to \mu^+\mu^-$ and $J/\psi \to \mu^+\mu^-$ respectively. The effects of these selection criteria are discussed in the next two sections.

5.5.1 Kinematic Acceptance

The acceptance of these offline kinematic cuts, A_{el}^{kin}, is defined to be the fraction of offline reconstructed $pp \to p + \mu^+\mu^- + p$ events passing all of the trigger stages that also satisfy these kinematic requirements. Using the full detector simulation A_{el}^{kin} was determined to be 0.2697 ± 0.003. Combining this with the geometric acceptance and the reconstruction and trigger efficiencies given in section 3 yields an overall efficiency of 0.0587 ± 0.0008(stat.). This gives an effective signal cross-section of ~ 5.21pb which corresponds to 5210 ± 71(stat.) events in half a nominal year of LHCb running ($1 fb^{-1}$ of data).

5.5.2 Background estimation

The expected background composition after the selection cuts have been applied is summarised in table 5.4. Applying the cuts to the background samples described in section 5.4 reduces the background to a level that is $(4.1 \pm 0.5$(stat.))% of the expected signal rate. This equates to ~ 214 background events per $1 fb^{-1}$. The background is dominated by events caused by pion/kaon mis-identification at a rate of ~ 121 events per $1 fb^{-1}$. In principle it should be possible to accurately assess the level of pion/kaon background from data once they arrive. Events containing dimuon pairs produced by double pomeron exchange or inelastic two photon fusion contribute to the overall background roughly equally (each contributing $\sim 1\%$ of the signal level).

It should be noted that due to the limited size of the Drell-Yan, heavy quark and pion/kaon mis-id samples, the effect of cuts 2-4 and cut 1 have been evaluated separately. The effect of cut 1 on events that have already passed cuts 2-4 was estimated by calculating the probability that an event will satisfy $P_T^{\mu\mu} <$50MeV/c as a function of the events' particle multiplicity. Figure 5.7 shows this probability for the four samples. The dependence of this probability on the event multiplicity was parameterised by fitting straight lines to the four distributions. Using these parameterisations the probability that $P_T^{\mu\mu} <$50MeV/c when the particle multiplicity is less than three was calculated for each background sample. An overall background estimate was made by combining this probability with the calculated probability that the events pass

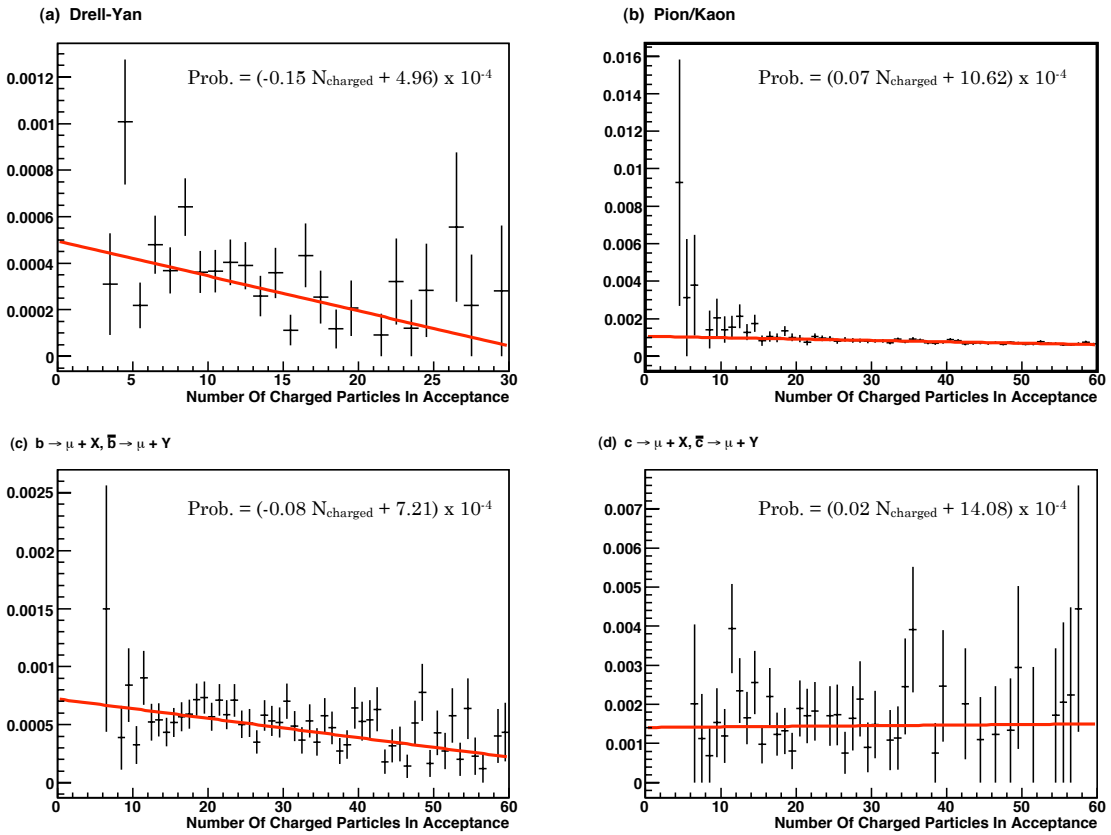

Figure 5.7: Probability of dimuon pair transverse momentum being less than 50MeV/c for events within the invariant mass range defined by cuts 1-2 as a function of the number of charged particles within the LHCb acceptance. (a) $\gamma^*/Z \to \mu^+\mu^-$. (b) Random Pion/Kaon combinations. (c) $b\bar{b}$ events where both b quarks decay semi-leptonically to muons. (d) $c\bar{c}$ events where both c quarks decay semi-leptonically to muons.

cuts 2-4 . The uncertainties on the straight line fits were included in the overall uncertainties of our background estimates.

The mass window proposed in cut 4 is designed to remove the contamination due to the process $J/\psi \to \mu^+\mu^-$. Since the reconstructed width of the J/ψ mass at LHCb via the dimuon channel is $\sim 10 MeV/c^2$[98] we have chosen a window of $\pm 100 MeV/c^2$ and expect a corresponding $J/\psi \to \mu^+\mu^-$ supression of $\sim 10^{-12}$ which equates to much less than 1 event per fb^{-1} of data.

It should be noted that the backgrounds coming from elastic pomeron-photon fusion have not been considered in this study. Here we should be primarily concerned with J/ψ's, $\psi(2s)$'s and Υ's produced via pomeron-photon fusion that subsequently decay into dimuon pairs. The leading order Feynman diagram for this processes, mediated by a J/ψ in this case, is shown in figure 5.3(c). These backgrounds are dangerous since they will exhibit many of the features of our signal process - in particular these events will contain two muons and no other particles. However, since the dimuons will predominantly have invariant masses corresponding to these

Process	Events/fb^{-1}	Statistical	Systematic
$pp \to pp + \mu^+\mu^-$ (signal)	5210	± 71	± 17
Inclusive DPE $\mu^+\mu^-$ production	49	± 15	± 49
$pp \to p + \mu^+\mu^- + X$	31	± 7	± 10
$pp \to Y + \mu^+\mu^- + X$	8	± 5	± 4
$b\bar{b} \to \mu^+ + \mu^- + X$	1	± 0.5	± 1
$c\bar{c} \to \mu^+ + \mu^- + X$	2	± 1	± 2
$J/\psi \to \mu^+\mu^-$	0	$+1$	$+1$
$\gamma^*/Z \to \mu^+\mu^-$	2	± 0.3	± 2
$Pion/Kaon\ mis-id$	121	± 19	± 12 (from data)
Total Background	214	± 26	± 52

Table 5.4: The expected number of events for the signal and background sources per fb^{-1} of data after the selection cuts outlined in section 5.5 have been applied. Statistical uncertainties due to our sample sizes and systematic uncertainties due to the errors on the predicted cross-sections are shown (see section 5.6 for more details).

resonances they can be dealt with by either excluding these mass ranges or estimating their contribution by performing a fit to the invariant mass distribution.

5.6 Pile-up correction

The proposed kinematic selection requires that there are less than three reconstructed charged particles in a given event in order for it to be accepted. This is problematic since at the LHC there will be a non-zero probability that a given bunch crossing will result in more than one proton-proton interaction. Assuming an LHCb running luminosity of $2 \times 10^{32} cm^{-2} s^{-1}$ and an LHC inelastic cross-section of 80mb the probabilities that a bunch crossing will result in zero, one, or more than one interaction are respectively: $P_0 = 0.57$, $P_1 = 0.31$, and $P_{>1} = 0.12$. Since these probabilities are dependent on the inelastic cross-section, which is not known accurately from theory, they must be measured using data. A possible method for making such a measurement at LHCb using the pile-up detector has been investigated previously by N. Zaitsev [99]. As discussed in chapter 3, the pile-up detector is located upstream of the Vertex Locator and consists of a set of two planes of silicon strip detectors equipped with fast readout electronics to allow their data to be made available at the L0 trigger level. During a given running period the number of bunch crossings containing i proton-proton interactions, N_i^m, can be counted. The number counted in this way can then be related to the actual number, N_i, if the efficiency for detection, ε_i, is known. Since we will only select single interaction

dimuon events produced via elastic two photon fusion, N_1^{el}, we will need to relate this number to the total number of signal events from bunch crossings of all types, N^{el}, which is equal to

$$N^{el} = N_1^{el} + N_{>1}^{el} = N_1^{el}(1+f) \tag{5.10}$$

Here $N_{>1}^{el}$ is the number of signal events produced in bunch crossings that contain more than one proton-proton interaction and f is the correction that must be determined from data and will be given by

$$f = \frac{N_{>1}^{el}}{N_1^{el}} \simeq \frac{N_{>1}^{m}\varepsilon_1 - N_1^{m}(1-\varepsilon_1)}{N_1^{m}\varepsilon_{>1} - N_{>1}^{m}(1-\varepsilon_{>1})} \tag{5.11}$$

Since the statistical uncertainties on N_1^m and $N_{>1}^m$ will be $< 0.1\%$ in as little as one second of data, the dominant uncertainty on a measurement of f will be due to the uncertainties on the determination of the efficiencies ε_1 and $\varepsilon_{>1}$. These efficiencies can be determined readily using Monte-Carlo studies, however, a measurement using real data would be preferable and it is envisioned that a viable method for achieving this will be developed before data-taking begins.

5.7 Systematic and statistical uncertainties

From equation 5.1 it can be seen that the accuracy with which an integrated luminosity measurement can be made using the rate of dimuons produced via elastic photon fusion will be limited by the statistical and systematic uncertainties on: the number of $pp \to p + \mu^+\mu^- + p$ candidates observed; the expected number of background events; the geometric and kinematic acceptances; the trigger and reconstruction efficiencies; the predicted cross-section of $pp \to p + \mu^+\mu^- + p$ events at LHCb. The uncertainties from each of these sources will be discussed in turn. The estimated systematic uncertainties from each source are summarised in table 5.5.

5.7.1 Predicted cross-section

As outlined in section 5.2 the uncertainty on the predicted cross-section of our signal process, σ_{el}, will have two components, one from the rescattering corrections due to strong interactions between the colliding protons and the other due to the accuracy of measurements of the proton electromagnetic form factors G_M and G_E.

Rescattering corrections: The events that pass our off-line selection criteria will have dimuon pair transverse momenta of less than 50MeV/c. It has been shown by Khoze et. al. [65] that for dimuon pairs produced via two photon fusion with a mass of 20GeV/c^2, a rapidity of zero and a pair transverse momentum below 50MeV/c, the appropriate uncertainty on σ_{el} is 0.3%. A value of 0.3% has therefore been taken as the systematic uncertainty from this source.

Electromagnetic form factors: Our elastic dimuon event sample will have two components: events where the impact parameters of the colliding protons are large (which allows the protons to be treated as point-like objects) and the process is only sensitive to the proton mass, charge and anomalous magnetic moment (which have been measured with an uncertainty below 0.001%) and events where the protons impact parameters are small and the process is sensitive to the electromagnetic form factors of the proton. As stated in section 5.2, the LPAIR generator[85] has been used to determine the mean Q^2 of our signal events - a value of $< Q^2 >= 0.001 GeV^2$ was found. For such low Q^2 events the appropriate electromagnetic form factor measurements have been made by J. J. Murphy et. al.[86] and can be parameterised by $G_E = 1 - bQ^2$ where $b = (0.110 \pm 0.007) fm^2 = (2.83 \pm 0.18) GeV^{-2}$. The uncertainty on the predicted cross-section due to the electomagnetic form factor measurements will therefore be of the order $4\Delta b < Q^2 >= 0.065\%$. We conservatively assume a systematic uncertainty from this source of 0.1%.

5.7.2 Signal candidates

The uncertainty on the number of $pp \rightarrow p + \mu^+\mu^- + p$ candidates observed, N_{el}^{obs}, will be purely statistical. Using the efficiency and acceptance values obtained from simulation, a 1% uncertainty on N_{el}^{obs} will require 10,000 events which equates to $\simeq 2 fb^{-1}$ of data.

5.7.3 Expected number of background events

The main contributions to the expected number of background events, N_{el}^{back}, will come from events where dimuons are produced via either double pomeron exchange or inelastic two photon fusion and events due to pion/kaon mis-identification. We will discuss each source separately.

Pions/kaons mis-id: It will be possible to measure the background due to pion and kaon mis-identification from data. This can be achieved by measuring the muon mis-identification rate of a pure sample of pions or kaons. For example for pions this can be achieved by examining the pions coming from the decays $K_s \rightarrow \pi^+\pi^-$ and $\Lambda \rightarrow p\pi^-$. Combining these mis-identification probabilities with the measured rate of events containing a di-hadron combination with an invariant mass in the range $2.6 GeV/c^2 < M_{hh} < 20 GeV/c^2$ will enable the background to be evaluated. Assuming the mis-id rates for Pions and Kaons can be determined with an uncertainty of 10% we estimate that the systematic uncertainty on such a measurement will be ± 12 events per fb^{-1} of data.

Double Pomeron Exchange: The expected background contribution due to dimuons produced via double pomeron exchange given in table 5.4 assumes a cross-section for this process of $113 pb$ within the fiducial volume described in section 5.4.2. As previously stated this estimate is the mean of two predictions one using the BPR inclusive DPE model and one using the inclusive model of Cox and Forshaw. As outlined in section 5.4.2 we estimate the uncertainty on this cross-section prediction to be $\pm 113 pb$. Given this uncertainty and the calculated effi-

ciencies for this process we assign a systematic uncertainty on the number of expected dimuon DPE events of ± 49 events per fb^{-1} of data.

Inelastic 2-Photon fusion: The uncertainty on the predicted cross-section for the semi and fully inelastic events has been estimated using LPAIR by calculating the effective cross-section for these events within the LHCb acceptance for two different proton structure functions. One set of structure functions is due to Suri and Yennie[89] while the second combines the Suri-Yennie q^2 dependence for the non-resonant contribution with experimental measurements of the q^2 dependence for the resonance contributions and the photo-production cross-section for $q^2 \to 0$. We have taken the percentage difference between these two predictions to be the systematic uncertainty on the predicted cross-sections. This results in an uncertainty on the cross-section prediction for dimuon production via semi amd fully inelastic 2-photon fusion events at LHCb of 32% and 50% respectively. Given these uncertainties and the calulated efficiencies for these processes we assign a systematic uncertainty on the number of expected semi amd fully inelastic 2-photon fusion events of ± 10 and ± 4 per fb^{-1} of data respectively.

5.7.4 Acceptances

Geometric acceptance: We expect the uncertainty on our geometric acceptance estimate to be dominated by uncertainties due to the tracking resolution near the edges of the LHCb detector. Using the muon tracks from our signal process that have been passed through the LHCb detector simulation the resolution in the reconstructed muon pseudorapidity ($\triangle\eta_\mu$) has been determined near the edges of the LHCb detector. Figures 5.8(a) and 5.8(b) show the variation in $\triangle\eta_\mu$ at the outer edge of the detector and the edge of the detector adjacent the beam pipe. From these plots it can be seen that the detector acceptance range in pseudorapidity is $1.86 < \eta < 4.97$. These variations in $\triangle\eta_\mu$ near the detector edges have been parameterised by straight line fits to the data in the regions $1.8 < \eta < 2.5$ and $4 < \eta < 5$ and yield pseudo-rapidity resolutions of $(2.4 \pm 0.3) \times 10^{-3}$ and $(1.4 \pm 0.6) \times 10^{-3}$ at muon pseudorapidities of 1.86 and 4.97 respectively. The percentage change between the number of events where both muons lie within the ranges $1.8573 < \eta < 4.968$ and $1.8627 < \eta < 4.972$ has been taken as the systematic uncertainty on our calculated geometric acceptance. The calculated value is 0.13%.

Kinematic acceptance: The main uncertainties arising from our estimation of the kinematic acceptance are due to the accuracy of the LHCb detector simulation. The detector simulation will be tuned using data once they are available. In particular the performance of the muon sub-system can be accurately assessed using events containing J/ψ, Υ or Z particles that decay into $\mu^+\mu^-$ pairs. We estimate that once the detector simulation has been re-tuned in this way the kinematic acceptance will contribute a systematic uncertainty on the proposed luminosity measurement of 0.1%. This estimate is in line with similar uncertainty estimates from other experiments[66].

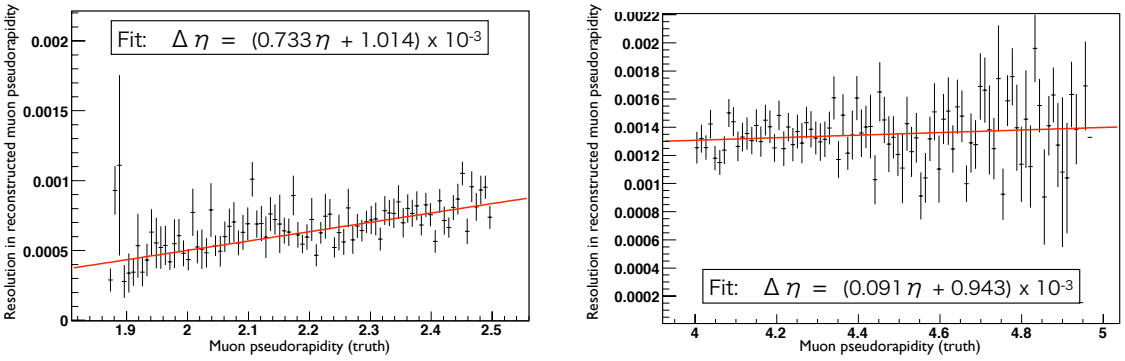

Figure 5.8: Reconstructed pseudorapidity resolution as a function true pseudorapidity for muons reconstructed near the edges of the LHCb detector. (a) low pseudorapidity values corresponding to the outer edge of the detector and (b) high pseudorapidity values corresponding to the detector edge near the beam pipe. The red lines are straight line fits to the data and the fit values are shown.

5.7.5 Reconstruction efficiency

As was pointed out in section 3 the reconstruction efficiency can be determined from data and is expressible as the product of three components,

$$\varepsilon_{el}^{reco} = (\varepsilon_{trk}^{(1)} \times \varepsilon_{match}^{(1)} \times \varepsilon_{id}^{(1)}) \times (\varepsilon_{trk}^{(2)} \times \varepsilon_{match}^{(2)} \times \varepsilon_{id}^{(2)}) \tag{5.12}$$

We will now outline methods that will allow these terms to be measured from data. The uncertainties quoted below are estimates.

Tracking efficiency: ε_{trk} can be determined from data using a pure unbiased sample of $W \rightarrow \mu\nu$ candidate events selected using a tight set of selection criteria based on muon chamber information. The fraction of events in such a sample that have a reconstructed track that points to the appropriate muon chamber deposit will give ε_{trk}. We estimate that a measurement of ε_{trk} will have an associated systematic uncertainty of 0.4%.

Matching efficiency: The efficiency to reconstruct muon towers and match them to reconstructed tracks, ε_{match}, can be found using a data-set containing events with at least one high P_T muon, for example events that pass the single muon trigger line and having $P_T > 10GeV$. The muon in these events is then combined with all the opposite sign high P_T tracks in the event. If a combination has an invariant mass close to the Z mass and the track points to an active area in the muon chambers, the track is considered a candidate. The fraction of these candidate tracks that are actually reconstructed offline as muons will be equal to ε_{match}. We estimate that a measurement of ε_{match} will have an associated systematic uncertainty of 0.4%.

Identification efficiency: The muon ID efficiency, ε_{id}, can be measured using a clean sample of muons that have been selected without using the cuts you wish to examine. Such a sample can be obtained from $J/\psi \rightarrow \mu\mu$ events that have passed the trigger via any stream bar the

dimuon trigger stream (selecting events from the dimuon stream would bias the sample). One of the legs of the J/ψ can then be used to tag the J/ψ, while the other can be used as a probe to measure the muon efficiency. The efficiency will be equal to the number of probe muons that pass the identification cuts divided by the total number of probe muons. Assuming an identification efficiency of 99% and a sample of 10^4 muons, such a measurement of ε_{id} will have an associated systematic uncertainty of 0.1%.

5.7.6 Trigger efficiency

The trigger efficiency, $\varepsilon_{el}^{trigger}$, of our signal process can be determined using a sample of minimum bias events that pass the trigger and contain an off-line reconstructed $\mu\mu$ pair. The trigger efficiency will be equal to the fraction of these events that have passed via the dimuon trigger stream. The uncertainty on such a determination of the trigger efficiency will depend on the size of the sample used. With 10^5 dimuon events and assuming a dimuon trigger efficiency of 44% the uncertainty will be 0.5%.

5.7.7 Resulting measurement uncertainty

The total systematic uncertainty on a measurement of the integrated luminosity using the measured rate of $pp \to p + \mu^+\mu^- + p$ events at LHCb is therefore estimated to be 1.3%. Assuming an average instantaneous luminosity of $2 \times 10^{32} cm^{-2} s^{-1}$ with $1 fb^{-1}$ of data the following integrated luminosity measurement is expected

$$\int \mathcal{L} dt = 1.000 \pm 0.014(stat.) \pm 0.013(syst.) fb^{-1} \tag{5.13}$$

This equates to a total measurement uncertainty of 1.9%. Currently the dominant systematic uncertainty is on the predicted cross-section of events where dimuons are produced via double pomeron exchange. We have estimated this uncertainty to be $\sim \pm 100\%$ of the predicted cross-section for these events. This uncertainty is due to both the theoretical modeling of the process and the measurement uncertainties in the Pomeron flux and Pomeron parton distribution functions (PDFs) that have been determined using $H1$ and ZEUS data from the HERA accelerator at DESY. Recently measurements have been made of the cross-sections for exclusive e^+e^-[100] , $\gamma\gamma$[101] and di-jet[102] production by the CDF collaboration at the Tevatron. These measurements will further constrain the pomeron flux and PDFs and will allow for the refinement of the theoretical models describing the double pomeron exchange production mechanism. We thus expect the uncertainty on the predicted cross-section of dimuons produced via DPE to be reduced in the near future which will allow for more accurate luminosity measurements at LHCb using the $pp \to p + \mu^+\mu^- + p$ process. For example, if the uncertainty on the predicted cross-section for these events was reduced to 25% then the overall systematic uncertainty would be reduced to 1.0%. This would enable a luminosity determination at LHCb to be made with a total uncertainty of 1.4% using $2 fb^{-1}$ of data.

Source	Estimated systematic uncertainty (%)
Rescattering corrections	0.3
Proton EM form factors	0.1
σ_{el} prediction total	0.32
π/K mis-id	0.23
Dimuons produced via DPE	0.94
Dimuons produced via $\gamma\gamma$ fusion	0.27
Background total	1.00
Geometric acceptance	0.13
Kinematic acceptance	0.1
Acceptance total	0.16
Trigger	0.5
Tracking	0.4
Track muon chamber matching	0.4
Muon identification	0.5
Efficiency total	0.76
Total	1.3

Table 5.5: Estimated systematic uncertainties on a luminosity measurement at LHCb using the $pp \to p + \mu^+\mu^- + p$ channel with $1fb^{-1}$ of data.

5.8 Conclusions

It is expected that 5210 $pp \to p + \mu^+\mu^- + p$ events will be recorded and reconstructed at LHCb in $1fb^{-1}$ of data. A set of simple offline selection criteria have been proposed that will reduce the background to a level that is $4.1 \pm 0.5(stat.) \pm 1.0(syst.)\%$ of the signal rate. This background will be dominated by the combinatoric backgrounds due to pion and kaon mis-identification, a background source that can be well understood from real data. It is estimated that using the measured rate of $pp \to p + \mu^+\mu^- + p$ events in $1fb^{-1}(2fb^{-1})$ of data, the integrated luminosity can be measured at LHCb with a $\sim 1.9\%(1.6\%)$ precision. This uncertainty is dominated by the systematic uncertainty on the predicted cross-section of dimuons produced via double pomeron exchange. An examination of the measured rate of exclusive l^+l^-, $\gamma\gamma$ and di-jet events at the Tevatron and the other LHC experiments in the near future will further

reduce this source of uncertainty enabling an even more accurate luminosity measurement to be made at LHCb using this channel.

6 Conclusions

The LHCb detector - one of the four main detectors at the LHC - commenced data taking in September 2008. This thesis has presented Monte-Carlo based studies of two physics measurements that will be made using the LHCb detector.

The first measurement, a determination of the total and differential Z cross-section times leptonic branching fraction, will improve our understanding of the internal structure of the proton, test the theoretical structure describing the Strong force in a new energy regime and, in conjunction with a measurement of the W cross-section, precisely test the theory that describes Electroweak interactions. In chapter 4 it was shown that $Z \rightarrow \mu^+\mu^-$ events will be recorded and reconstructed at LHCb at a rate of $\sim 190 evts/pb^{-1}$. A simple set of offline selection criteria was proposed that will select $\sim$90% of the signal events while reducing the background to (3.0 ± 2.9)% of the signal level with the dominant contribution due to combinatoric backgrounds from pion and kaon mis-identification. It is expected that these backgrounds can be well understood from real data or removed using muon isolation criteria. With $100 pb^{-1}$ of data and ignoring luminosity uncertainties, the Z cross-section can be measured in the forward region with a ~ 1% precision which is mainly attributable to systematic uncertainties coming from a number of sources (tracking, muon id, track matching). Comparisons to measurements made by Atlas and CMS can be made by either examining the overlap region ($1.7 < y < 2.6$) in the distribution $d\sigma/dy$ or extrapolating to a total (4π) cross-section measurement. For a 4π measurement the systematic uncertainty will rise to ~ 2.5% due to the theoretical uncertainties on the proton PDFs. Assuming the luminosity can be determined, LHCb will rapidly be able to make a unique measurement of $\sigma_Z \cdot Br(Z \rightarrow \mu^+\mu^-)$ at high rapidities while providing an important cross-check for the corresponding measurements at the central LHC detectors, CMS and Atlas.

The second measurement, a determination of the event rate of the rare QED process $pp \rightarrow p + \mu^+\mu^- + p$, can be used to make a precise evaluation of the absolute luminosity at LHCb - a quantity that is needed for all cross-section measurements. A feasibility study for using this process to determine the absolute luminosity at LHCb was presented in chapter 5. It is expected that $\sim$10k $pp \rightarrow p + \mu^+\mu^- + p$ events will be recorded and reconstructed in a nominal year of running at LHCb ($2 fb^{-1}$). A set of simple offline selection criteria was proposed that will reduce the background to a level that is $4.1 \pm 0.5(\text{stat.}) \pm 1.0(\text{syst.})$% of the signal rate. This background will be dominated by the combinatoric backgrounds due to pion and kaon mis-identification, a background source that can be well understood from real data. It is estimated that using the measured rate of $pp \rightarrow p + \mu^+\mu^- + p$ events in $1 fb^{-1}(2 fb^{-1})$ of data, the integrated luminosity can be measured at LHCb with a $\sim 1.9\%(1.6\%)$ precision. This uncertainty is dominated by the systematic uncertainty on the predicted cross-section of

dimuons produced via double pomeron exchange. An examination of the measured rate of exclusive l^+l^-, $\gamma\gamma$ and di-jet events at the Tevatron and the other LHC experiments in the near future will further reduce this source of uncertainty enabling an even more accurate luminosity measurement to be made at LHCb using this channel.

Bibliography

[1] The LHCb Collaboration, *The LHCb Detector at the LHC*, JINST **3** S08005 (2008).

[2] L. Evans and P. Bryant (editors), *LHC Machine*, JINST **3** S08001 (2008).

[3] S. Glashow, *Partial symmetries of Weak interactions*, Nucl. Phys. **22** 579 (1961).

[4] S. Weinberg, *A model of leptons*, Phys. Rev. Lett. **19** 1264 (1967).

[5] A. Salam, *Weak and electromagnetic interactions*, in: Elementary Particle Theory, ed: Svartholm, Almqvist and Wiksell,Stockholm 367 (1968).

[6] The ATLAS Collaboration, *The ATLAS Experiment at the CERN Large Hadron Collider*, JINST **3** S08003 (2008).

[7] The CMS Collaboration, *The CMS experiment at the CERN LHC*, JINST **3** S08004 (2008).

[8] The ALICE Collaboration, *The ALICE experiment at the CERN LHC*, JINST **3** S08002 (2008).

[9] D. Griffiths, *Introduction to elementary particles*; ISBN 0-471-60386-4 (1987).

[10] I. Aitchison and A. Hey, *Gauge theories in particle physics*; ISBN 0-85274-329-7 (2002).

[11] A. Pich, *The standard model of electroweak interactions*; arXiv:hep-ph/0502010v1 (2007).

[12] C. Amsler et al., *Review of Particle Physics*, Physics Letters **B667**, 1 (2008).

[13] ALEPH, DELPHI, L3 and OPAL collaborations, *The LEP Working Group for Higgs Boson Searches*, Phys. Lett. **B565** 61 (2003).

[14] F.J. Yndurain, *Limits on the mass of the gluon*, Phys. Lett. **B345** 524 (1995).

[15] S. Helgason, *Differential geometry, Lie groups, and symmetric spaces*, Academic Press, New York (1978).

[16] P. Renton, *Electroweak Interactions*, Cambridge University Press (1990).

[17] G. Arnison et al. *Experimental Observation of Lepton Pairs of Invariant Mass Around 95 ,GeV/c2 at the CERN SPS Collider*, Phys. Lett. **126B** 398 (1983).

[18] G. Banner et al. *Evidence for* $Z^0 \rightarrow e^+e^-$ *at the CERN pp Collider*, Phys. Lett. **129B** 130 (1983).

[19] P.W. Higgs, *Broken Symmetries and the Masses of Gauge Bosons*, Phys. Rev. Lett. **13** 508-09 (1964).

[20] J. Goldstone, Nuov. Cim. **19** 154 (1961).

[21] J. M. Campbell et. al. *Hard interactions of quarks and gluons: a primer for LHC physics*, Rep. Prog. Phys. **70** 89D193 (2007).

[22] J. C. Collins and D. E. Soper, *The Theorems of Perturbative QCD*, Ann. Rev. Nucl. Part. Sci. **37** 33 (1987).

[23] G. Altarelli, et. al. *Transverse momentum in Drell-Yan processes*, Phys. Lett., **B76** 351 (1978).

[24] S. D. Drell and T. M. Yan, Ann. Phys. **66** 578 (1971).

[25] G. Alterelli and G. Parisi, *Nucl. Phys.* **B126**, 298 (1977).

[26] R. S. Thorne et. al., *Parton Distributions for the LHC*, Proceedings DIS2007 (2007).

[27] H. L. Lai et. al., Eur. Phys. J. **C12** 375 (2001).

[28] K. Melnikov and F. Petriello, *Electroweak gauge boson production at hadron colliders through* $O(\alpha_s^2)$, Phys. Rev. **D74**, 114017 (2006).

[29] T. Sjostrand et. al. *Pythia 6.4 physics and manual*, JHEP, **05** 026 (2006).

[30] G. Marchesini et al. *Herwig: A monte carlo event generator for simulating hadron emis- sion reactions with interfering gluons - version 5.1*, Comput. Phys. Commun., **67** 465D508 (1992).

[31] T. D. Gottschalk. *An improved description of hadronization in the qcd cluster model for e+ e- annihilation*, Nucl. Phys., **B239** 349 (1984).

[32] E. D. Courant, M. S. Livingstone and H. S. Snyder, Phys. Rev. 88, 1190 (1952).

[33] LHCb public website, [http://lhcb.web.cern.ch/lhcb/].

[34] The LHCb collaboration, *LHCb Technical Design Report 5, LHCb Vertex Locator*, CERN-LHCC-2001-011 (2001).

[35] The LHCb collaboration, *LHCb Technical Design Report 1, LHCb Magnet*, CERN-LHCC-2000-007 (2000).

[36] The LHCb collaboration, *LHCb Technical Design Report 9, LHCb Reoptimized Detector*, CERN-LHCC-2003-030 (2003).

[37] LHCb Silicon Tracker public website, [http://lhcb.physik.uzh.ch/ST/]

[38] The LHCb collaboration, *LHCb Technical Design Report 8, LHCb Inner Tracker*, CERN-LHCC-2002-029 (2002).

[39] The LHCb collaboration, *LHCb Technical Design Report 6, LHCb Outer Tracker*, CERN-LHCC-2001-024 (2001).

[40] O. Callot and S. Hansmann-Menzemer, *The Forward Tracking: Algorithm and Performance Studies*, LHCb note, LHCb-015-2007 (2007).

[41] R. Forty, *Track seeding*, LHCb note, LHCb-109-2001 (2001).

[42] R.E. Kalman, *A new approach to linear ltering and prediction problems*, Trans. ASME J. Bas. Eng. **D82** 35 (1960).

[43] J. Van Tilburg, *Track simulation and reconstruction in LHCb*, PhD thesis, Vrije Universiteit (2005).

[44] The LHCb collaboration, *LHCb Technical Design Report 3, LHCb RICH*, CERN-LHCC-2000-037 (2000).

[45] The LHCb collaboration, *LHCb Technical Design Report 2, LHCb Calorimeters*, CERN-LHCC-2000-036 (2000).

[46] The LHCb collaboration, *LHCb Technical Design Report 4, LHCb Muon System*, CERN-LHCC-2001-010 (2001).

[47] E. Polycarpo and M. Gandelman, *The Performance of the LHCb Muon Identication Procedure*, LHCb note LHCb-2007-145 (2007).

[48] The LHCb collaboration, *LHCb Technical Design Report 10*, LHCb Trigger System, CERN-LHCC-2003-031 (2003).

[49] The LHCb collaboration, *LHCb Technical Design Report 7, LHCb Online System*, CERN-LHCC-2001-040 (2001).

[50] The LHCb collaboration, *Addendum to the LHCb Online Ststem Technical Design Report*, CERN-LHCC-2005-039 (2005).

[51] The LHCb collaboration, *LHCb Technical Design Report 11, LHCb Computing*, CERN-LHCC-2005-019 (2005).

[52] I. Belyaev et al., *Simulation application for the LHCb experiment*, physics/0306035 (2003).

[53] M. Cattaneo, *The Boole project*, http://lhcb-release-area.web.cern.ch/LHCb-release-area/DOC/boole/ (2008).

[54] M. Cattaneo, *The Brunel project*, http://lhcb-release-area.web.cern.ch/LHCb-release-area/DOC/brunel/ (2008).

[55] P. Koppenburg, *The DaVinci project*, http://lhcb-release-area.web.cern.ch/LHCb-release-area/DOC/davinci/ (2008).

[56] D. J. Lange, *The EvtGen particle decay simulation package*, Nucl. Inst. Meth., **A462** 152-155 (2001).

[57] J. Allison et. al., *Geant4 developments and applications*, IEEE Trans. Nucl. Sci., **53** 270 (2006).

[58] M. Ferro-Luzzi, *Proposal for an absolute luminosity determination in colliding beam experiments using vertex detection of beam-gas interations*, CERN-PH-EP/2005-023 (2005).

[59] A. G. Shamov and V. I. Telnov, *Precision luminosity measurement at LHC using two-photon production of $\mu^+\mu^-$ pairs*, Nucl. Instr. Meth. **A494** 51 (2002).

[60] J. Anderson and R. McNulty, *Luminosity measurements at LHCb using dimuon pairs produced via elastic two photon fusion*, LHCb-2008-001 (2008).

[61] D. Domenici, *Detection of muons in the LHCb experiment: the aging of RPC detectors and the study of $Z \rightarrow \mu^+\mu^-$*, CERN-THESIS-2007-028 (2003).

[62] S. De Capua, *Large mass dimuon detection in the LHCb experiment*, CERN-THESIS-2006-035 (2006).

[63] M. Poli-Lener, *Triple-GEM detectors for the innermost region of the muon apparatus at the LHCb experiment*, CERN-THESIS-2006-013 (2006).

[64] B. R. Webber et. al., *QCD and Collider Physics*, Cambridge University Press (1996).

[65] V. A. Khoze et. al., *Luminosity monitors at the LHC*, IPPP/00/01 (2000). Updated plots from J. Stirling and R. Thorne (private communication).

[66] The CDF collaboration, *Measurements of inclusive W and Z cross-sections in $p\overline{p}$ collisions at $\sqrt{s} = 1.96TeV$*, hep-ex/0508029 (2005).

[67] The D0 collaboration, *Measurement of the Cross-Section for Inclusive Z Production in Di-muon Final States at $\sqrt{s} = 1.96TeV$*, D0 note 4573 (2004).

[68] A. D. Martin et. al., *Parton distributions and the LHC: W and Z production*, hep-ph/9907231 (1999).

[69] R. Thorne, *PDFs at LHCb*, presentation at LHCb-UK meeting, IPPP Durham, http://www.ippp.dur.ac.uk/old/LHCb07/ (September 2007).

[70] J. Campbell and K. Ellis, MCFM webpage http://mcfm.fnal.gov.

[71] A. D. Martin et. al., *MRST2001: partons and α_S from precise deep inelastic scattering and Tevatron jet data*, Eur.Phys.J. **C23** 73-87 (2002).

[72] J. Anderson, *Efficiency Improvements to the Dimuon trigger for high pt events*, presentation at T-Rec meeting, http://indico.cern.ch/conferenceDisplay.py?confId=2934 (August 2006).

[73] The RD5 collaboration, *Measurement of hadron shower punchthrough in iron*, Z. Phys. **C60** 1-10 (1993).

[74] RD5 collaboration, *Measurement of momentum and angular distribution of punchthrough muons at the RD5 experiment*, CERN/PPE/95-195 (1995).

[75] T. Nakada and O. Schneider, *The LHCb Trigger*, In Proceedings of the 4th International Workshop on B Physics and CP Violation (2001).

[76] A. D. Martin et. al., *NNLO global parton analysis*, Phys.Lett. **B531** 216-224 (2002).

[77] C. Anastasiou et. al., *High-precision QCD at hadron colliders: electroweak gauge boson rapidity distributions at NNLO*, Phys.Rev. **D69** 094008 (2004).

[78] A. D. Martin et. al., *Uncertainties of predictions from parton distributions. I: experimental errors*, Eur.Phys.J. **C28** 455-473 (2003).

[79] J. Pumplin et. al., *New Generation of Parton Distributions with Uncertainties from Global QCD Analysis*, JHEP 0207 012 (2002).

[80] Atlas collaboration, *Atlas forward detectors for luminosity measurement and monitoring*, CERN/LHCC/2004-010 (2004).

[81] S. Van Der Meer, *Calibration of the effective beam height at the ISR*, ISR-PO/68-31 (1968).

[82] J. Bosser et al., *LHC beam instrumentation conceptual design report*, LHC Project Report 370 (2000).

[83] J. Anderson and R. McNulty, *Measuring $\sigma_Z \cdot Br(Z \to \mu^+\mu^-)$ at LHCb*, LHCb note, LHCb-2007-114 (2007).

[84] V. M. Budnev et. al., *The process $pp \to ppe^+e^-$ and the possibility of its calculation by means of quantum electrodynamics only*, Nucl. Phys. **B63** (1973).

[85] J. Vermaseren, Nucl. Phys. **B229**, 347 (1983).

[86] J.J.Murphy et. al. Phys.Rev. **C9** 2125 (1974)

[87] Private communication with V. A. Khoze, A. D. Martin and M. Ryskin.

[88] Private communication with K. Hennessy - LHCb note in preparation: K. Hennessy, G. Corti and R. McNulty, *Evaluation of backgrounds from the beam halo*.

[89] A. Suri and D. R. Yennie, Annals Phys. **72** (1972).

[90] M. Boonekamp and T. Kucs, *DPEMC: A Monte-Carlo for double diffraction*, hep-ph/031227 (2004).

[91] A.Bialas and R.Janik, Z.Phys. **C62** 487 (1994).

[92] M. Boonekamp, R. Peschanski, C. Royon, Phys. Rev. Lett. **87** 251806 (2001).

[93] B. Cox and J. Forshaw, Comput. Phys. Commun. **144** 104 (2002).

[94] The H1 collaboration, *Inclusive Measurement of Diffractive Deep-inelastic ep Scattering*, Z. Phys. **C 76** 613-629 (1997).

[95] C. Royon et. al. *Pomeron structure functions from HERA to Tevatron and LHC*, hep-ph/0602228v2 (2006).

[96] C. Royon et. al. *A global analysis of inclusive diffractive cross sections at HERA*, hep-ph/0609291v2 (2006).

[97] A. Bialas, P. V. Landshoff, Phys. Lett. **B256** (1991).

[98] J. M. Amoraal, *The J/ψ selection*, LHCb-2007-052 (2007).

[99] N. Zaitsev, *The Luminosity measurement at the LHCb*, LHCb note, LHCb-1998-053 (1998).

[100] The CDF collaboration, *Observation of Exclusive Electron-Positron Production in Hadron-Hadron Collisions*, Phys. Rev. Lett. **98** 112001 (2007).

[101] The CDF collaboration, *Search for Exclusive Gamma Gamma Production in Hadron-Hadron Collisions*, arXiv:0707.2374 (2007).

[102] CDF collaboration, *Observation of Exclusive Dijet Production at the Fermilab Tevatron p-pbar Collider*, arXiv:0712.0604 (2007).